How to Build a Brain: Insights from Neural Circuit Development and Molecular Engineering

Michael Alex Wheeler
Swainton, NJ

Bachelor of Arts, Neuroscience (Honors)
Minor: Philosophy
Concentration: Biomedical Engineering
Johns Hopkins University, 2010

A Dissertation presented to the Graduate Faculty
of the University of Virginia in Candidacy for the Degree of
Doctor of Philosophy

Department of Biology
Neuroscience Graduate Program

University of Virginia
May, 2016

Preface

I want to thank my friends and family for the support and positivity during graduate school. Additionally, thank you to my graduate thesis committee for advice and guidance (Bimal Desai, Serena Liu, Iggy Provencio, and Michael Scott). Thanks to the Biology Department and Neuroscience Department faculty advice and guidance. Thank you to the Deppmann, Güler, Kucenas, and Condron labs for close advice and guidance. Thank you to the special mentorship and friendship of Tony Spano during graduate school. Finally, thank you to Chris Deppmann and Ali Güler, who are better mentors than I could have ever envisioned, who have challenged me continuously, and are the models against which I will judge myself as a scientist and an advisor.

The work contained here has been published in two papers:

Wheeler, Michael A., et al. "TNF-α/TNFR1 signaling is required for the development and function of primary nociceptors." *Neuron* **82**(3) (2014): 587-602.

Wheeler, Michael A., et al. "Genetically targeted magnetic control of the nervous system." *Nature Neuroscience* (2016).

The structure of this dissertation is: (Chapter 1) a brief introduction to neurotrophic regulation of peripheral circuits; (Chapter 2) Wheeler et al., Neuron 2014; (Chapter 3) a brief history of the development of actuator systems; (Chapter 4) Wheeler et al., Nature Neuroscience 2016; (Chapter 5) Global perspective of the significance of the work contained herein.

Table of Contents

Chapter 1 – Molecular players implicated in sculpting the developing nervous system

I. A perspective on the development and refinement of the peripheral nervous system

Proper organismal function requires precise development and organization of neural circuits. Antagonistic molecular signaling pathways that control the construction and destruction of portions of these circuits are responsible for nervous system assembly[1]. Even after the nervous system is formed, these antagonistic signals continue to work toward refinement of specialized properties of mature neural circuits to correctly tune information transduction. This general principle holds true in the development of one branch of the nervous system, the somatosensory division, which is the sensory system responsible for all forms of tactile sensation (e.g. pain, itch, light touch, proprioception)[2,3]. Herein, antagonistic signaling pathways are explored in the context of how they sculpt the peripheral nervous system and control input gain for touch perception.

The somatosensory system is a network of peripheral sensory neurons distributed across the entire body with the ability to interpret the different tactile, thermal, mechanical, and chemical forces that contact bodily tissue (Cajal S.R., 1899). Peripheral sensory neurons innervate distinct end organs such as hair follicles, Meissner corpuscles, Merkel complexes, Pacinian corpuscles, Ruffini corpuscles, or simply terminate in the epidermis as free nerve endings; each ending transduces a specific sensory percept to the central nervous system[4–7]. The diversity of somatosensory impulses that can be sensed by the body is "somatotopically" mapped onto higher order targets in the nervous system, thus permitting fine discrimination between these sensations[5].

Proper construction of any neural system requires growth, synaptogenesis, and survival, which, in the case of the somatosensory system, increase receptivity to touch

sensation. Destructive forces dampen innervation, connectivity, and survival of neurons, which can potentially cause a decrease in tactile signal gain[8,9]. Achieving a balance between the establishment of functional components and the elimination of excessive elements is realized through two receptor families that work against one another[10–14].

Construction of the sensory nervous system depends in part on the ability of a single family of receptors to bind their ligands. The Trk family of receptor tyrosine kinases (RTKs) binds to a subset of target derived growth factors called the neurotrophins, which generate signals that promote neural differentiation, survival, axon growth, and proper integration with central circuits[15]. There are three Trk receptors: TrkA, TrkB, and TrkC, which bind with high affinity to the neurotrophins nerve growth factor (NGF), brain derived neurotrophic factor (BDNF), and neurotrophin-3 (NT-3), respectively. Peripheral sensory neurons each express one type of Trk receptor, which influences whether the sensory neuron will transduce nociceptive, mechanosensory, or proprioceptive information[16,17]. Although the role of Trk receptors in the construction of the somatosensory system is well studied, the mechanisms that refine neurotrophin-mediated assembly, or in other words, coordinate disassembly, remain poorly understood.

One potential mechanism is that a family of opposing receptors generates destructive signals as a means of tuning Trk-dependent pathways. Consistent with this idea, sensory neurons also express members of the tumor necrosis factor receptor (TNFR) superfamily, which are known to promote apoptosis, axon degeneration, and synapse restriction[18–20]. Whereas Trk receptor signaling generally promotes growth, differentiation, and survival, TNFR “death receptor” signaling tends to actively oppose these pathways. TNFRs are highly expressed in tissues rich in neurotrophin-dependent neurons such as

somatosensory, sympathetic, and basal forebrain neurons. Thus, one could postulate that wherever Trk receptors are promoting construction, TNFRs are antithetically promoting destruction.

This prediction remains to be more fully elucidated. Although Trk survival signaling is very well characterized and TNFR death signaling is also well studied, the interface of this developmental antagonism is not widely understood. Thus, the question I am currently investigating is: How does proper tactile sense arise as a function of destructive TNFR signals working against constructive neurotrophin signals?

II. Molecular mechanisms regulating refinement of the PNS

The aforementioned work supports the notion that the Trks are "neuroconstructive" mediators, meaning that they assist the developing nervous system in cell survival, target innervation, and establishment of synaptic contacts. However, the eminently prophetic, and accurate, "Neurotrophic Factor Hypothesis" posits that neurons without sufficient amounts of growth factor signaling will die[21]. In accordance with this prediction, it is now known that approximately half of the neurons generated in the massive waves of developmental neurogenesis die by adulthood[13,22]. In other words, evidence suggests that there are "neurodestructive" forces working against constructive Trk signals. Is this death mediated solely by growth factor deprivation or could other factors be at play? In fact, couldn't there just as easily be coordination of destructive signaling meant to directly antagonize constructive Trk pathways?

One answer to these questions comes from elegant studies investigating BDNF function during development. Although BDNF promotes the growth and survival of TrkB-

expressing neurons through canonical Trk signaling, it is also a crucial factor involved in signaling apoptosis during peripheral neuron development independent of TrkB[22,23]. How is it that one molecule is able to induce two antithetical signaling cascades within a single neuron? What particular characteristics of the Trk receptors enable them to promote constructive signals when other receptors are primed to destroy neurons even when binding the same molecule? The well-established systems of postganglionic sympathetic and primary sensory neurons are the framework for analyzing the nature of these very questions.

III. Mechanisms of Developmental Death

Numerous molecules have been shown to oppose different aspects of Trk signaling both from within and without the cell, such as BDNF action mentioned earlier[22,24]. Thus, there seem to be molecules capable of transducing intracellular signals to oppose the constructive signals generated by Trk receptors. If this is in fact the case, which signals are sufficient to counteract Trk activity? Moreover, how does a cell discriminate between almost omnipresent external and internal cues that could be utilized to suppress Trk signals? Despite the apparent complexity in potential signal transduction mechanisms, general differences in antagonism of Trk receptors can be parsed out, permitting a broad categorization of state-dependent constructive/destructive signal antagonism in prototypical neurotrophin systems.

For instance, it is no secret that a dearth of growth factor signaling induces a death program in neurons[25]. However, the mechanisms by which this death occurs are more obscure than the homogeneous phenotype of pyknotic, dying neurons. Since it is known

that growth factor signals emanating from the Trk receptors induce survival signals, it is possible that a lack of neurotrophin fails to activate survival pathways leading to a death program in the cells simply through survival pathway *inactivity*. Alternatively, the possibility exists that trophic signals instead suppress a "default" death signal within cells but that under certain conditions the death signal can overcome survival pathways to induce apoptosis. The current evidence indicates that these two possibilities are not mutually exclusive and an accurate picture of developmental cell death probably requires a blend of the two.

IV. The Many Functions of p75NTR

Given that absence of neurotrophin leads to a time-dependent death pathway for developing, neurotrophin-supported neurons via Trk inactivity and probably an intrinsic death program[13], what are the mechanisms in place for promoting death? Is neuronal destruction caused by the Trk receptors' mirror image, the purpose of which is to destroy neurons? Although not quite the mirror image of Trk receptors in terms of function, numerous groups have reported that the low affinity neurotrophin receptor p75NTR (henceforth referred to as p75NTR or p75), is in fact one cause of this ongoing death signal in developing cells[11–13,22].

(a) p75 Can Work Against TrkA

In the late 1970s, it was discerned from studies of binding kinetics that NGF can bind multiple distinct receptors on cells[26]. In fact, further studies more fully uncovered the affinities to which NGF binds its receptors as well as an identification of the receptors

themselves[27,28]. p75 alone binds all of the neurotrophins with low affinity, and can also bind ligands such as myelin associated glycoprotein (MAG) or oligodendrocyte myelin glycoprotein (OMgp) in a complex with the co-receptor NgR1 to degenerate axons[29,30]. In addition, p75 binds pro-forms of all of the neurotrophic factors, which, as some groups have reported, causes cell death[31–33].

After the period of developmental neurogenesis when mature neurons are extending their axons toward their targets, p75 is critical for underlying cell death mechanisms. It has been shown by multiple groups that neurons with high NGF-TrkA signaling upregulate BDNF and secrete it in a paracrine manner to serve as an apoptotic cue[13,22]. The secreted BDNF binds to p75 receptors on neighboring neurons, which transduces an apoptotic signal in neurons without trophic activity sufficient enough to overcome the death signal. This particular paradigm has also been shown to restrict axon growth and promote pruning of neural fibers[11].

(b) p75 Can Work With TrkA?

p75 is an interesting receptor in that differing growth factor concentrations seem to induce state-dependent signaling responses such as death at low concentrations and survival at high concentrations[34]. In fact, some groups suggest that even though it can cause death, p75 can actually enhance Trk-mediated survival under conditions of high neurotrophin concentration[35,36]. Some of these controversial studies have argued that p75 augments TrkA's ability to transduce signals but this evidence is still not widely accepted. An elaborate study of NGF binding kinetics to TrkA and p75 was undertaken by Barbara Hempstead in Moses Chao's lab in 1991. They found that radiolabelled NGF bound with

high affinity only in the presence of both p75 and TrkA receptors. This led them to the conclusion that the receptors potentially interact with one another[24].

In support of the Hempstead findings, there are several lines of evidence that suggest TrkA functions less optimally in p75(-/-) mice. Lee, Davies, and Jaenisch argued that p75(-/-) DRG and SCG neurons are less sensitive to NGF but more sensitive to NT-3 (Lee et al. 1994). An additional study by Bergmann and others in 1997 analyzed the epidermal innervation pattern of nociceptors in p75(-/-) mice[37]. They found a decreased density of nociceptors in the skin as well as insensitivity to pain in p75(-/-) mice, which are essentially NGF-TrkA signaling readouts. Indeed, work from our own lab confirms Bergmann's findings as p75(-/-) mice are hyposensitive to pain, have a hypoinnervated epidermis, and express hypoexcitable nociceptive sensory neurons (Wheeler et al., unpublished data).

These data still remain controversial. Work from Freda Miller's lab has demonstrated opposing findings that p75(-/-) sympathetic neurons grow more robustly in response to lower concentrations of NGF. Furthermore, other work from our lab shows that p75(-/-) neurons can survive under conditions of lower NGF than WT sympathetic neurons (Edamura et al., unpublished data). Whether these findings suggest that p75 directly assists Trk receptors, directly opposes Trk receptors, latently inhibits other Trk-inhibitors, or acts in a state-dependent manner to perform all of the above roles still remains unclear.

(c) Dependence Receptors: p75/TrkA

Until recently, the TrkA-p75 interaction dogma was that the two receptors could form a complex together to bind NGF and transduce signals. However, members of Chris Garcia's lab performed a beautiful structural analysis of p75 and TrkA to test the heterodimerization theory. They found that there is no structural evidence to support a direct p75/TrkA interaction[38]. This means that if these two receptors are coordinating growth then they are doing so with common adaptor proteins or at shared nodes of signal transduction.

One potential shared signaling node between Trk receptors and p75 is the recent and controversial finding that p75-mediated death is aided by the supposed "pro-survival" TrkA and TrkC receptors[39]. Work by Alain-Barde's laboratory involved the generation of ES cell lines expressing GFP, TrkA, TrkB, and TrkC driven from the *Mapt* locus, which is neuron-specific. They found that selective elimination of TrkA or TrkC increased cell survival both *in vivo* and *in vitro* under conditions of growth factor deprivation. In addition, overexpression of TrkA or TrkC, but not TrkB, enhanced cell death of ES cells.

The Nikoletopoulou work taken together with studies of p75-TrkA cooperation, highlights an important concept in developmental biology: the theory of dependence receptors[40]. This theory mainly hypothesizes that certain receptors can function differently in the presence or absence of ligand. For instance, although TrkA and TrkC play a major role in developmental survival, they are also implicated in cell death that they promote together with the death receptor p75 when growth factor is absent. Alternatively, even though p75NTR can promote death, there is evidence that it also aids in promoting survival under high neurotrophin concentrations. These intriguing properties increase the combinatorial arrangement of the ligand-receptor system, which causes more diverse

cellular states than simply “survival” or “death.” Dependence receptors such as p75, TrkA, or TrkC can thus act as a cellular safeguard whereby death program activation is contingent on a distinct molecular state rather than simply activation of a single receptor by one ligand.

Chapter 2 – TNFα/TNFR1 forward and reverse signaling coordinate the development and function of multiple nociceptor subtypes

I. Introduction

The ability to discriminate between innocuous and painful touch is critical for survival. Nociceptors are polymodal sensory neurons that relay information about noxious tactile cues from peripheral targets to the spinal cord (Julius and Basbaum 2001, Craig 2003, Basbaum et al. 2009). Importantly, nociceptors are defined by their high excitability thresholds for thermal, mechanical, or chemical stimuli; pain is perceived only when these stimuli are potent enough to trigger action potentials (Woolf and Salter 2000, Hunt and Mantyh 2001). Critical properties of nociceptors that govern the perceived intensity of a painful stimulus include density of peripheral target innervation, proper targeting of central projections, and excitability thresholds (Pezet and McMahon 2006). It follows that if any of these components were enhanced or attenuated then the perception of pain would be altered.

A signaling pathway central in tuning nociceptor sensitivity is that of target-derived nerve growth factor (NGF), which regulates survival, axon growth, and excitability of nociceptors (Crowley et al. 1994, Patel et al. 2000, Chuang et al. 2001). Peripheral targets such as the skin release NGF during development, around the time that newly born nociceptors begin to innervate peripheral targets (Marmigère and Ernfors 2007, Lallemend and Ernfors 2012). Secreted NGF binds to a receptor tyrosine kinase (RTK), TrkA, on developing nociceptors to transduce intracellular signals that are required for survival and target innervation (Crowley et al. 1994, Patel et al. 2000). Deletion of genes encoding NGF or TrkA causes the death of all nociceptors during development and, as a result, pain

insensitivity (Verhoeven et al. 2006, Indo et al. 1996). Conversely, hyperactivation of NGF-TrkA signaling can cause hyperalgesia or allodynia, which skew pain thresholds toward hypersensitivity (Neumann et al. 1996, Woolf and Salter 2000, Costigan et al. 2009, Mantyh 2011). Thus, NGF signaling must be tightly tuned during development such that pain is properly interpreted.

Maturation of several functionally distinct nociceptor subclasses also requires NGF-TrkA signaling during embryonic and postnatal nociceptor development (Luo et al. 2007, Gascon et al. 2010, Marmigère and Ernfors 2007). The two major populations of mature nociceptor subclasses are peptidergic and non-peptidergic nociceptors. Peptidergic nociceptors express TrkA, calcitonin gene-related peptide (CGRP), and substance P throughout development and are responsive to target-derived NGF (Lallemend and Ernfors 2012). Non-peptidergic nociceptors do not express TrkA or neuropeptides, but rather express an RTK, Ret, which is responsive to the target-derived glial cell line-derived neurotrophic factor (GDNF) family of ligands (Airaksinen and Saarma 2002, Molliver et al. 1997). Loss of GDNF family receptor α 2 (GFRα2), a Ret co-receptor that responds to the GDNF family ligand, neurturin (NRTN), impairs peripheral target innervation and sensitivity to inflammatory pain (Lindfors et al. 2006). Interestingly, acute pain is sensed by TrkA+ peptidergic nociceptors in the absence of NRTN signaling, suggesting that TrkA+ and Ret+ nociceptors are functionally distinct from one another in adulthood despite being derived from the same early TrkA+ nociceptor lineage during embryonic development (Marmigère and Ernfors 2007, Liu and Ma 2011). Together, these studies suggest that NGF-TrkA signaling is critical for the orchestration of peptidergic and non-peptidergic nociceptive circuits, which underlie the perception of distinct forms of painful touch.

Given the broad phenotypes and functions that NGF-TrkA signaling regulates, it stands to reason that there should be factors that modulate TrkA function and, by extension, tune and refine broad aspects of developing nociceptive circuits. Clues for this hypothesis come from studies in the sympathetic nervous system, which also requires NGF-TrkA signaling for survival and target innervation (Crowley et al. 1994, Glebova and Ginty 2004). Antagonism of NGF-TrkA signals can occur via the p75 neurotrophin receptor (p75NTR), which induces death (Deppmann et al. 2008), promotes axon pruning (Singh et al. 2008), dampens excitability (Luther and Birren 2009), and restricts post-synaptic densities (Sharma et al. 2010) in sympathetic neurons. As such, elimination of *p75NTR* is analogous to TrkA gain-of-function in sympathetic neurons. Consequently, one would expect that the loss of p75NTR in nociceptors would manifest as heightened pain sensitivity. Surprisingly, however, numerous reports argue the opposite; loss of p75NTR results in decreased pain sensitivity and reduced cutaneous innervation by nociceptors (Lee et al. 1992, Bergmann et al. 1997). Nociceptors from *p75NTR*$^{-/-}$ mice are roughly 3-fold less sensitive to NGF (Davies et al. 1993, Lee et al. 1994), which suggests that p75NTR likely augments NGF-TrkA signaling in nociceptors.

If not p75NTR, might a different receptor buffer NGF-TrkA signaling in nociceptors? It is possible that receptors structurally related to p75NTR may function as negative regulators of NGF-TrkA signals in nociceptors. Indeed, p75NTR is just one of 29 tumor necrosis factor (TNF) receptor (TNFR) superfamily members, many of which are implicated in the modulation of growth factor signaling (Deppmann and Janes 2012, Locksley et al. 2001). To test this idea, we screened the expression of 23 TNFR family members in the dorsal root ganglion (DRG), which revealed the selective expression of three highly related family

members: TNFR1, p75NTR, and death receptor 6 (DR6). Herein we pursued the role of TNFα-TNFR1 signaling in nociceptor development in part because it has been shown to negatively regulate events such as growth and survival in the sympathetic nervous system (Barker et al. 2001, Kisiswa et al. 2013). Similar to reported phenotypes in the sympathetic nervous system, we report that TNFα-TNFR1 can also inhibit the development of NGF-TrkA-dependent sensory circuits by negatively regulating axon growth, survival, and excitability of TrkA+ primary nociceptors. Moreover, loss of either TNFα or TNFR1 drives TrkA+ nociceptors toward a premature non-peptidergic fate. Surprisingly, we found that TNFR1 plays a dichotomous role in the function of peptidergic and non-peptidergic nociceptors. While TrkA+ peptidergic nociceptors exhibit increased responsiveness to NGF as evidenced by enhanced growth and excitability in the absence of TNFR1 or TNFα, the Ret+/TrkA- population of non-peptidergic nociceptors exhibits functional impairments in NRTN-dependent axon growth and excitability. We demonstrate that *Tnf* and *Tnfr1* null mice are hypersensitive to several pain modalities due to enhanced nociceptor sensitivity. Finally, we show that the increased gain in nociceptive signals observed in *Tnf* or *Tnfr1* knockouts is caused by an increase in the NGF sensitivity of TrkA+ nociceptors, as a *Tnfr1* deletion rescues pain insensitivity phenotypes observed in *Ngf* $^{+/-}$ mice. These results suggest that TNFα and TNFR1 together coordinate the development and function of molecularly distinct nociceptive circuits through cross-talk with TrkA and Ret to either block or promote pain sensitivity in peptidergic and non-peptidergic nociceptor populations, respectively.

II. Results

(a) Characterization of TNFα and TNFR1 expression on nociceptors and their targets

In order to identify putative factors that can antagonize NGF-TrkA dependent signaling in nociceptors, we examined the expression of 23 TNFR family members in embryonic day (E)18.5 DRG, brain, or muscle via reverse transcriptase polymerase chain reaction (RT-PCR) **(Figure S1A)**. This analysis revealed selective expression of three highly related TNFR family members in the DRG: *p75NTR* (TNFRSF16), *Dr6* (TNFRSF21), and *Tnfr1* (TNFRSF1A). We focused on TNFR1, which is an understudied TNFR family member in the context of nociceptor development and function. Given that TNFR1 is robustly expressed in the DRG, which contains many different cell types, we next sought to determine whether it is expressed on nociceptors. To this end, we performed immunohistochemistry to examine percent colocalization of TNFR1 with CGRP, peripherin, or TrkA at postnatal day (P)0 **(Figure 1A-F)**. CGRP and TrkA represent peptidergic nociceptors while peripherin labels small-diameter unmyelinated nociceptors. In each case, TNFR1 colocalizes with nociceptive markers >99% of the time.

We performed the same analysis at P30 when most nociceptors are terminally specialized into distinct functional subclasses (Lallemend and Ernfors 2012). In addition to CGRP, TrkA, and peripherin, we examined non-peptidergic neurons by staining with the fluorescently conjugated lectin, IB4. We observed similar levels of colocalization at P30 as at P0 (i.e. at least 98.7% of nociceptors are positive for TNFR1) **(Figure 1G-N)**. We found that TNFR1 is localized to both the cell bodies and axons of sensory neurons both *in vivo* **(Figure S1B-C)** and *in vitro* **(Figure S1D)**. Together, these analyses suggest that TNFR1 is found ubiquitously on nociceptors across different stages of sensory circuit development, ranging from early to mature nociceptor populations.

We also sought to localize the sources of TNFα in developing nociceptive circuits, which may lend clues as to how nociceptors interpret TNFα signaling. TNFα is enriched on sensory neurons in the P4 DRG **(Figure S1E)**, in the epidermis between P0 and P30 **(Figure 1O-P; Figure S1F-G),** and in the marginal zone and second order spinal cord neurons at P7 **(Figure 1Q; Figure S1H)**. Taken together these data suggest that sensory neurons, peripheral targets, and central targets express TNFα and signal to nociceptors through TNFR1 throughout critical periods of nociceptor circuit maturation.

(b) TNFα-TNFR1 signaling suppresses skin innervation and NGF-dependent neurite growth programs

In normal development, NGF-TrkA signaling functions to control nociceptor axon growth into peripheral targets (Patel et al. 2000). If TNFα-TNFR1 signaling antagonizes NGF-TrkA dependent growth of nociceptors into peripheral targets, we would predict that axon overgrowth into the skin would be observed in *Tnfr1*$^{-/-}$ and *Tnf* $^{-/-}$ mice. To test whether TNFα-TNFR1 signaling is indeed required, *in vivo,* for proper axon innervation of peripheral targets, we performed immunohistochemical analyses for nociceptive axons in the epidermis, as described previously (Zylka et al. 2005). First, we observed that there is an increased density of small-diameter peripherin+ axons in glabrous skin at P0 in *Tnfr1*$^{-/-}$ and *Tnf* $^{-/-}$ animals relative to wild type (WT) **(Figure 2A; Figure S2A)**. We then stained for the pan-axonal marker protein gene product 9.5 (PGP9.5) and observed twice as many PGP9.5+ nociceptive fibers projecting into the epidermis in *Tnfr1*$^{-/-}$ or *Tnf* $^{-/-}$ mice than WT mice by P30, suggesting that TNFα and TNFR1 normally suppress axon growth programs in the periphery **(Figure 2B-C; Figure S2B-C)**. Finally, whole-mount substance P or peripherin

immunostaining of the forepaw revealed that as early as E14.5, misguided nociceptive axons densely innervate the digits and footpad of the paw in mice lacking TNFα or TNFR1 **(Figure 2D; Figure S2D)**. Taken together these data suggest that the TNFα-TNFR1 pathway is critical in regulating growth and refinement of peripheral axonal projections *in vivo*.

To examine the role of TNFR1 on NGF-TrkA dependent neurite growth *in vitro*, we established dissociated sensory neurons from WT or *Tnfr1*$^{-/-}$ mice in microfluidic devices, which spatially isolate neuronal cell bodies and neurites (Park et al. 2006). We found that WT neurons bathed in NGF along with TNFα or brain-derived neurotrophic factor (BDNF) showed significantly lower rates of neurite growth than WT neurons bathed in NGF alone **(Figure 2E)**. Strikingly, *Tnfr1*$^{-/-}$ axons grew roughly 5 times faster than WT neurons in response to 10 ng/mL NGF, suggesting that TNFR1 plays a role in suppressing NGF-dependent neurite growth **(Figure 2E)**. While TNFα had no effect on NGF dependent neurite growth in *Tnfr1*$^{-/-}$ neurons, we observed that BDNF still slowed neurite growth in *Tnfr1*$^{-/-}$ neurons bathed in NGF, albeit to a lesser degree than BDNF treatment on WT mice neurons **(Figure 2E; Figure S2E)**. To assess the effect of NGF mediated neurite growth on whole ganglia from *Tnfr1*$^{-/-}$ and *Tnf* $^{-/-}$ mice, E14.5 DRG explants were also cultured in NGF, which yielded similar results as the dissociated cultures; *Tnfr1*$^{-/-}$ and *Tnf* $^{-/-}$ neurites grew ~2-4 times more rapidly than WT neurites **(Figure 2F-G; Figure S2F-G).** Together, these data suggest that neurons lacking *Tnfr1* or *Tnf* are more responsive to NGF in the context of *in vitro* neurite growth assays.

(c) TNFα-TNFR1 signaling is required for proper axon guidance of peptidergic central projections

In *Tnfr1*$^{-/-}$ and *Tnf* $^{-/-}$ mice, nociceptor peripheral projections display phenotypes reminiscent of those observed in classical NGF-TrkA gain-of-function experiments with axon overgrowth into peripheral targets (Aloe et al. 1975). Therefore, we sought to test whether nociceptor central projections were disrupted similar to peripheral projections in *Tnfr1*$^{-/-}$ and *Tnf* $^{-/-}$ mice. To address this, we compared peptidergic (TrkA+, CGRP+) central projections in the spinal cord between WT, *Tnfr1*$^{-/-}$, and *Tnf* $^{-/-}$ mice at P0, P7, and P30. We found that mice lacking TNFR1 or TNFα display a 50% larger area occupied by TrkA+ and CGRP+ peptidergic fibers than WT lumbar dorsal horn at P0 **(Figure 3A-E; Figure S3A-E)**. Moreover, most sections contained axon bundles that misprojected within the dorsal horn and extended medially and/or laterally **(Figure 3F, Figure S3F)**. The same analyses performed at P7 and P30 revealed similar phenotypes suggesting that central projection defects are stable even after terminal differentiation **(Figure 3G-R; Figure S3G-R)**. The enhanced growth and misguidance of *Tnfr1*$^{-/-}$ and *Tnf* $^{-/-}$ central projections are reminiscent of other pathways that negatively modulate NGF-dependent central projections such as HoxD1 (Guo et al. 2011), suggesting that TNFα-TNFR1 signaling is also required for proper growth and promotion of central projection refinement.

(d) TNFα-TNFR1 signaling coordinates nociceptor differentiation

There are several possible explanations for the increase in peptidergic peripheral and central projection densities that occur in *Tnfr1*$^{-/-}$ and *Tnf* $^{-/-}$ mice: 1) an increase in the neurite density of individual nociceptors and/or 2) more nociceptors in the DRG, which would increase the overall number of axons projecting to the skin and spinal cord. Although we have established that loss of TNFR1 signaling enhances NGF dependent axon growth, it is

also possible that TNFR1 antagonizes non-axon growth aspects of NGF-TrkA signaling such as cell death and differentiation in the DRG. To test this possibility we examined cell number in the DRG by counting the number of TrkA+ nociceptors at P0, P14, and P30, time points corresponding to key regulatory events in the survival and differentiation of nociceptors (Marmigère and Ernfors 2007). Surprisingly, we observed a significant decrease in the TrkA+ nociceptor population at P0 in *Tnfr1*$^{-/-}$ and *Tnf*$^{-/-}$ mice but, relative to WT, more TrkA+ neurons at P14 and P30 **(Figure 4A; Figure S4A)**. It is possible that the appearance of fewer TrkA+ neurons at P0 may not be due to an altered trophic threshold for survival; rather, it may have to do with altered differentiation programs. Indeed, it is established that early TrkA+ nociceptors downregulate TrkA/CGRP and upregulate Ret to become non-peptidergic nociceptors through a process that is itself dependent on the strength of NGF-TrkA signals (Luo et al. 2007). Thus, if a *Tnf* or *Tnfr1* deletion enhances NGF sensitivity in TrkA+ nociceptors, more early TrkA+ neurons would be driven toward a non-peptidergic fate. To examine this possibility, we assessed non-peptidergic cell number in the DRG by counting the number of Ret+/TrkA+ (differentiating) and IB4+ (terminally differentiated) neurons across time, as previously described (Luo et al. 2007). The number of differentiating Ret+/TrkA+ cells in *Tnfr1*$^{-/-}$ or *Tnf*$^{-/-}$ P0 DRGs was ~3 times higher than the number of differentiating neurons in WT mice **(Figure 4B-C; Figure S4B-C)**. At P14 and P30, the increase in non-peptidergic neuron number persists in *Tnfr1*$^{-/-}$ and *Tnf*$^{-/-}$ mice compared to WT **(Figure 4D; Figure S4D)**. These data suggest that TNFα-TNFR1 signals work during nociceptive differentiation to dampen the NGF-TrkA-dependent drive toward a non-peptidergic fate and loss of these signals leads to higher numbers of both peptidergic and non-peptidergic nociceptors.

(e) TNFα and TNFR1 are required for non-peptidergic nociceptor axon extension into the spinal cord and NRTN-dependent neurite outgrowth through a reverse signaling paradigm

We next sought to determine whether TNFα and TNFR1 specifically influence developmental processes in TrkA+ neurons or can more broadly affect other nociceptor pools such as Ret-expressing non-peptidergic neurons. To address this we used WT, *Tnfr1*$^{-/-}$ and *Tnf* $^{-/-}$ mice to evaluate whether non-peptidergic central projections phenocopied the robust expansion into the dorsal horn observed for peptidergic nociceptor central projections. We noted that between P14 and P30, TrkA+/CGRP+ peptidergic fibers and non-peptidergic IB4+ fibers properly segregate into laminae I-IIo and lamina IIi, respectively, in *Tnfr1*$^{-/-}$ and *Tnf* $^{-/-}$ mice (data not shown). To our surprise, however, there was approximately a 30-50% reduction in the area devoted to non-peptidergic, IB4+ axons in the dorsal horn at P14 and P30 in *Tnfr1*$^{-/-}$ or *Tnf* $^{-/-}$ mice relative to WT mice **(Figure 4E-J; Figure S4E-J)**. Having observed an increase in the number of these non-peptidergic, IB4+ cells in *Tnfr1*$^{-/-}$ and *Tnf* $^{-/-}$ mice, this finding suggests that TNFα-TNFR1 signaling is required for the maintenance of non-peptidergic central projections.

A well-established signaling pathway implicated in promoting the growth of non-peptidergic nociceptive axons is through the ligand, co-receptor, and RTK: NRTN, GFRα2, and Ret, respectively (Stucky et al. 1999, Airaksinen and Saarma 2002, Lindfors et al. 2006, Luo et al. 2007). Therefore, we next asked whether loss of TNFα or its receptor could influence Ret-dependent non-peptidergic neurite growth. To this end, we cultured E14.5 DRG explants from WT, *Tnfr1*$^{-/-}$, and *Tnf* $^{-/-}$ mice in 100 ng/mL NRTN. Surprisingly, in

response to NRTN, neurite outgrowth was significantly lower in *Tnfr1*$^{-/-}$ and *Tnf* $^{-/-}$ explants compared to WT **(Figure 4K-L; Figure S4K-L)**, consistent with *in vivo* observations of IB4-labeled axons in lamina IIi of the spinal cord. These data suggest that in contrast to the repressive effect of TNFα-TNFR1 signaling on NGF-TrkA dependent growth, TNFα and TNFR1 enhance the NRTN-GFRα2-Ret dependent neurite growth of non-peptidergic nociceptors.

(f) TNFα and TNFR1 are required to differentially regulate the excitability of peptidergic and non-peptidergic nociceptors

Nociceptors sense thermal, mechanical, and chemical stimuli through the expression of different ion channels such as the transient receptor potential (TRP) family of ion channels (Clapham 2003, Moran et al. 2011). Importantly, RTK signaling can modulate the excitability of ion channels in nociceptors. For instance, NGF-TrkA signaling can enhance the expression and sensitivity of TRP ion channels in peptidergic nociceptors (Chuang et al. 2001, Zhang et al. 2005, Ji et al. 2002, Luo et al. 2007) while NRTN-GFRα2-Ret signaling regulates expression of the ATP-gated ion channel, P2X purinoceptor 3 in non-peptidergic nociceptors (Wang et al. 2013). To test whether *Tnfr1*$^{-/-}$ and *Tnf* $^{-/-}$ peptidergic nociceptors exhibit altered excitability, we performed calcium imaging in cultured E14.5 TrkA+ sensory neurons, similar to previous studies (Liu et al. 2009). Neurons were stimulated with mustard oil, menthol, and capsaicin, which are specific agonists of the temperature sensitive TRP channels, TRPA1, TRPM8, and TRPV1, respectively (Caterina et al. 1997, Peier et al. 2002, Bandell et al. 2004). Upon stimulation with any of the three agonists, *Tnfr1*$^{-/-}$ and *Tnf* $^{-/-}$ TrkA+ neurons were hypersensitive to the chemical analogues relative to WT neurons **(Figure 5A; Figure S5A)**.

This suggests that TNFα and TNFR1 negatively regulate the excitability of TRP channels in TrkA+ nociceptors and most prominently, TRPV1, as described previously (Chuang et al. 2001, Zhang et al. 2005).

We also tested whether the excitability of non-peptidergic nociceptors is altered in the absence of TNFα or TNFR1 since NRTN is known to regulate sensitivity of P2X ion channels (Wang et al. 2013). We employed a strategy that permits recording fluorescence changes exclusively in non-peptidergic nociceptors by incubating the cultures with Alexa 568-conjugated IB4 before application of a chemical agonist **(Figure 5B)** (Gerevich *et al.* 2004). In response to ATP stimulation, *Tnfr1*$^{-/-}$ and *Tnf* $^{-/-}$ P14 IB4+ nociceptors were less excitable than WT IB4+ neurons **(Figure 5C; Figure S5B)**. Because non-peptidergic nociceptors also express TRPV1 (Chen et al. 2006, Luo et al. 2007), we tested whether a similar effect was observed after capsaicin stimulation. Indeed, IB4+ neurons from *Tnfr1*$^{-/-}$ or *Tnf* $^{-/-}$ nociceptors were hypoexcitable to capsaicin stimulation compared to WT while IB4- nociceptors were hyperexcitable **(Figure 5D; Figure S5C)**. As observed for axon growth, these data suggest opposing regulatory roles for TNFα and TNFR1 in attenuating excitability of TrkA+ peptidergic nociceptors or enhancing excitability of Ret+ non-peptidergic nociceptors.

(g) Tnf $^{-/-}$ *and Tnfr1*$^{-/-}$ *mice are hypersensitive to pain*

NGF-TrkA signaling controls nociceptor target innervation, cell survival, fate specification, excitability, and as a result, pain sensitivity thresholds (Pezet and McMahon 2006). Overactive NGF signaling therefore causes hyperalgesia largely through pathological hyperactivation of pathways regulating target innervation and excitability (Smelter and

Hochberg 2013, Hefti et al. 2006, Pezet and McMahon 2006). We found that excessive NGF signaling and loss of TNFR1 or TNFα signaling phenocopy one another with respect to hyperinnervation of the skin and spinal cord **(Figures 2-3; Figures S2-3)**, hypersensitivity to TRP agonists **(Figure 5; Figure S5)**, as well as a greater overall number of nociceptors **(Figure 4A, D; Figure S4A, D)**. Thus, we hypothesized that developmental loss of TNFα-TNFR1 signaling would translate to increased sensitivity to pain, which can be assessed by behavioral assays (for review, see Sandkühler 2009). To test this hypothesis, we first sought to precisely corroborate our calcium imaging data by subjecting the mice to a variety of different temperatures at prescribed intervals. Toward this end, we performed the tail flick assay where tails of WT or mutant mice were submerged in water ranging from 5°C to 50°C for no more than 20 seconds and the latency to tail withdrawal was measured. *Tnfr1*$^{-/-}$ and *Tnf* $^{-/-}$ mice were significantly more sensitive to every temperature examined including neutral temperatures between 25°C and 37°C **(Figure 6A)**. Hyperexcitability to all temperatures is consistent with the sensitization of TRPV1, TRPM8, and TRPA1 observed in our calcium imaging experiments **(Figure 5A; Figure S5A)** since *Tnfr1*$^{-/-}$ and *Tnf* $^{-/-}$ mice were more responsive to hot, cool, and freezing temperatures, respectively, in the behavioral assays. *Tnfr1*$^{-/-}$ and *Tnf* $^{-/-}$ mice also responded more quickly than WT in the Hargreaves radiant heat test, which applies heat with no tactile cue **(Figure 6C)**, further corroborating hypersensitivity to heat in the absence of TNFα or TNFR1. These data are consistent with the notion that TNFα-TNFR1 signaling contributes to proper perception of temperature by dampening nociceptor pain thresholds.

In addition to measuring reflexive pain, we utilized two tests that interrogate centrally-mediated hot- and cold-sensing abilities: the hot plate test and the acetone drop

test. These tests quantify grooming responses indicative of which temperatures mice perceive as noxious. For the hot-plate test we examined several temperatures ranging from mild to noxious heat. Mice lacking *Tnfr1* and *Tnf* had lower pain thresholds for heat and consequently, an altered perception of thermal stimuli when compared to WT mice **(Figure 6D)**. Both ligand and receptor null mice also displayed similar increases in grooming behaviors in the acetone drop test, which simulates cold-sensation **(Figure 6E)**. In addition to enhanced reflexive acuity to pain, *Tnfr1*$^{-/-}$ and *Tnf* $^{-/-}$ mice display skewed thresholds of which temperatures are noxious and which are not, as they confuse the distinction between mild and injurious temperatures in both tests.

To assay another form of tactile sensitivity, we tested mechanical acuity in *Tnfr1*$^{-/-}$ and *Tnf* $^{-/-}$ mice. Reflexive mechanical sensitivity can be probed with von Frey filaments of varying diameter to determine the threshold sensitivity of a mechanical force. In response to mild mechanical forces both *Tnfr1*$^{-/-}$ and *Tnf* $^{-/-}$ mice were more acutely sensitive to von Frey filament stimulation than WT **(Figure 6F)**, suggesting that TNFα-TNFR1 signaling can also shape and suppress perception of mechanical acuity in addition to reflexively- and centrally-mediated thermal pain. Thus, we propose that the TNFα-TNFR1 pathway functions to tune primary nociceptors to properly interpret painful touch and prevent increased nociceptive signal gain.

(h) Deletion of Tnfr1 rescues pain phenotypes associated with Ngf heterozygosity

Our *in vitro* and *in vivo* data demonstrate a consistent role for TNFα-TNFR1 antagonizing NGF-TrkA function. Based on these data we speculated that by modulating one pathway we might be able to correct phenotypes observed in the other. While *Ngf* $^{-/-}$ mice

die perinatally (Crowley et al. 1994), it is established that nociceptors in mice heterozygous for *Ngf* have roughly 50% less cell survival and axon growth (Crowley et al. 1994, Brennan et al. 1999). If the role of TNFα-TNFR1 signaling is to antagonize NGF-TrkA signaling in nociceptors, then we would predict that ablation of *Tnfr1* would rescue pain phenotypes that might be associated with loss of one *Ngf* allele. First, we performed an analysis of the number of TrkA+ and IB4+ nociceptors in the P14 L4 or L5 DRG of *Tnfr1*$^{+/-}$, *Tnfr1*$^{+/-}$;*Ngf* $^{+/-}$, and *Tnfr1*$^{-/-}$;*Ngf* $^{+/-}$ mice. Consistent with the loss of 50% of target-derived NGF, *Tnfr1*$^{+/-}$;*Ngf* $^{+/-}$ mice exhibited roughly 50% fewer TrkA+ and IB4+ neurons at P14 compared to *Tnfr1*$^{+/-}$ mice **(Figure 7A)**. *Tnfr1*$^{-/-}$;*Ngf* $^{+/-}$ mice, by contrast, exhibited TrkA+ and IB4+ neuron numbers similar to *Tnfr1*$^{+/-}$, which suggests that loss of *Tnfr1* increases the NGF-sensitivity of TrkA+ nociceptors, thereby rescuing the impaired cell survival caused by *Ngf* heterozygosity.

Next, we analyzed the central projections into the spinal cord dorsal horn in *Tnfr1*$^{+/-}$, *Tnfr1*$^{+/-}$;*Ngf* $^{+/-}$, and *Tnfr1*$^{-/-}$;*Ngf* $^{+/-}$ mice. As expected, there was roughly a 50% decrease in the area occupied by CGRP+ fibers in the dorsal horn at P14 in *Tnfr1*$^{+/-}$;*Ngf* $^{+/-}$ mice relative to *Tnfr1*$^{+/-}$ mice **(Figure 7B-E)**. Homozygous *Tnfr1* deletion can rescue this fiber deficiency in *Tnfr1*$^{-/-}$;*Ngf* $^{+/-}$ mice, providing additional evidence for functional antagonism between TNFR1 and TrkA *in vivo*. Although the number of peptidergic and non-peptidergic nociceptors in the DRG is rescued by homozygous elimination of *Tnfr1*, the area occupied by non-peptidergic axons in the dorsal horn was identical between *Tnfr1*$^{+/-}$/*Ngf* $^{+/-}$ and *Tnfr1*$^{-/-}$/*Ngf* $^{+/-}$ mice **(Figure 7B, F-H)**. This is consistent with the idea that TNFR1 positively regulates the maintenance of IB4+ fibers and supports the claim that TNFR1 is required for the full elaboration of non-peptidergic axons through cooperation with NRTN signaling.

We next examined innervation of glabrous skin from the hindpaw footpad of P14 *Tnfr1*$^{+/-}$, *Tnfr1*$^{+/-}$;*Ngf* $^{+/-}$, and *Tnfr1*$^{-/-}$;*Ngf* $^{+/-}$ mice by quantifying the number of CGRP+ axons projecting into the epidermis **(Figure 7I-L)**. This analysis revealed a 50% reduction in epidermal innervation by CGRP+ fibers in *Tnfr1*$^{+/-}$/*Ngf*$^{+/-}$, compared to *Tnfr1*$^{+/-}$. Interestingly, the skin of *Tnfr1*$^{-/-}$;*Ngf* $^{+/-}$ mice exhibited ~20% more fibers than *Tnfr1*$^{+/-}$ mice, suggesting that TNFR1 potently opposes NGF-mediated peripheral axon growth of peptidergic fibers.

Finally, we performed behavioral analyses on *Tnfr1*$^{+/-}$, *Tnfr1*$^{+/-}$;*Ngf* $^{+/-}$, and *Tnfr1*$^{-/-}$;*Ngf* $^{+/-}$ mice. *Tnfr1*$^{+/-}$;*Ngf* $^{+/-}$ mice were moderately less sensitive than *Tnfr1*$^{+/-}$ mice when performing the hot plate task at 50, 52.5, and 55°C **(Figure 7M)**. As expected, the latency to onset of rapid, sustained grooming was reduced in *Tnfr1*$^{-/-}$;*Ngf* $^{+/-}$ mice when compared to the less sensitive *Tnfr1*$^{+/-}$;*Ngf* $^{+/-}$ mice. These loss-of-function data indicate that ablation of TNFR1 can sensitize TrkA signaling in nociceptors and thereby compensate for reduced NGF availability. We conclude that the normal function of the TNFα-TNFR1 pathway during development is to functionally repress NGF-TrkA signaling, and in turn, counter nociception *in vivo*.

III. Discussion

This study describes dual roles for TNFα and TNFR1 signaling in the coordination of peptidergic and non-peptidergic nociceptive circuits during PNS development. We demonstrate that, as early as E14.5 and as late as P30, TNFR1 is required to negatively regulate the growth, differentiation, and excitability of peptidergic nociceptors. In contrast, TNFR1 signaling is required for the full axonal outgrowth and excitability of non-peptidergic nociceptors between P14 and P30. We propose that these differential functions are

principally dependent on the complement of RTK signaling and growth factor responsiveness resident in different nociceptor populations, specifically NGF-TrkA and NRTN-GFRα2-Ret in peptidergic and non-peptidergic nociceptors, respectively **(Figure 8A-B)**.

TNFα-TNFR1 attenuates NGF-TrkA dependent constructive processes in peptidergic nociceptors

Our *in vivo* and *in vitro* results provide evidence that TNFα and TNFR1 are required for proper development of nociceptive circuits through antagonism of NGF-TrkA signaling. Several lines of evidence support this assertion including: (1) *In vivo*, *Tnfr1*$^{-/-}$ and *Tnf* $^{-/-}$ mice exhibit an increased density of nociceptive fibers both peripherally and centrally **(Figures 2A-D; Figure S2A-D)**. (2) *In vitro, Tnfr1*$^{-/-}$ and *Tnf* $^{-/-}$ neurons are more sensitive to NGF-mediated growth both in compartmentalized chambers and in explants **(Figures 2E-G; Figure S2E-G)**. (3) *In vitro* calcium imaging suggests that TNFα-TNFR1 signaling normally suppresses the sensitivity of several TRP channels in TrkA+ peptidergic nociceptors since TrkA+ nociceptors are hyperexcitable in the absence of TNFα-TNFR1 signaling **(Figure 5A; Figure S5A).** (4) We show that homozygous deletion of *Tnfr1* is sufficient to compensate for axon growth and behavioral pain deficits caused by the loss of a single *Ngf* allele **(Figure 7)**. Together, these results suggest that TNFα is expressed by sensory neurons and their targets, which signals through TNFR1 in an autocrine or paracrine manner, in order to antagonize NGF-TrkA signaling.

Our findings that TNFα-TNFR1 signaling and NGF-TrkA signaling mutually oppose one another in nociceptors are analogous to the function of p75NTR in sympathetic neurons

(Glebova and Ginty 2005, Deppmann et al. 2008). For instance, p75NTR prevents axon overgrowth (Yeo et al. 1997, Singh et al. 2008), modulates electrical properties (Luther and Birren 2009), and expedites developmental cell death (Deppmann et al. 2008) in sympathetic neurons. While p75NTR does not appear to play this role in sensory neurons (Lee et al. 1992), we suggest that TNFα and TNFR1 may have taken on the role of being functionally antagonistic toward NGF-TrkA dependent axon growth into peripheral and central targets, excitability, cell survival, and differentiation. It is intriguing to speculate however, that other TNFR family members might also serve as pro-refinement mechanisms in sensory neurons. DR6 is one likely candidate given its robust enrichment in the DRG **(Figure S1A)** and its pronounced role in sensory neuron degeneration (Nikolaev et al. 2009). One avenue of future investigation will be to ask whether TNFR family members can cooperate to facilitate pro-refinement functions in the somatosensory system.

(a) Cell fate specification of TrkA+ sensory neurons is coordinated by TNFα-TNFR1 signaling

All newly born nociceptors are TrkA+ but mature to become several diverse subpopulations expressing various combinations of the RTKs TrkA, Ret, and Met during adulthood (Lallemend and Ernfors 2012, Liu and Ma 2011, Gascon et al. 2010, Luo et al. 2007). These fate specification events are reported to be dependent on hierarchal NGF-TrkA modulation of the RTK, Ret, and the transcription factor, Runx1 (Lallemend and Ernfors 2012, Gascon et al. 2010, Luo et al. 2007, Chen C et al. 2006). Thus, it stands to reason that perturbing TrkA signals in developing sensory neurons would perturb fate specification. How then is such remarkable diversity coordinated from the standpoint of an early TrkA-

expressing nociceptor? We propose that TNFR1 plays a pivotal role in the specification of different nociceptor subtypes based on the following observations: (1) Elimination of TNFα-TNFR1 signaling leads to higher numbers of TrkA+ nociceptors in adulthood, consistent with previous reports that TNFα serves a death-promoting developmental role in sensory neurons **(Figure 4A; Figure S4A)** (Barker et al. 2001). (2) Loss of TNFR1 or TNFα also results in a higher proportion of nociceptors moving toward a non-peptidergic fate commitment at P0 **(Figure 4B-C; Figure S4B-C)**. (3) Consistent with this idea, at P14 and P30 there are more IB4+ neurons in *Tnfr1* and *Tnf* knockout animals than WT mice in the L4/L5 DRG **(Figure 4D; Figure S4D)**.

Previous work has demonstrated that loss of key transcription factors impairs differentiation and function of sensory neurons (Chen A et al. 2006, Chen C et al. 2006, Wende et al. 2012). While the importance of TrkA in regulating nociceptor differentiation has already been established (Luo et al. 2007), to our knowledge TNFR1 is the only non-RTK reported to influence sensory neuron fate specification. We find that loss of TNFα-TNFR1 signaling is more akin to enhancement of TrkA-dependent differentiation as more non-peptidergic nociceptors are generated in the absence of TNFα or TNFR1. Importantly, while we specifically focus on the development of non-peptidergic nociceptors derived from TrkA+ precursors, there are several other distinct populations of TrkA-derived cells that are likely affected by loss of TNFα or TNFR1 such as those expressing *mrg* family members regulating pain, itch, or even low threshold mechanosensation (Dong et al. 2001, Liu et al. 2009, Vrontou et al. 2013, Abraira and Ginty 2013). In future studies it will be interesting to examine how TNFα and TNFR1 influence the development and specification of several important sensory neuron subtypes critical for varied modes of tactile perception.

(b) TNFα and TNFR1 enhance non-peptidergic nociceptor growth and excitability

Despite increases in the number of IB4+ neurons in mice lacking TNFα or TNFR1 signaling, it appears that the role of this signaling is not antagonistic toward but cooperative with Ret signaling in non-peptidergic nociceptors. Several lines of evidence support this synergistic relationship including: (1) *In vivo*, a reduction in IB4+ fibers occupying lamina IIi at P14 and P30, despite the presence of more non-peptidergic cell bodies in the DRG at P14 and P30 **(Figure 4E-J; Figure S4E-J)**. (2) *In vitro,* DRG explants from *Tnfr1*$^{-/-}$ or *Tnf* $^{-/-}$ mice display impaired axon outgrowth in response to NRTN **(Figure 4K-L; Figure S4K-L)**. (3) *In vitro* calcium imaging assays reveal that *Tnf* $^{-/-}$ and *Tnfr1*$^{-/-}$ non-peptidergic nociceptors are hypoexcitable to acute ATP and capsaicin stimulation **(Figure 5C-D; Figure S5B-C)**. (4) The inability of a *Tnfr1* deletion to rescue deficient non-peptidergic central projections to lamina IIi caused by *Ngf* heterozygosity **(Figure 7B, F-H)**. These results point to a dichotomous function for TNFα and TNFR1 signals in two populations of functionally disparate neurons and suggest that TNFα and TNFR1 may modulate growth and excitability via similar mechanisms (Stucky et al. 1999, Lindfors et al. 2006).

What is the molecular basis for the dichotomous role of TNFα and TNFR1 signaling in the context of RTK mediated nociceptor development? One plausible mechanism could be that TNFR1 physically interacts with TrkA and Ret to influence downstream pathways. While cross-talk between Trk and TNFR family members is established, the mechanism is, at present, unclear (Chao 2003, Wehrman et al. 2007). Similarly, Ret functions as a co-receptor for GFRα subunits and ephrins (Airaksinen and Saarma 2002, Bonanomi et al. 2012), suggesting that TNFR1 could serve as another co-receptor in the context of nociceptive

neurons to enhance non-peptidergic growth and excitability. Alternatively, TNFR1 could interact with TrkA and Ret downstream by biasing peptidergic and non-peptidergic nociceptors toward desensitizing or sensitizing pathways, respectively, mediated by Jun kinase or NF-κB, for instance (Chang et al. 2006). Another possible explanation might be reverse signaling by soluble TNFR1 through membrane-bound TNF to promote growth and excitability in the non-peptidergic population but forward signaling by soluble TNF through membrane-bound TNFR1 to inhibit growth and excitability in the peptidergic population (Barker et al. 2001, Sun and Fink 2007, Kisiswa et al. 2013). Although further studies on these possible mechanisms are necessary, it is a compelling idea to consider the number of permutations of TNFR family members antagonizing or synergizing with different RTKs to promote vastly different functional outcomes such as what we observe in peptidergic (TrkA) and non-peptidergic (Ret) nociceptors. As such, our findings likely extend beyond neuronal populations specifically, and to RTK and TNFR family member function, generally.

(c) NGF-TrkA signaling is gated by TNFα-TNFR1 signaling, which suppresses pain

Our data suggest that TNFR1 acts as a gatekeeper on nociceptive neurons where it exerts control over several processes gating stimulus perception. Importantly, our data also imply that TNFα-TNFR1 signaling within nociceptors is, in turn, controlled by the levels of TNFα produced by tissues that nociceptors innervate such as the skin and spinal cord. TNFα-TNFR1 signals modify nociceptor information processing by attenuating NGF-TrkA signals and refining components of the primary nociceptive circuit such that nociceptors properly interpret painful touch. Our study and findings from other groups have demonstrated that elimination of NGF or TrkA signaling results in nociceptive impairment (Crowley et al. 1994,

Silos-Santiago et al. 1995, Indo et al. 1996). Conversely, excessive NGF-TrkA activation causes nociceptor sensitization (Pezet and McMahon 2006, Lane et al. 2010). Thus, deletion of *Tnf* or *Tnfr1* is analogous to increasing the sensitivity of nociceptors to NGF stimulation, effectively increasing the gain in pain signals that are transmitted to the CNS, as suggested previously **(Figure 6)** (Woolf and Salter 2000). In support of this notion, we find that loss of TNFR1 can rescue the defective nociceptive perception observed in mice heterozygous for *Ngf*. This rescue can be observed for cell number, central projection, and peripheral innervation density as well as behavior **(Figure 7)**.

This study furthers the important yet somewhat nascent concept emerging in studies of the PNS describing how antagonistic signals regulate the development of the peripheral nervous system, and by extension, sensory perception. While the idea that TNFR family members negatively regulate the Trk family of RTKs isn't a new one, the argument that the infamously pro-inflammatory TNFα-TNFR1 pathway opposes pain perception is novel. In fact, we report that nearly every major hallmark of the NGF-TrkA pathway is augmented when *Tnfr1* or *Tnf* is deleted, suggesting a broad, general, and robust antagonism of TrkA signaling in nociceptors. Surprisingly, while TNFα and TNFR1 are analgesic signals in TrkA+ nociceptors, they serve an algesic role in Ret+ nociceptors, which highlights the importance of molecular context in the formation of developing neural circuits.

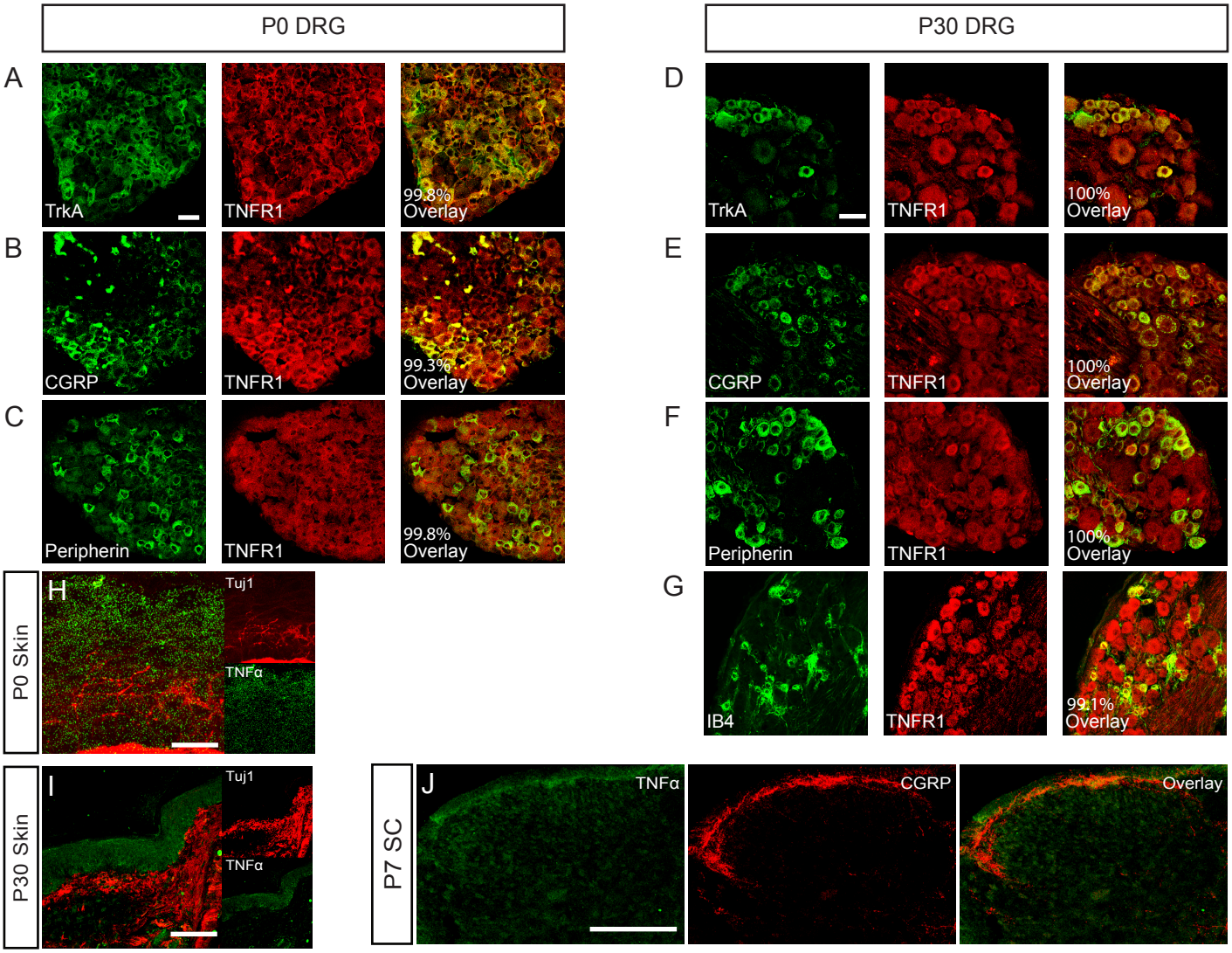
P0 DRG
P30 DRG
A
TrkA
TNFR1
99.8%
Overlay
B
CGRP
TNFR1
99.3%
Overlay
C
Peripherin
TNFR1
99.8%
Overlay
D
TrkA
TNFR1
100%
Overlay
E
CGRP
TNFR1
100%
Overlay
F
Peripherin
TNFR1
100%
Overlay
G
IB4
TNFR1
99.1%
Overlay
P0 Skin
H
Tuj1
TNFα
P30 Skin
I
Tuj1
TNFα
P7 SC
J
TNFα
CGRP
Overlay

Figure 1

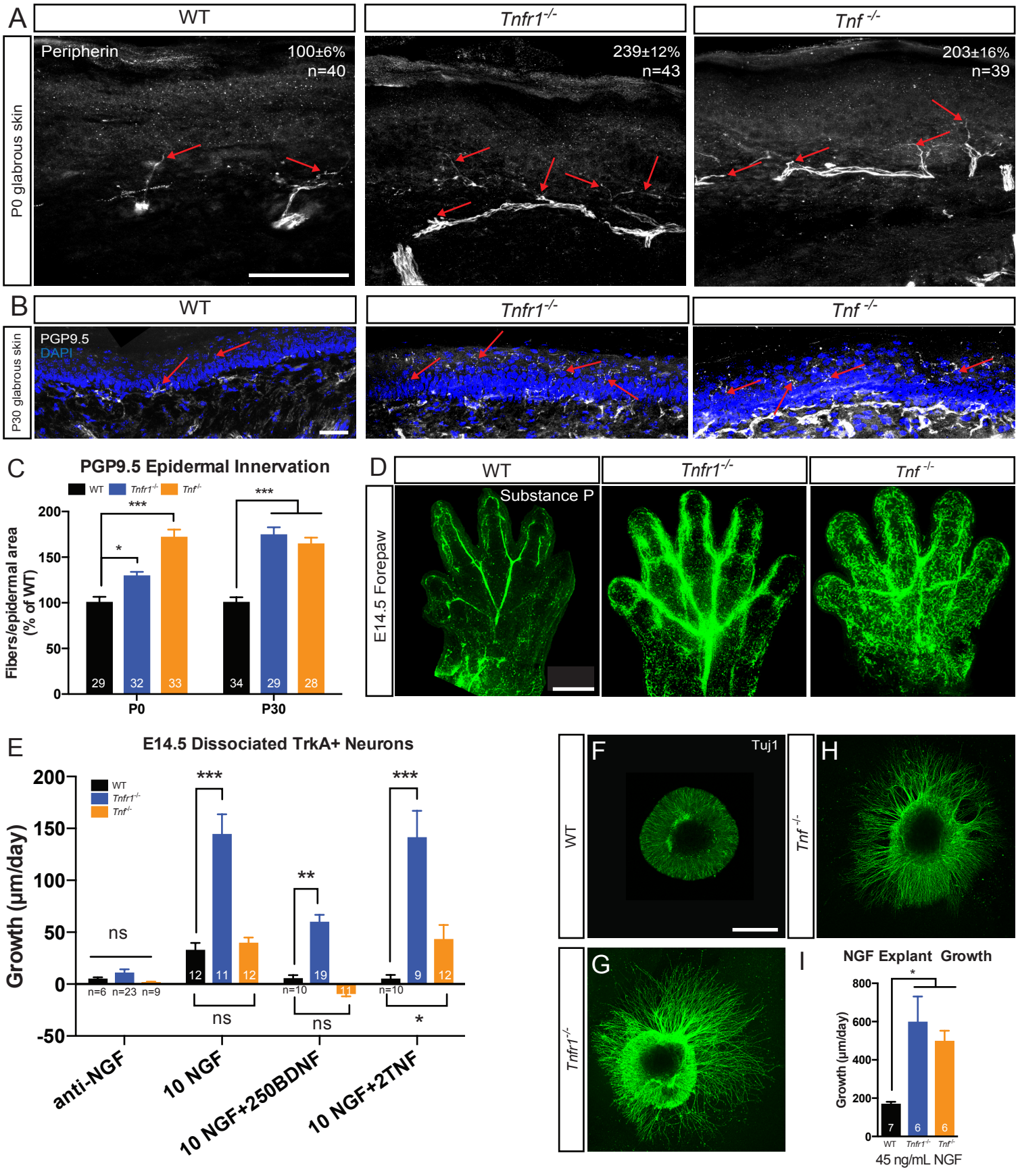
A
WT
Tnfr1-/-
Tnf -/-
P0 glabrous skin
Peripherin
100±6%
n=40
239±12%
n=43
203±16%
n=39
B
WT
Tnfr1-/-
Tnf -/-
P30 glabrous skin
PGP9.5
DAPI
C
PGP9.5 Epidermal Innervation
WT
Tnfr1-/-
Tnf-/-
Fibers/epidermal area (% of WT)
200
150
100
50
0
*
***
***
29
32
33
34
29
28
P0
P30
D
WT
Tnfr1-/-
Tnf -/-
E14.5 Forepaw
Substance P
E
E14.5 Dissociated TrkA+ Neurons
WT
Tnfr1-/-
Tnf-/-
Growth (µm/day)
200
150
100
50
0
-50
ns
***
**
***
12
11
12
19
11
9
12
n=6
n=23
n=9
n=10
n=10
ns
ns
*
anti-NGF
10 NGF
10 NGF+250BDNF
10 NGF+2TNF
F
Tuj1
WT
H
Tnf -/-
G
Tnfr1-/-
I
NGF Explant Growth
Growth (µm/day)
800
600
400
200
0
*
7
6
6
WT
Tnfr1-/-
Tnf-/-
45 ng/mL NGF

Figure 2

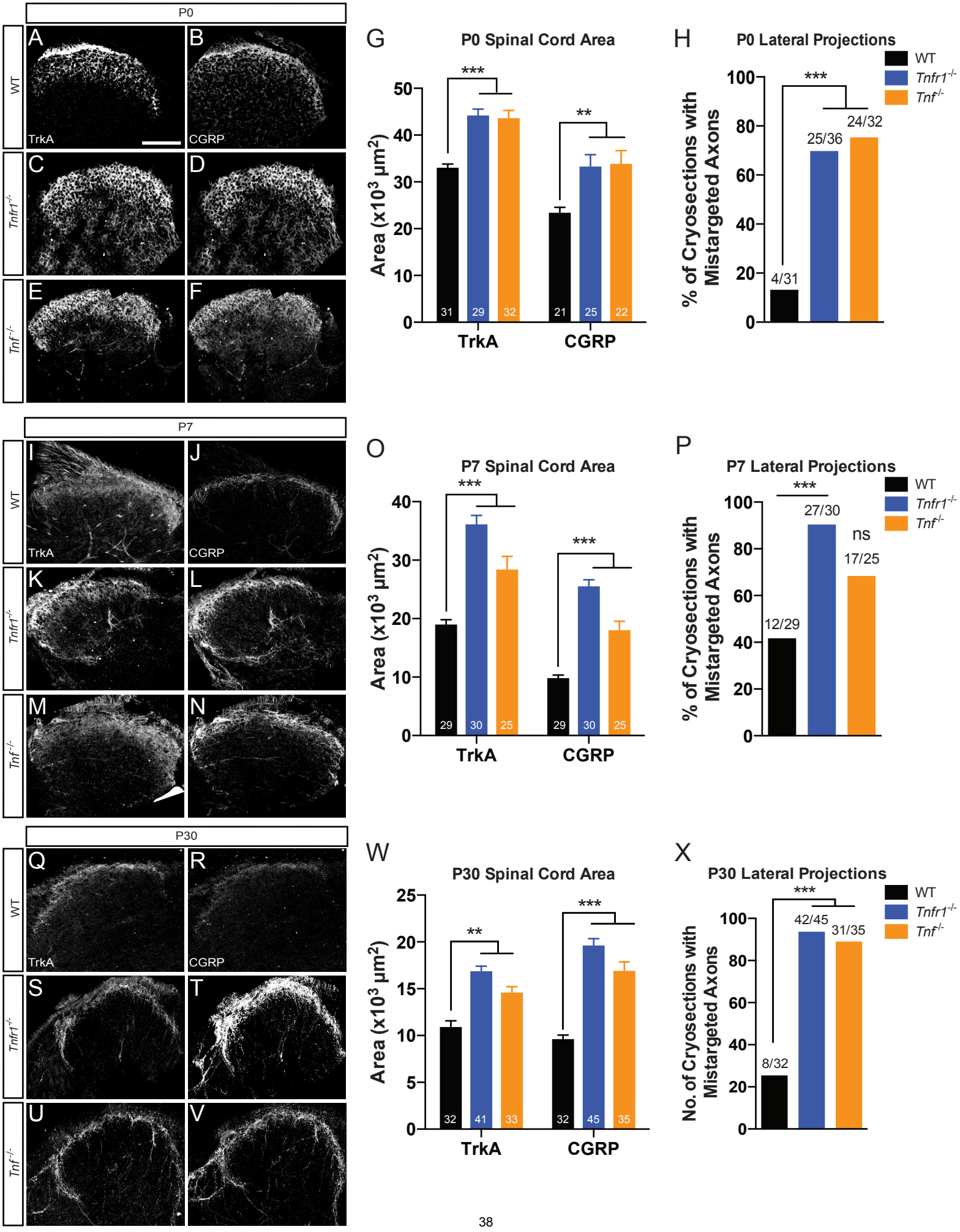
P0
A
B
C
D
E
F
WT
Tnfr1-/-
Tnf-/-
TrkA
CGRP
G
P0 Spinal Cord Area
Area (x10³ µm²)
***
**
31
29
32
21
25
22
TrkA
CGRP
H
P0 Lateral Projections
% of Cryosections with Mistargeted Axons
***
4/31
25/36
24/32
WT
Tnfr1-/-
Tnf-/-
P7
I
J
K
L
M
N
O
P7 Spinal Cord Area
29
30
25
P
P7 Lateral Projections
12/29
27/30
ns
17/25
P30
Q
R
S
T
U
V
W
P30 Spinal Cord Area
32
41
33
45
35
X
P30 Lateral Projections
No. of Cryosections with Mistargeted Axons
8/32
42/45
31/35

Figure 3

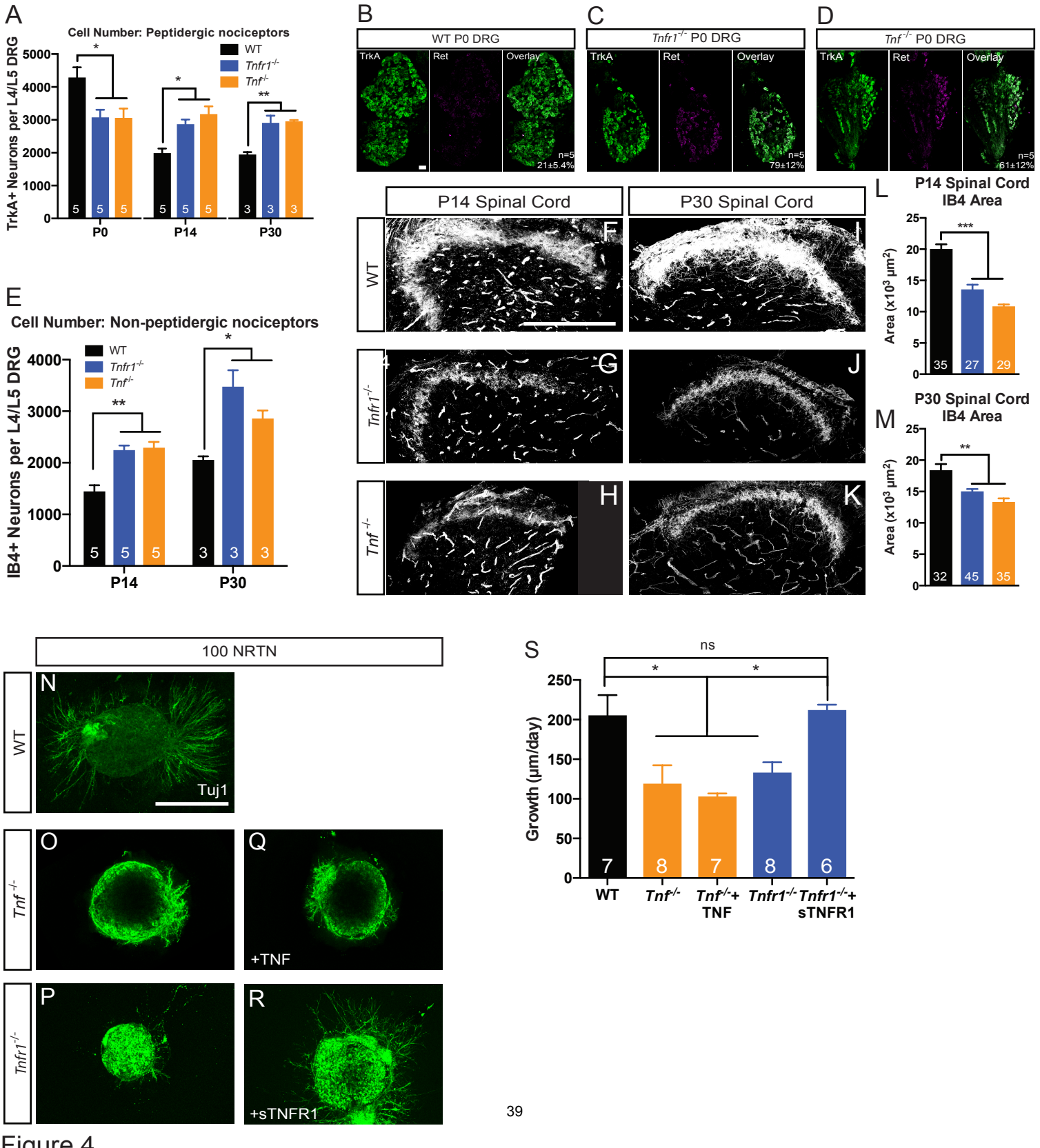
A
Cell Number: Peptidergic nociceptors
TrkA+ Neurons per L4/L5 DRG
WT
Tnfr1-/-
Tnf-/-
P0
P14
P30
B
WT P0 DRG
C
Tnfr1-/- P0 DRG
D
Tnf-/- P0 DRG
TrkA
Ret
Overlay
n=5
21±5.4%
79±12%
61±12%
E
Cell Number: Non-peptidergic nociceptors
IB4+ Neurons per L4/L5 DRG
P14 Spinal Cord
P30 Spinal Cord
F
G
H
I
J
K
L
P14 Spinal Cord IB4 Area
Area (x10³ µm²)
M
P30 Spinal Cord IB4 Area
100 NRTN
N
Tuj1
O
P
Q
+TNF
R
+sTNFR1
S
Growth (µm/day)
WT
Tnf-/-
Tnf-/-+ TNF
Tnfr1-/-
Tnfr1-/-+ sTNFR1
ns

Figure 4

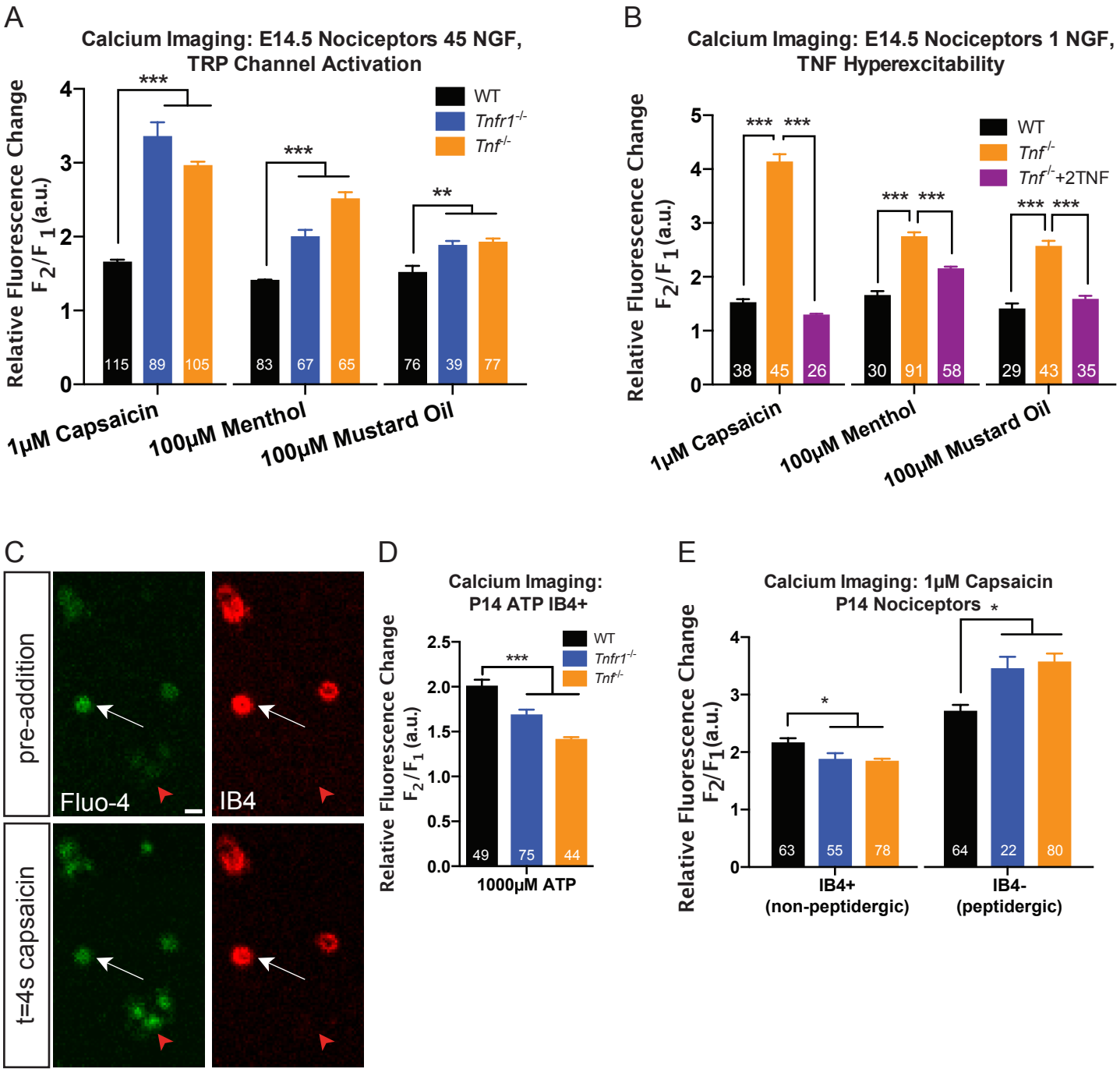
A
Calcium Imaging: E14.5 Nociceptors 45 NGF, TRP Channel Activation
Relative Fluorescence Change F2/F1 (a.u.)
WT
Tnfr1-/-
Tnf-/-
***
***
**
115
89
105
83
67
65
76
39
77
1μM Capsaicin
100μM Menthol
100μM Mustard Oil
B
Calcium Imaging: E14.5 Nociceptors 1 NGF, TNF Hyperexcitability
Relative Fluorescence Change F2/F1 (a.u.)
WT
Tnf-/-
Tnf-/-+2TNF
*** ***
*** ***
*** ***
38
45
26
30
91
58
29
43
35
1μM Capsaicin
100μM Menthol
100μM Mustard Oil
C
pre-addition
t=4s capsaicin
Fluo-4
IB4
D
Calcium Imaging: P14 ATP IB4+
Relative Fluorescence Change F2/F1 (a.u.)
WT
Tnfr1-/-
Tnf-/-
***
49
75
44
1000μM ATP
E
Calcium Imaging: 1μM Capsaicin P14 Nociceptors
Relative Fluorescence Change F2/F1(a.u.)
*
*
63
55
78
64
22
80
IB4+ (non-peptidergic)
IB4- (peptidergic)

Figure 5

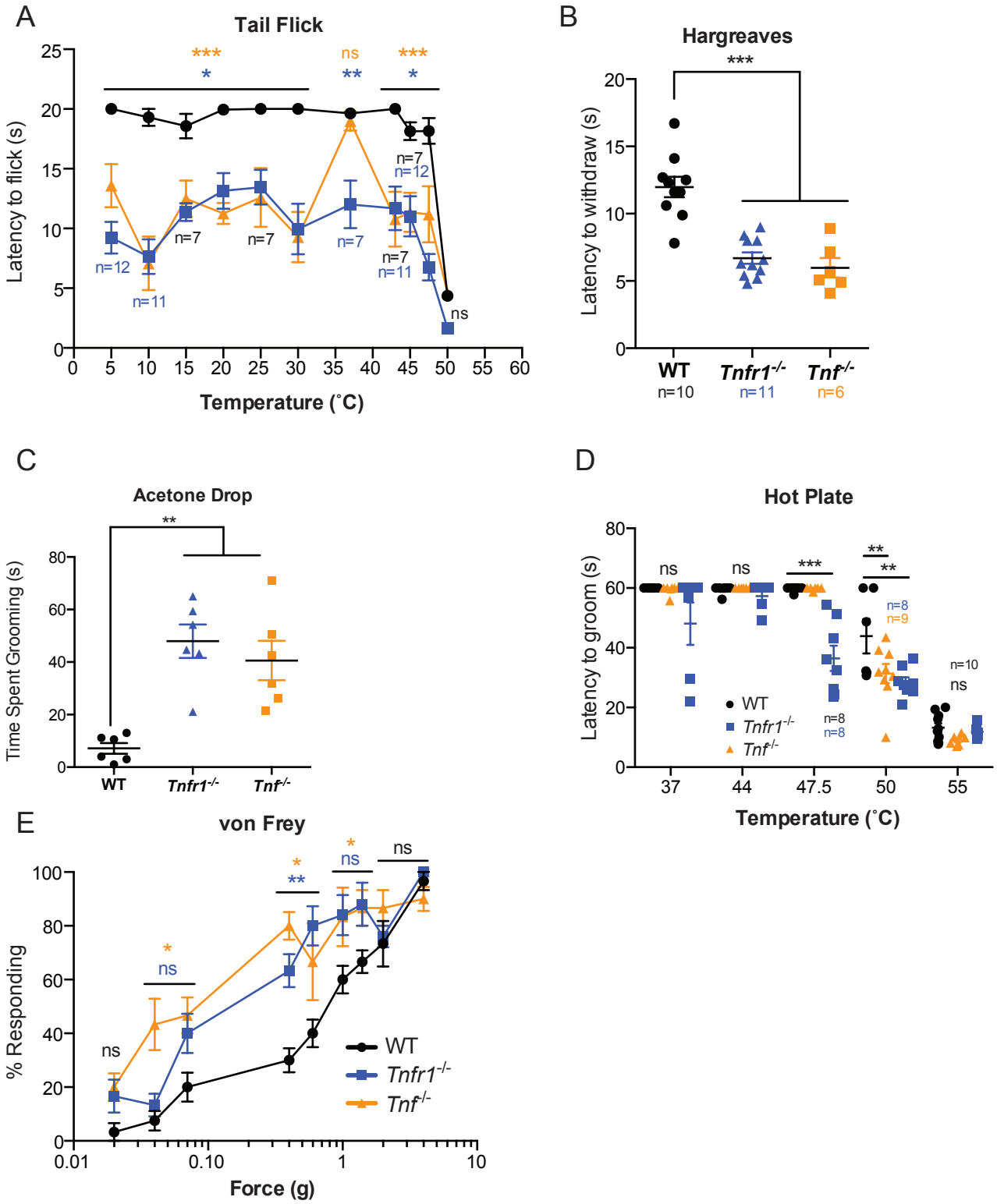
A
Tail Flick
Latency to flick (s)
Temperature (˚C)
B
Hargreaves
Latency to withdraw (s)
WT
n=10
Tnfr1-/-
n=11
Tnf-/-
n=6
C
Acetone Drop
Time Spent Grooming (s)
D
Hot Plate
Latency to groom (s)
Temperature (˚C)
E
von Frey
% Responding
Force (g)

Figure 6

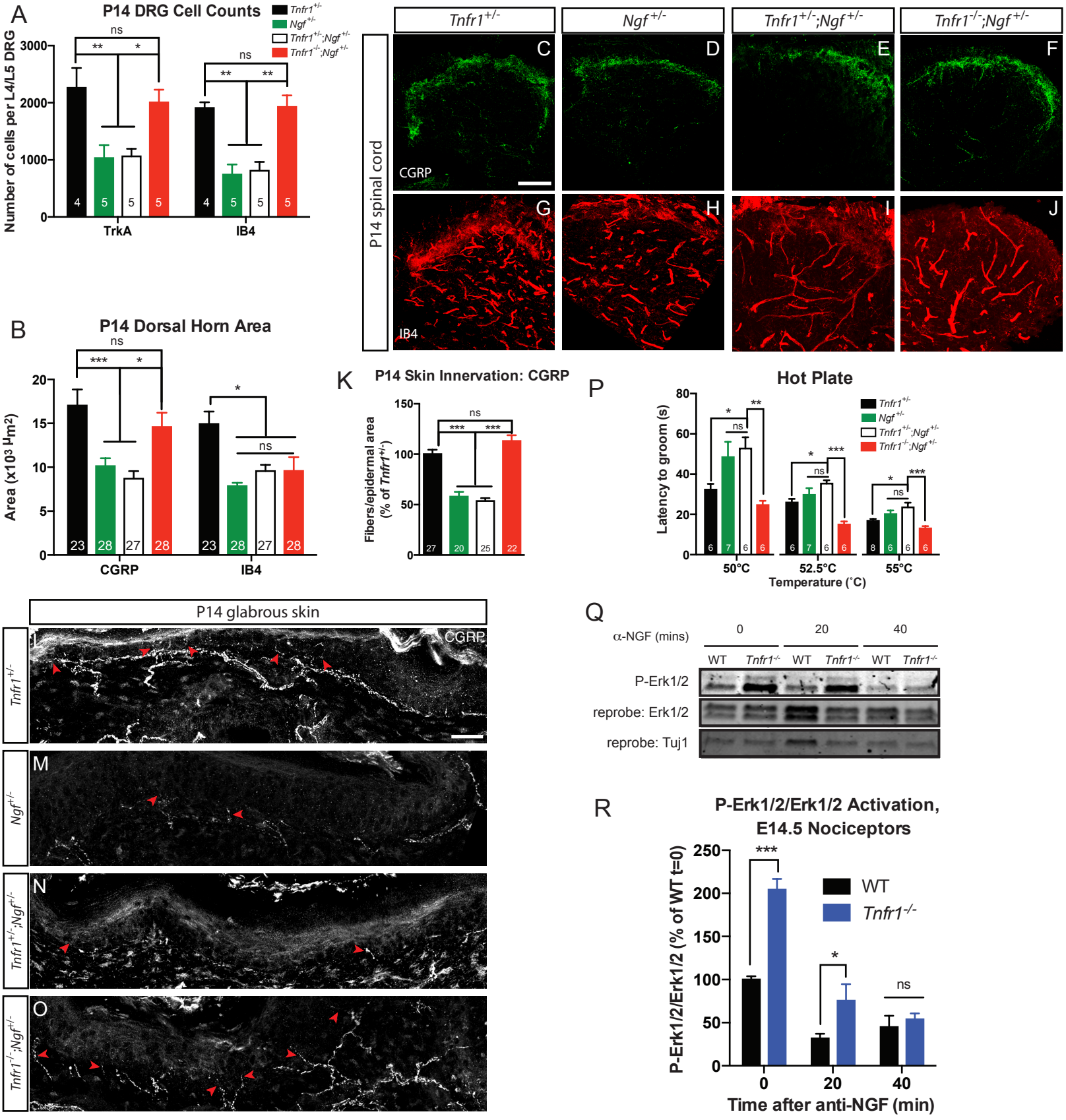
A
P14 DRG Cell Counts
Tnfr1+/-
Ngf+/-
Tnfr1+/-;Ngf+/-
Tnfr1-/-;Ngf+/-
Number of cells per L4/L5 DRG
ns
**
*
**
**
TrkA
IB4
B
P14 Dorsal Horn Area
Area (x10³ µm²)
***
CGRP
IB4
P14 spinal cord
CGRP
IB4
C
D
E
F
G
H
I
J
K
P14 Skin Innervation: CGRP
Fibers/epidermal area (% of Tnfr1+/-)
P
Hot Plate
Latency to groom (s)
50°C
52.5°C
55°C
Temperature (°C)
P14 glabrous skin
CGRP
L
M
N
O
Q
α-NGF (mins)
0
20
40
WT
Tnfr1-/-
P-Erk1/2
reprobe: Erk1/2
reprobe: Tuj1
R
P-Erk1/2/Erk1/2 Activation, E14.5 Nociceptors
P-Erk1/2/Erk1/2 (% of WT t=0)
Time after anti-NGF (min)

Figure 7

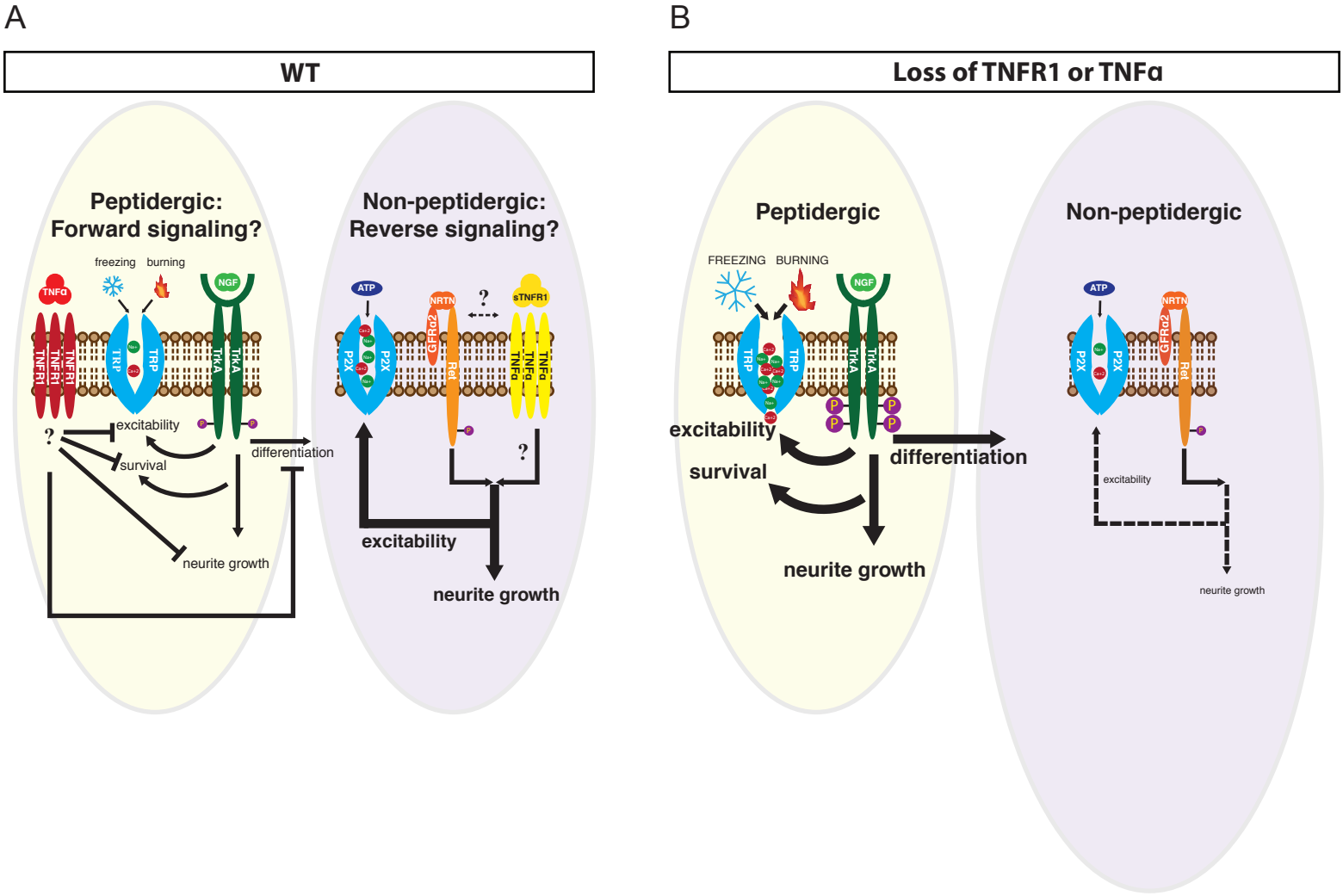
A
WT
Peptidergic:
Forward signaling?
freezing
burning
TNFα
NGF
TNFR1
TRP
TrkA
excitability
survival
differentiation
neurite growth
Non-peptidergic:
Reverse signaling?
ATP
P2X
NRTN
GFRα2
Ret
sTNFR1
TNFα
excitability
neurite growth
B
Loss of TNFR1 or TNFα
Peptidergic
FREEZING
BURNING
excitability
survival
differentiation
neurite growth
Non-peptidergic
excitability
neurite growth

Figure 8

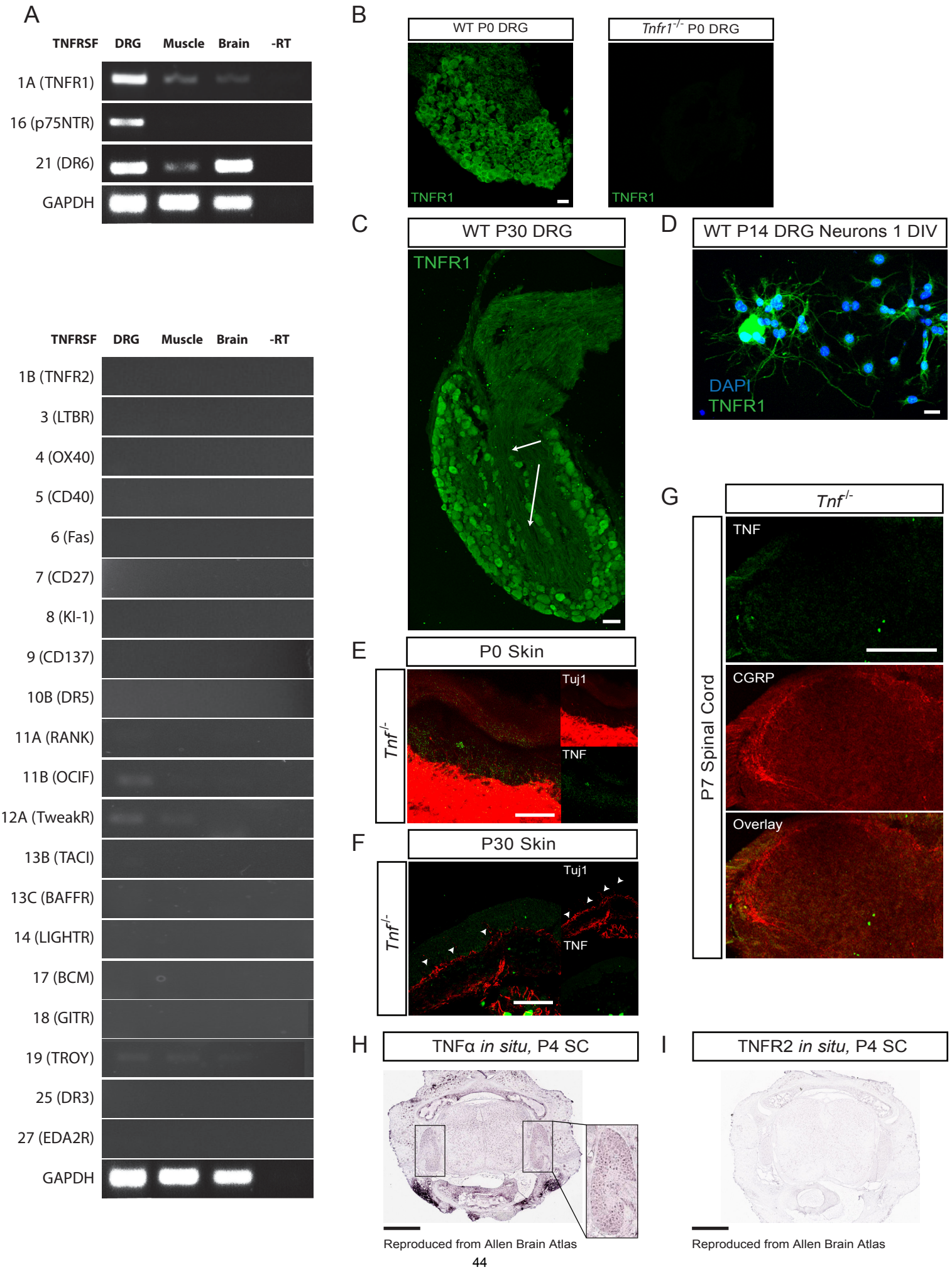

Figure S1, related to Figure 1

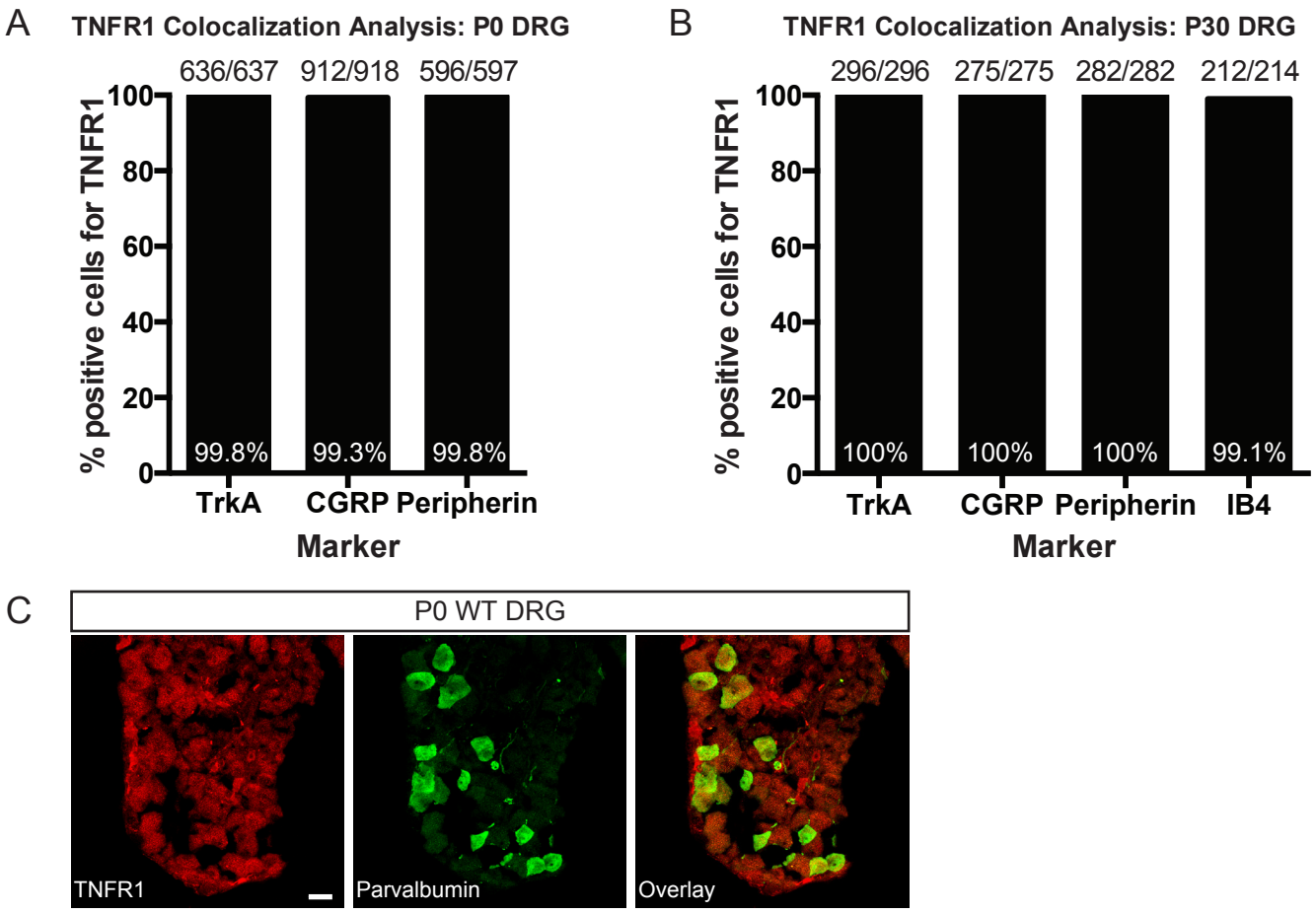

Figure S2, related to Figure 1

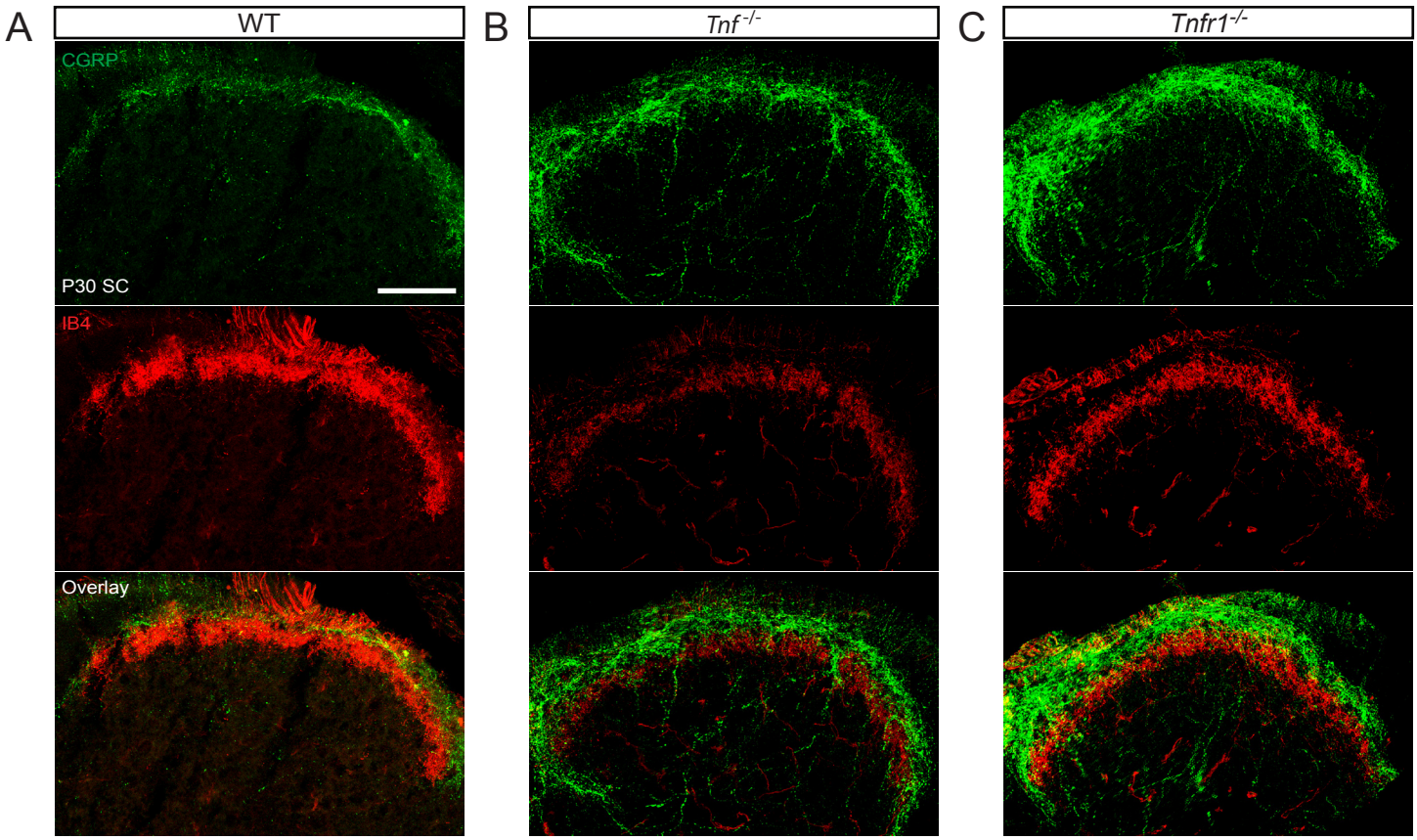

Figure S3, related to Figure 3

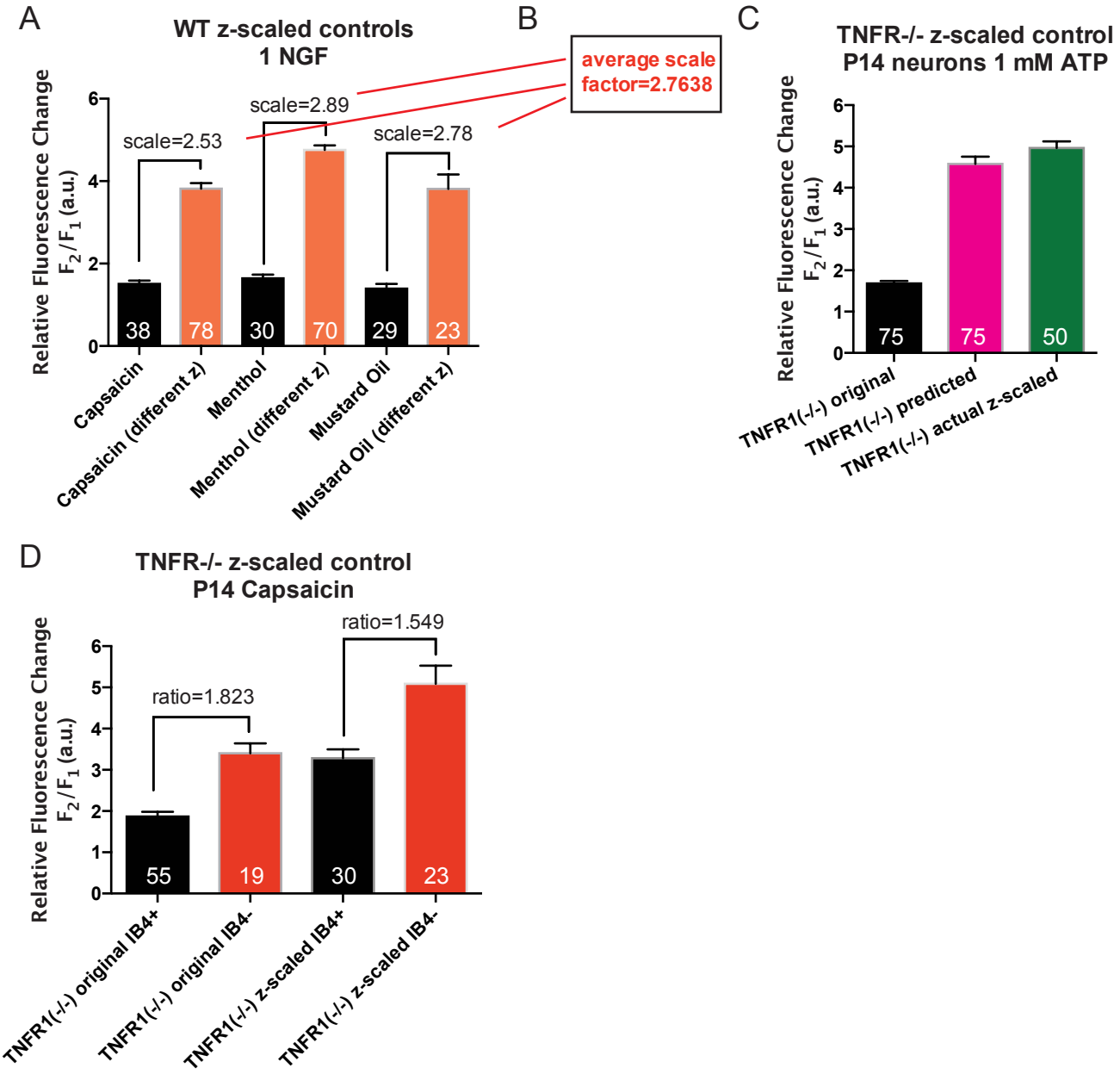

Figure S4, related to Figure 5

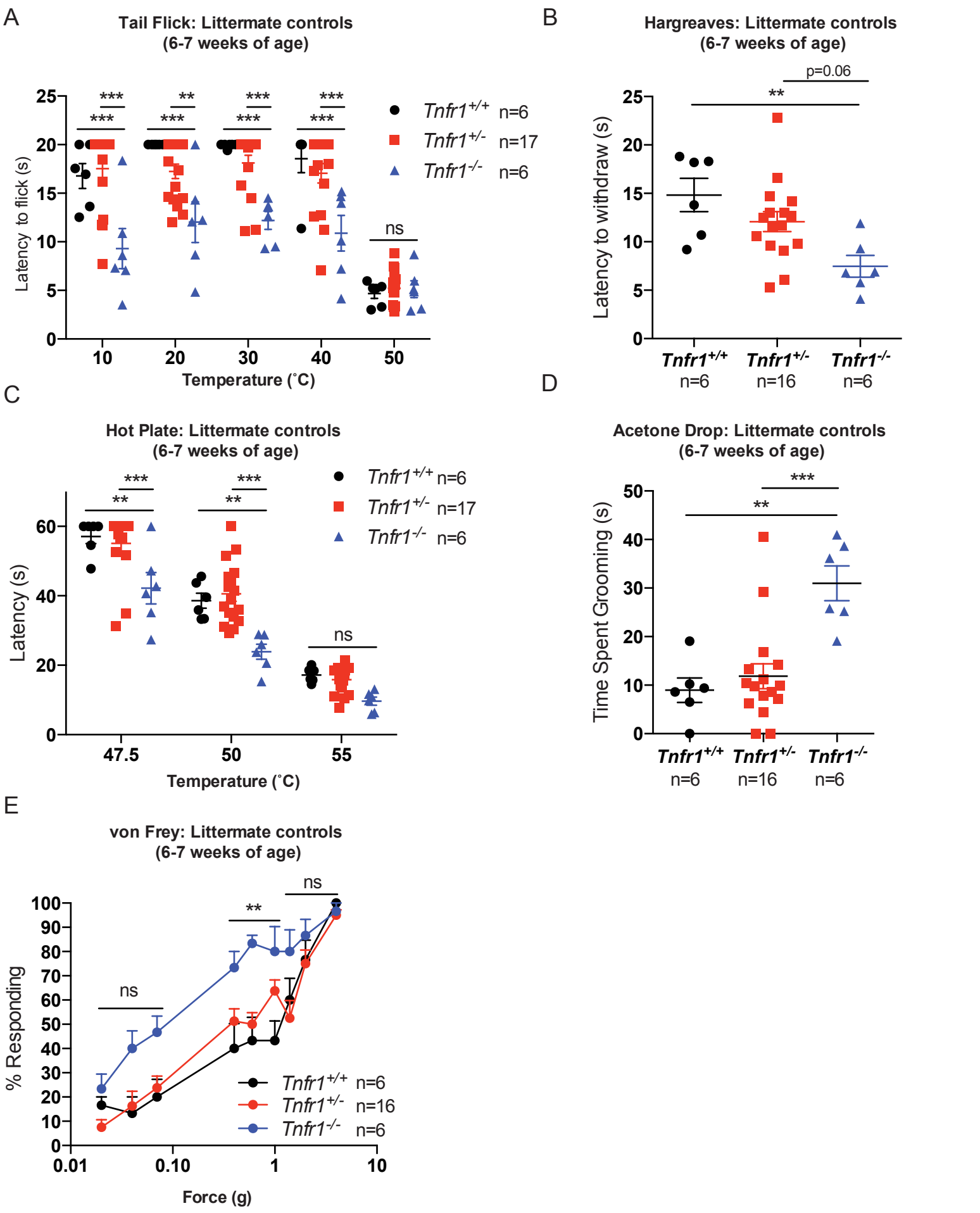

Figure S5, related to Figure 6

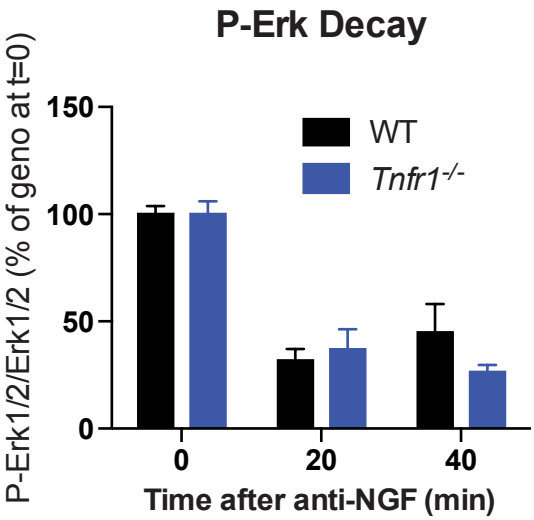

Figure S6, related to Figure 7

V. Figure Legends

Figure 1: TNFR1 is expressed by nociceptive neurons and TNFα is expressed in nociceptor targets

(A-C) Quantification of TNFR1 colocalization the nociceptive markers TrkA, CGRP, and peripherin in the P0 DRG. Scale bar represents 30 μm.

(D-G) Quantification of TNFR1 colocalization with the same nociceptive markers above plus IB4 as a marker of non-peptidergic nociceptors in the P30 DRG. Scale bar represents 60 μm.

(H-I) TNFα is enriched mainly in the epidermis at P0 and P30. Scale bar represents 120 μm.

(J) Expression of TNFα in the marginal zone and dorsal horn neurons of the spinal cord. Scale bar represents 150 μm.

Figure 2: *Tnfr1*$^{-/-}$ and *Tnf* $^{-/-}$ nociceptive axons hyperinnervate the skin and are hypersensitive to NGF-dependent growth

(A) Peripherin immunostaining of hind-paw thin glabrous skin. Arrows point to axons sprouting into the cutaneous field. Scale bar represents 50 μm. Quantification shown is peripherin+ fiber cutaneous field density normalized as percent of WT mean. 5 animals of each genotype examined.

(B-C) PGP9.5 immunostaining of thin glabrous skin and quantification of epidermal innervation. (B) P30 thin glabrous skin. Arrows point to invading fibers. (C) Quantification of the number of PGP9.5 neurites crossing into the epidermal field at P0 and P30, normalized to percent of WT: 5 animals of each genotype analyzed per time point. Scale bar represents 25 μm.

(D) Representative whole mount immunostaining of E14.5 forepaws for the peptidergic nociceptor marker substance P; n=4 paws from 4 mice stained per genotype. Scale bar represents 50 μm.

(E) *In vitro* neurite growth of E14.5 TrkA+ nociceptors grown in NGF and measured in compartmentalized chambers. Data shown are from 2-6 independent experiments for each condition.

(F-I) Tuj1 immunostaining (F-H) of and quantification (I) of E14.5 explant outgrowth in response to 45 ng/mL NGF for 24 hours. Scale bar represents 500μm. Explants from $\geq$3 mice per genotype.

1-way (G) or 2-way (C,E) ANOVA, Bonferroni post-test. Data represent mean ± SEM, ns: not significant, *p<0.05, **p<0.01, ***p<0.001.

Figure 3: *Tnfr1*$^{-/-}$ and *Tnf* $^{-/-}$ peptidergic central projections are robust and misguided.

(A-F) TrkA and CGRP immunostaining in P0 WT (A-B), *Tnfr1*$^{-/-}$ (C-D), and *Tnf* $^{-/-}$ (E-F) lumbar spinal cord. Quantification of area (G) and lateral projections (H) within WT, *Tnfr1*$^{-/-}$, and *Tnf* $^{-/-}$, spinal cord sections. Scale bar represents 100 μm.

(I-X) Immunostaining and quantification of P7 (I-P) and P30 (Q-X) lumbar spinal cord.

2-way ANOVA, Bonferroni post-test (E,K,Q) and Fisher's exact test (F,L,R). 5 mice analyzed per genotype per time point.

Data represent mean±SEM, ns: not significant, *p<0.05, **p<0.01, ***p<0.001.

Figure 4: Deletion of *Tnfr1* or *Tnf* leads to the premature differentiation and impaired growth of non-peptidergic nociceptors

(A) Quantification of the number of TrkA+ sensory neurons in the L4/L5 DRG at P0, P14, and P30.
(B-D) Representative images of Ret/TrkA colocalization in the P0 DRG from WT, *Tnfr1*$^{-/-}$, and *Tnf* $^{-/-}$ mice. Scale bar represents 30 μm. Quantification of colocalization shown on overlay.
(E) Quantification of the number of IB4+ neurons in the L4/L5 DRG at P14 and P30.
(F-M) Immunostaining and quantification of IB4+ axons invading the spinal cord dorsal horn at P14 (F-H) and P30 (I-K) in WT, *Tnfr1*$^{-/-}$, and *Tnf* $^{-/-}$ mice. Quantification of IB4+ axon area shown in (L-M). Scale bar represents 100 μm.
(N-S) E14.5 DRG explants cultured in 100 ng/mL of NRTN, 100 ng/mL NRTN + 2 ng/mL TNF, or 100 ng/mL NRTN + 5 μg/mL sTNFR1 for 24 hours. Explants from ≥3 mice per condition. Scale bar represents 100 μm.
1-way ANOVA, Bonferroni post-test (A,L,M) or Tukey post-test (S). 2-way ANOVA, Bonferroni post-test (E). Number of mice analyzed is indicated in A,E. 5 mice analyzed in L-M.
Data represent mean±SEM, ns: not significant, *p<0.05, **p<0.01, ***p<0.001.

Figure 5: TNFα/TNFR1 signaling differentially regulates the excitability of peptidergic and non-peptidergic nociceptors
(A) Fluo-4 *in vitro* calcium imaging of E14.5 nociceptors. The changes in fluorescence of E14.5 TrkA+ nociceptors were measured (cultured in 45 ng/mL NGF for 3 days *in vitro*) after acute addition of the indicated TRP channel agonist. 2 experiments per condition, at least 3 mice per experiment are reported.
(B) Rescue experiment demonstrating that TNFα is sufficient to quench the hyperexcitability of *Tnf* $^{-/-}$ nociceptors. E14.5 nociceptors from WT or *Tnf* $^{-/-}$ mice were cultured in 1 ng/mL NGF (with or without TNF for *Tnf* $^{-/-}$ neurons) for 2 days *in vitro* and prepared for calcium imaging as in (A). 2 experiments per condition are reported; at least 3 mice per experiment were used.
(C) Representative image of P14 calcium imaging strategy examining non-peptidergic nociceptor excitability. IB4+ and IB4- neurons are shown before and after agonist addition. Red arrow: IB4+ neuron; white arrow: IB4- neuron. Scale bar represents 20 μm.
(D) Quantification of fluorescence changes of P14 nociceptors (cultured in 45 ng/mL for 1 day *in vitro*) in response to 1000 μM ATP.
(E) Excitability of P14 IB4+ and IB4- nociceptors responding to capsaicin. 2-3 experiments per condition, 3 mice per experiment.
Statistics determined by 1-way (A-B, D-E) ANOVA, Bonferroni post-test. Data represent mean±SEM, ns: not significant, *p<0.05, **p<0.01, ***p<0.001.

Figure 6: *Tnfr1*$^{-/-}$ and *Tnf* $^{-/-}$ mice are hypersensitive to thermal and mechanical stimuli
(A-E) Behavioral sensitivity of WT, *Tnfr1*$^{-/-}$, and *Tnf* $^{-/-}$ mice in response to the tail flick (A), Hargreaves (B), acetone drop (C), hot plate (D), and von Frey (E) tests measuring reflexive (A-B) or centrally-mediated (C-D) thermal pain thresholds or mechanical acuity (E).
n=6 mice per data point (aged P26-P56), if n>6 mice, it is indicated. 2-way (A,D,E) or 1-way (B,C) ANOVA, Bonferroni post-test. All mice shown are on a B6;129s mixed background. WT mice are background matched, non-littermate controls for *Tnfr1*$^{-/-}$ and *Tnf* $^{-/-}$ mice. Data represent mean±SEM, ns: not significant, *p<0.05, **p<0.01, ***p<0.001.

Figure 7: Loss of *Tnfr1* can compensate for heterozygous *Ngf* deletion
(A) Quantification of the number of TrkA+ and IB4+ neurons per L4/L5 DRG at P14. One DRG used per animal, number of DRGs is indicated.
(B-J) Analysis of the P14 L4/L5 spinal cord dorsal horn innervation density of CGRP (C-F) and IB4 (G-J) fibers and quantification (B). 5 animals analyzed per genotype, number of sections analyzed is indicated. Scale bar represents 50 μm.
(K-O) CGRP+ fiber density in P14 footpad (thick) glabrous skin. (L-O) Representative images of CGRP+ peptidergic nociceptor fibers invading the hindpaw footpad of P14 mice. Arrowheads point to invading fibers. Scale bar represents 25 μm. (K) Quantification of peptidergic innervation. 5 mice analyzed per genotype.
(P) Hot plate behavioral analysis at 50, 52.5, and 55°C. Behavioral analysis performed on mice from a mixed, B6;129 background. Mice analyzed are littermate controls except $Ngf^{+/-}$, which are background matched.
(Q-R) Western blot (Q) and quantification (R) showing the decay in P-Erk1/2 signal after E14.5 nociceptors from WT and $Tnfr1^{-/-}$ mice were deprived of NGF via incubation with anti-NGF for the indicated times. Nociceptors were cultured in 45 ng/mL NGF for 1 DIV. Data are from 3 independent experiments using cultured nociceptors from 4-6 mice per experiment per genotype. 2-way ANOVA, Holm-Sidak post-test.
Statistics determined by 1-way (O,P) or 2-way (A,I) ANOVA, Tukey post-test. Data represent mean ± SEM, ns: not significant, *p<0.05, **p<0.01, ***p<0.001.

Figure 8: Model of TNFα-TNFR1 antagonism against NGF-TrkA signals in nociceptors
(A) Model of TNFR1 and TrkA signaling events in WT animals. TNFR1 generates signals that suppress NGF-TrkA-dependent excitability, axon growth, survival, and differentiation. These signals lead to proper specialization of some TrkA+ peptidergic nociceptors as Ret+ non-peptidergic neurons, which are approximately equal in number to peptidergic cells in young adulthood (P30). Non-peptidergic nociceptors are dependent on TNFR1 signaling for maximal axon growth and excitability through TNFR1-TNFα reverse signaling.
(B) Loss of TNFα or TNFR1 signaling causes a gain-of-function of NGF-TrkA signals, hyperactivating TrkA excitability, axon growth, cell survival, and differentiation pathways (thick arrows). Consequently, more TrkA+ neurons are driven to toward a non-peptidergic fate earlier during development, which results in roughly 50% more IB4+ neurons by young adulthood (P30). In contrast, non-peptidergic nociceptors are deficient in excitability and NRTN-dependent axon growth in the absence of TNFα or TNFR1 (dashed arrows) through loss of a reverse signaling mechanism.

Figure S1, related to Figure 1: TNFα and TNFR1 localization and controls.
(A) RT-PCR for TNFR family members in E18.5 DRG, muscle, and brain. Note absence of TNFR2 (*Tnfrsf1b*).
(B) Verification of TNFR1 antibody in immunostaining. Scale bar represents 25 μm.
(C) TNFR1 is expressed on the somas and axons of DRG sensory neurons. Scale bar represents 40 μm.
(D) TNFR1 localized to somas and axons of neurons cultured in 45 ng/mL NGF. Scale bar represents 15 μm.
(E-F) $Tnf^{-/-}$ control examining TNFα localization in the skin at P0 and P30. Arrowheads point to invading fibers in the absence of TNFα. Scale bar represents 120 μm.

(G) *Tnf* $^{-/-}$ control examining TNFα localization in the spinal cord. Scale bar represents 150 μm.
(H) *In situ* hybridization showing expression of TNFα in the P4 DRG (black boxes/inset). Reproduced from Allen Brain Atlas (www.brain-map.org). Scale bar represents 500 μm
(I) *In situ* hybridization demonstrating absence of TNFR2 in the P4 SC. Reproduced from Allen Brain Atlas (www.brain-map.org). Scale bar represents 500 μm.

Figure S2, related to Figure 1: Quantification of TNFR1 colocalization with sensory neuron markers
(A-B) Quantification of TNFR1 colocalization with nociceptive neuron markers at P0 (A) and P30 (B). Number of cells and percent colocalization are indicated.
(C) Representative image demonstrating TNFR1 colocalization with large-diameter proprioceptive neurons at P0, suggesting TNFR1 is ubiquitous in sensory neurons in the DRG. These data were not formally quantified. Scale bar represents 20 μm.

Figure S3, related to Figure 3: Peptidergic and non-peptidergic nociceptive axons properly segregate into discrete laminae in the spinal cord in *Tnf* $^{-/-}$ and *Tnfr1* $^{-/-}$ mice
(A-C) Immunostaining of the P30 SC from WT (A) *Tnf* $^{-/-}$ (B), and *Tnfr1* $^{-/-}$ (C) mice. CGRP and IB4 axons properly segregate into laminae I-IIo and IIi, respectively, independent of TNFα-TNFR1 signaling. Representative images of WT, *Tnf* $^{-/-}$, and *Tnfr1* $^{-/-}$ P30 spinal cords from n=5 mice. Scale bar represents 100 μm.

Figure S4, related to Figure 5: Calcium imaging quantification shown as a function of working distance in the z-plane
(A) Calcium imaging data for E14.5 nociceptors cultured in 1 ng/mL NGF for 2 DIV. Black columns restate WT data from Figure 5B. They are compared against data from the same experimental conditions but analyzed using a shorter working distance to increase fluorescence intensity. A "scale factor" is calculated for each experimental condition and averaged to generate an approximate scale factor (B) to convert between the short (high fluorescence) versus long (low fluorescence) working distances.
(B) Average scale factor generated, which can be used to convert fluorescence fold changes yielded from short and long working distances of the objective.
(C) Proof of principle demonstrating that fluorescence fold change from an independent calcium imaging experiment can be reliably predicted using the generated scale factor from (B). "Original" *Tnfr1* $^{-/-}$ imaging data is copied from Figure 5D. "Predicted" fluorescent values represent the original data scaled by the average scale factor shown in (B). "Actual" fluorescent values indicate the quantitated data acquired from a short working distance.
(D) Demonstration that differences between groups are preserved despite acquisition from a short working distance. "Original" calcium imaging data of P14 nociceptors are presented with the same data acquired from a short working distance.
Data shown are from at least 2 experiments with cells taken from at least 3 mice. Data represent mean±SEM.

Figure S5, related to Figure 6: *Tnfr1* $^{-/-}$ and *Tnf* $^{-/-}$ littermate controls recapitulate non-littermate control behavioral data

(A-E) Behavioral sensitivity of WT, *Tnfr1*$^{-/-}$, and *Tnf* $^{-/-}$ mice in response to the tail flick (A), Hargreaves (B), hot plate (C), acetone drop (D) and von Frey (E) tests.
2-way (A,C,E) or 1-way (B,D) ANOVA, Bonferroni post-test. All mice shown are on a mixed B6;129 background. All mice are background matched, littermate controls aged between P42-P49 during testing. Data represent mean±SEM, ns: not significant, *p<0.05, **p<0.01, ***p<0.001.

Figure S6, related to Figure 7: P-Erk1/2/Erk1/2 decay is the same for WT and *Tnfr1*$^{-/-}$ neurons

The decay of activated Erk1/2 (calculated as P-Erk1/2 as a proportion of the Erk1/2 pool) normalized relative to each genotype at t=0. Data represent mean±SEM. Statistics determined by 2-way ANOVA, Holm-Sidak post-test.

VI. References

1. Abraira VE, & Ginty DD (2013). The sensory neurons of touch. *Neuron* 79, 618–39.
2. Airaksinen MS, & Saarma M (2002). The GDNF family: Signalling, biological functions and therapeutic value. *Nat Rev Neurosci* 3, 383–94.
3. Aloe L, Mugnaini E, & Levi-Montalcini R (1975). Light and electron microscopic studies on the excessive growth of sympathetic ganglia in rats injected daily from birth with 6-OHDA and NGF. *Arch Ital Biol* 113, 326-53
4. Bandell M, Story GM, Hwang SW, Viswanath V, Eid SR, Petrus MJ, Earley TJ, Patapoutian A (2004). Noxious cold ion channel TRPA1 is activated by pungent compounds and bradykinin. *Neuron* 41, 849–57.
5. Barker V, Middleton G, Davey F, & Davies AM (2001). TNFα contributes to the death of NGF-dependent neurons during development. *Nat Neurosci* 4, 1194–8.
6. Basbaum AI, Bautista DM, Scherrer G, & Julius D (2009). Cellular and molecular mechanisms of pain. *Cell* 139, 267–84.
7. Bergmann I, Priestley JV, McMahon SB, Bröcker EB, Toyka KV, & Koltzenburg M (1997). Analysis of cutaneous sensory neurons in transgenic mice lacking the low affinity neurotrophin receptor p75. *Eur J Neurosci* 9, 18–28.
8. Bonanomi D, Chivatakarn O, Bai G, Abdesselem H, Lettieri K, Marquardt T, Pierchala BA, Pfaff SL (2012). Ret is a multifunctional coreceptor that integrates diffusible- and contact-axon guidance signals. *Cell* 148, 568–82.
9. Brennan C, Rivas-Plata K, & Landis SC (1999). The p75 neurotrophin receptor influences NT-3 responsiveness of sympathetic neurons in vivo. *Nat Neurosci* 2, 699–705.

10. Caterina MJ, Schumacher MA, Tominaga M, Rosen TA, Levine JD, & Julius D (1997). The capsaicin receptor: A heat-activated ion channel in the pain pathway. *Nature* 389, 816–24.
11. Chang L, Kamata H, Solinas G, Luo JL, Maeda S, Venuprasad K, Liu YC, Karin M (2006). The E3 ubiquitin ligase itch couples JNK activation to TNFalpha-induced cell death by inducing c-FLIP$_L$ turnover. *Cell* 124, 601–13.
12. Chao MV (2003). Neurotrophins and their receptors: A convergence point for many signaling pathways. *Nat Rev Neurosci* 4, 299-309.
13. Chen AI, De Nooij JC, & Jessell TM (2006). Graded activity of transcription factor Runx3 specifies the laminar termination pattern of sensory axons in the developing spinal cord. *Neuron* 49, 395–408.
14. Chen CL, Broom DC, Liu Y, De Nooij JC, Li Z, Cen C, Samad OA, Jessell TM, Woolf CJ, & Ma Q. (2006). Runx1 determines nociceptive sensory neuron phenotype and is required for thermal and neuropathic pain. *Neuron* 49, 365–77.
15. Chuang HH, Prescott ED, Kong H, Shields S, Jordt SE, Basbaum AI, Chao MV, & Julius D (2001). Bradykinin and nerve growth factor release the capsaicin receptor from PtdIns(4,5)P_2-mediated inhibition. *Nature* 411, 957–62.
16. Clapham DE (2003). TRP channels as cellular sensors. *Nature* 426, 517–24.
17. Costigan M, Scholz J, & Woolf CJ (2009). Neuropathic pain: A maladaptive response of the nervous system to damage. *Annu Rev Neurosci* 32, 1-32.
18. Craig ADB (2003). Pain mechanisms: Labeled lines versus convergence in central processing. *Annu Rev Neurosci* 1–30.

19. Crowley C, Spencer SD, Nishimura MC, Chen KS, Pitts-Meek S, Armanini MP, Ling LH, McMahon SB, Shelton DL, & Levinson AD (1994). Mice lacking nerve growth factor display perinatal loss of sensory and sympathetic neurons yet develop basal forebrain cholinergic neurons. *Cell* 76, 1001–1011.
20. Davies AM, Lee KF, & Jaenisch R (1993). p75-deficient trigeminal sensory neurons have an altered response to NGF but not to other neurotrophins. *Neuron* 11, 565–74.
21. Deppmann CD & Janes K (2012). Cytokine-cytokine crosstalk and cell-death decisions. In Systems Biology of Apoptosis. I.N. Lavrik, ed. (New York, NY: Springer Publishers), 163-80.
22. Deppmann CD, Mihalas S, Sharma N, Lonze BE, Niebur E, & Ginty DD (2008). A model for neuronal competition during development. *Science* 320, 369–73.
23. Dong X, Han S, Zylka MJ, Simon MI, & Anderson DJ (2001). A diverse family of GPCRs expressed in specific subsets of nociceptive sensory neurons. *Cell* 106, 619–32.
24. Gascon E, Gaillard S, Malapert P, Liu Y, Rodat-Despoix L, Samokhvalov IM, Delmas P, Helmbacher F, Maina F, & Moqrich A (2010). Hepatocyte growth factor-Met signaling is required for Runx1 extinction and peptidergic differentiation in primary nociceptive neurons. *J Neurosci* 30, 12414–23.
25. Gerevich Z, Borvendeg SJ, Schröder W, Franke H, Wirkner K, Nörenberg W, Fürst S, Gillen C, & Illes P (2004). Inhibition of N-type voltage-activated calcium channels in rat dorsal root ganglion neurons by P2Y receptors is a possible mechanism of ADP-induced analgesia. *J Neurosci* 24, 797–807.
26. Glebova NO, & Ginty DD (2004). Heterogeneous requirement of NGF for sympathetic target innervation *in vivo*. *J Neurosci* 24, 743–51.

27. Glebova NO, & Ginty DD (2005). Growth and survival signals controlling sympathetic nervous system development. *Annu Rev Neurosci* 28, 191–222.

28. Guo T, Mandai K, Condie BG, Wickramasinghe SR, Capecchi MR, & Ginty DD (2011). An evolving NGF-Hoxd1 signaling pathway mediates development of divergent neural circuits in vertebrates. *Nat Neurosci* 14: 31–6.

29. Hefti FF, Rosenthal A, Walicke PA, Wyatt S, Vergara G, Shelton DL, & Davies AM (2006). Novel class of pain drugs based on antagonism of NGF. *Trends Pharmacol Sci* 27, 85–91.

30. Hunt S, & Mantyh P (2001). The molecular dynamics of pain control. *Nat Rev Neurosci* 2, 83-91.

31. Indo Y, Tsuruta M, Hayashida Y, & Karim M (1996). Mutations in the TRKA/NGF receptor gene in patients with congenital insensitivity to pain with anhidrosis. *Nat Genet* 13, 485-8 (1996).

32. Ji RR, Samad TA, Jin SX, Schmoll R, & Woolf CJ (2002). p38 MAPK activation by NGF in primary sensory neurons after inflammation increases TRPV1 levels and maintains heat hyperalgesia. *Neuron* 36, 57–68.

33. Julius D, & Basbaum AI (2001). Molecular mechanisms of nociception. *Nature* 413 203–10.

34. Kisiswa L, Osório C, Erice C, Vizard T, Wyatt S, & Davies AM (2013). TNFα reverse signaling promotes sympathetic axon growth and target innervation. *Nat Neurosci* 16, 865-73.

35. Lallemend F, & Ernfors P (2012). Molecular interactions underlying the specification of sensory neurons. *Trends Neurosci* 35, 373–81.

36. Lane NE, Schnitzer TJ, Birbara CA, Mokhtarani M, Shelton DL, Smith MD, & Brown MT (2010). Tanezumab for the treatment of pain from osteoarthritis of the knee. *N Engl J Med* 363, 1521–31

37. Lee KF, Li E, Huber LJ, Landis SC, Sharpe AH, Chao MV, & Jaenisch R (1992). Targeted mutation of the gene encoding the low affinity NGF receptor p75 leads to deficits in the peripheral sensory nervous system. *Cell* 69, 737–49.

38. Lindfors PH, Võikar V, Rossi J, & Airaksinen MS (2006). Deficient nonpeptidergic epidermis innervation and reduced inflammatory pain in glial cell line-derived neurotrophic factor family receptor α2 knock-out mice. *J Neurosci* 26, 1953–60.

39. Liu Q, Tang Z, Surdenikova L, Kim S, Patel KN, Kim A, Ru F, Guan Y, Weng HJ, Geng Y, Undem BJ, Kollarik M, Chen ZF, Anderson DJ, & Dong X (2009). Sensory neuron-specific GPCR Mrgprs are itch receptors mediating chloroquine-induced pruritus. *Cell* 139, 1353–65.

40. Liu Y, & Ma Q (2011). Generation of somatic sensory neuron diversity and implications on sensory coding. *Curr Opin Neurobiol* 21, 52–60.

41. Locksley RM, Killeen N, & Lenardo MJ (2001). The TNF and TNF receptor superfamilies: Integrating mammalian biology. *Cell* 104, 487–501.

42. Luo W, Wickramasinghe SR, Savitt JM, Griffin JW, Dawson TM, & Ginty DD (2007). A hierarchical NGF signaling cascade controls Ret-dependent and Ret-independent events during development of nonpeptidergic DRG neurons. *Neuron* 54, 739–54.

43. Luther JA, & Birren SJ (2009). p75 and TrkA signaling regulates sympathetic neuronal firing patterns via differential modulation of voltage-gated currents. *J Neurosci* 29, 5411–24.

44. Mantyh PW, Koltzenburg M, Mendell LM, Tive L, & Shelton DL (2011). Antagonism of nerve growth factor-TrkA signaling and the relief of pain. *Anesthesiology* 115, 189–204.

45. Marmigère F, & Ernfors P (2007). Specification and connectivity of neuronal subtypes in the sensory lineage. *Nat Rev Neurosci* 8, 114–27.

46. Molliver DC, Wright DE, Leitner ML, Parsadanian AS, Doster K, Wen D, Yan Q, & Snider WD (1997). IB4-binding DRG neurons switch from NGF to GDNF dependence in early postnatal life. *Neuron* 19, 849–61.

47. Moran MM, McAlexander MA, Bíró T, & Szallasi A (2011). Transient receptor potential channels as therapeutic targets. *Nat Rev Drug Discov* 10, 601–20.

48. Neumann S, Doubell T, Leslie T, & Woolf C (1996). Inflammatory pain hypersensitivity mediated by phenotypic switch in myelinated primary sensory neurons. *Nature* 384, 360-4.

49. Nikolaev A, McLaughlin T, O'Leary DDM, & Tessier-Lavigne M (2009). APP binds DR6 to trigger axon pruning and neuron death via distinct caspases. *Nature* 457, 981–9.

50. Park JW, Vahidi B, Taylor AM, Rhee SW & Jeon NL (2006). Microfluidic culture platform for neuroscience research. *Nat Protoc* 1, 2128–36.

51. Patel TD, Jackman A, Rice FL, Kucera J, & Snider WD (2000). Development of sensory neurons in the absence of NGF/TrkA signaling in vivo. *Neuron* 25, 345–57.

52. Peier AM, Moqrich A, Hergarden AC, Reeve AJ, Anderson DA, Story GM, Earley TJ, Dragoni I, McIntyre P, Bevan S, & Patapoutian A (2002). A TRP channel that senses cold stimuli and menthol. *Cell* 108, 705–15.

53. Pezet S, & McMahon SB (2006). Neurotrophins: Mediators and modulators of pain. *Annu Rev Neurosci* 29, 507–38.

54. Preibisch S, Saalfeld S, & Tomancak P (2009). Globally optimal stitching of tiled 3D microscopic image acquisitions. *Bioinformatics* 25, 1463–5.

55. Sandkühler J (2009). Models and mechanisms of hyperalgesia and allodynia. *Physiol Rev* 89, 707–58.

56. Sharma N, Deppmann CD, Harrington AW, St Hillaire C, Chen ZY, Lee FS, & Ginty DD (2010). Long-distance control of synapse assembly by target-derived NGF. *Neuron* 67, 422–34.

57. Silos-Santiago I, Molliver DC, Ozaki S, Smeyne RJ, Fagan AM, Barbacid M, & Snider WD (1995). Non-TrkA-expressing small DRG neurons are lost in TrkA deficient mice. *J Neurosci* 15, 5929–42.

58. Singh KK, Park KJ, Hong EJ, Kramer BM, Greenberg ME, Kaplan DR, & Miller FD (2008). Developmental axon pruning mediated by BDNF-p75NTR-dependent axon degeneration. *Nat Neurosci* 11, 649–58.

59. Smelter E, & Hochberg ME (2013). New treatments for osteoarthritis. *Curr Opin Rheumatol* 3, 310-6.

60. Snider WD, & McMahon SB (1998). Tackling pain at the source: New ideas about nociceptors. *Neuron* 20, 629–32.

61. Stucky CL, & Lewin GR (1999). Isolectin B_4-positive and -negative nociceptors are functionally distinct. *J Neurosci* 19, 6497–505.

62. Sun M, & Fink PJ (2007). A new class of reverse signaling costimulators belongs to the TNF family. *J Immunol* 179, 4307–12.

63. Verhoeven K, Timmerman V, Mauko, B, Pieber TR, De Jonghe P, & Auer-Grumbach M (2006). Recent advances in hereditary sensory and autonomic neuropathies. *Curr Opin Neurol* 19, 474-80.

64. Vrontou S, Wong AM, Rau KK, Koerber HR, & Anderson DJ (2013). Genetic identification of C fibres that detect massage-like stroking of hairy skin in vivo. *Nature*, 493, 669–73.

65. Wang T, Jing X, DeBerry JJ, Schwartz ES, Molliver DC, Albers KM, & Davis BM (2013). Neurturin overexpression in skin enhances expression of TRPM8 in cutaneous sensory neurons and leads to behavioral sensitivity to cool and menthol. *J Neurosci* 33, 2060–70.

66. Wehrman T, He X, Raab B, Dukipatti A, Blau H, & Garcia KC (2007). Structural and mechanistic insights into nerve growth factor interactions with the TrkA and p75 receptors. *Neuron* 53, 25–38.

67. Wende H, Lechner SG, Cheret C, Bourane S, Kolanczyk ME, Pattyn A, Reuter K, Munier FL, Carroll P, Lewin GR, & Birchmeier C (2012). The transcription factor c-Maf controls touch receptor development and function. *Science* 335, 1373–6.

68. Woolf CJ, & Salter MW (2000). Neuronal Plasticity: Increasing the Gain in Pain. *Science* 288, 1765–1768.

69. Yeo TT, Chua-Couzens J, Butcher LL, Bredesen DE, Cooper JD, Valletta JS, Mobley WC, & Longo FM (1997). Absence of p75NTR causes increased basal forebrain cholinergic neuron size, choline acetyltransferase activity, and target innervation. *J Neurosci* 17, 7594–605.

70. Zhang X, Huang J, & McNaughton PA (2005). NGF rapidly increases membrane expression of TRPV1 heat-gated ion channels. *EMBO J* 24, 4211–23.

71. Zylka MJ, Rice, FL, & Anderson DJ (2005). Topographically distinct epidermal nociceptive circuits revealed by axonal tracers targeted to Mrgprd. *Neuron* 45, 17–25.

VII. Methods

Animals

All experiments were carried out in compliance with the Association for Assessment of Laboratory Animal Care policies and approved by the University of Virginia Animal Care and Use Committee.

Tnfr1a$^{-/-}$ *and Tnf* $^{-/-}$ mice were purchased from Jackson Labs and backcrossed to a B6;129 mixed background for ≥4 generations. *Ngf*$^{+/-}$ mice were a gift from David Ginty and were maintained on a B6;129s mixed background. For timed pregnancies, animals were mated overnight and removed the next day once per week; E14.5 was judged as the time point 2 weeks post separation from mating. Animals were housed on a 12-hour light/dark cycle with food and water *ad libitum*. Tissue was collected from independently housed, non littermate B6;129 WT , *Tnfr1a*$^{-/-}$*, and Tnf* $^{-/-}$ mice generated from homozygous backcrosses for ≥4 generations. For *Ngf*$^{+/-}$ rescue experiments, tissue was taken from littermates generated from *Tnfr1a*$^{-/-}$ x *Ngf*$^{+/-}$ crosses and backcrosses of the F1 progeny. All behavioral experiments and tissue collection for *Ngf*$^{+/-}$ rescue experiments were performed with littermate controls except *Ngf*$^{+/-}$ mice, which were background matched on the B6;129 mixed background.

Tissue Processing

P0-P7 mice were euthanized by decapitation; hind-paws, spinal cords (L3-L6) and DRGs (L4/L5) or spinal columns (L3-L6) were dissected out and fixed in 4% PFA pH=7.4 o/n at 4°C. Tissues were cryoprotected in 30% sucrose for at least 2 days at 4°C, embedded in OCT, and then cryosectioned.

P14 mice were anesthetized by CO_2 gas followed by cervical dislocation and spinal columns were dissected and processed as above. Footpad skin was freshly dissected from the hindpaw and fixed in Zamboni's fixative (2% PFA, 15% picric acid in phosphate buffer pH=7.3) o/n at 4°C. Tissues were cryoprotected in 30% sucrose for at least 2 days at 4°C.

P30 mice were intracardially perfused with ice cold saline for 3 minutes followed by ice cold 4% PFA for 3-5 minutes. Spinal columns were dissected and processed as above. Paw skin was dissected and processed as above.

E14.5 forepaws were dissected and fixed in 4% PFA o/n at 4°C and changed to 30% sucrose for at least 2 days.

L4 or L5 DRGs were cryosectioned into thirds at 20µm but 1 DRG was sectioned in the same manner at 12µm. Every section was collected for each DRG and evenly distributed amongst 3 slides. Skin and spinal cords were sectioned at 30µm and every second or third section was collected. Skin was sectioned in the thick glabrous footpad (Figure 7) or the thin glabrous skin (Figure 2) proximal to the footpad, and is indicated in the legend. Spinal cords were sectioned starting with L3 for Figure 1, Figure S1, Figure 3, or Figure S3, or L4 for Figure 7.

Immunostaining

Staining was performed as described previously, with slight modifications (Suo et al. 2014). Staining was performed on slides in all cases for sectioned tissue. Sections were washed 2-4x for 5 minutes with PBS containing 0.1% Triton X-100 in PBS (PBS-T). Antigen retrieval/permeabilization was performed with 1% SDS buffer for 5 minutes, followed by wash 3-4x for 5 minutes with 0.1% PBS-T, incubation in blocking solution (5% normal serum, either goat or donkey, in 0.1% PBS-T) for 30 minutes, and incubation with primary

antibodies diluted in blocking solution. Primary antibody incubation was performed at 2 hours at room temperature (in most cases) or o/n at 4°C. Primary antibodies used in this study were: rabbit anti-peripherin (Millipore, 1:200), chicken anti-peripherin (Millipore, 1:1000), rabbit anti-TrkA (Millipore, 1:200), goat anti-Ret (Neuromics, 1:50), rabbit anti-parvalbumin (Swant, 1:5000), rabbit anti-TNFR1 (Enzo, 1:1000), goat anti-CGRP (AbD Serotec, 1:400), guinea pig anti-CGRP (Bachem, 1:4000 skin, 1:200-500 DRG/spinal cord), guinea pig anti-Substance P (Abcam, 1:200), rabbit anti-TNFα (Abcam, 1:100), mouse anti-ßIII Tubulin (Covance, 1:1000), rabbit anti-PGP9.5 (Millipore, 1:500), and Alexa-568-conjugated IB4 (Invitrogen, 1:100). IB4-568 was used as a primary antibody. Following primary antibody incubation, sections were washed 3x for 5 minutes with 0.1% PBS-T, then secondary antibodies diluted in blocking solution were added. Alexa-488; -555/-546/-568; -647/-660 secondary antibodies were used against different species (Invitrogen, 1:500). Alexa-488 F(ab')2 anti-rabbit fragment was also used (Invitrogen, 1:500) for TrkA or parvalbumin double staining with TNFR1. After secondary incubation, sections were washed 3-4x for 5 minutes in 0.1% PBS-T, and mounted in Fluoromount-G with DAPI (SouthernBiotech).

Whole mount staining of forepaws was performed as described previously (Glebova & Ginty 2004), with slight modifications. Paws were washed 3x for 15 minutes with ice cold 1X PBS at 4°C. Paws were incubated in blocking solution (5% normal serum/1% PBS-T) o/n at 4°C. Paws were then incubated in primary antibodies diluted in blocking solution 2x o/n at 4C. Paws were washed with 1% PBS-T 3x for 2 hours at room temperature, then incubated with secondary antibodies diluted in blocking solution o/n at 4°C. Paws were washed 3x 2 hours

at room temperature and serially dehydrated in MeOH in PBS (50%, 80%, 100%). Paws were then cleared in a mixture of 2:1 BABB and imaged.

Immunocytochemistry

Cultured cells were fixed for 1 hour with 4% PFA and then processed for immunofluorescence as described above.

Microscopy

All tissue was imaged on a Leica SP5X inverted laser scanning confocal microscope with a white light laser and 405 diode. Explant, whole mount paw, and *in vitro* calcium imaging data were acquired with a 10X objective. Spinal cord data were acquired at 20X or 40X with oil immersion. Skin data were acquired at 40X with oil immersion or 63X with oil immersion. DRG data were acquired at 20X or 63X with oil immersion.

Cell culture

DRGs from either E14.5 or P14 animals were dissected into DMEM/F-12 supplemented with 10% FBS and penicillin/streptomycin (1 U/mL) on ice. P14 DRGs were processed as described previously (Guo et al. 2011) while E14.5 DRGs were processed in the same enzymes at 10% of the concentration for 15-30 minutes per enzymatic digestion. DRGs were then triturated with 23 and/or 27 gauge needles and plated into mass or compartmentalized cell cultures on poly-D-lysine (50 μg/mL) and laminin (1μg/mL) coated coverslips. Varying concentrations of NGF purified from mouse salivary glands and 5μM cytosine ß-D arabinofuranoside hydrochloride (AraC) (Sigma) were added to all dissociated cultures

(except those used for biochemistry). E14.5 TrkA+ neurons were selected for as described previously (Deckwerth and Johnson 1993). Cells were maintained at 37°C (10% CO_2) in a humidified cell culture incubator.

Western Blotting

Approximately 100 DRGs were harvested from n=4-6 E14.5 pups per genotype, dissociated, and plated into a 96-well plate. Cells were incubated with 45 ng/mL NGF for 24 hours, washed 3 times with 1X PBS, incubated with an anti-NGF monoclonal antibody (1:1000, Millipore) diluted in serum-free media for the indicated times, and lysed with 50 µL of boiling 2X Laemmli buffer (Boston BioProducts). Lysates were boiled for 5 minutes, vortexed, boiled for an additional 5 minutes, and then subjected to SDS-PAGE, as described previously (Suo et al. 2014). The PVDF membrane was blocked for 30 minutes in Odyssey Blocking Buffer (Li-Cor), followed by incubation with primary antibody diluted in 0.1% TBS-Tween overnight at 4C. The next day, the membrane was washed 3 times with 0.1% TBS-Tween and incubated with secondary antibody diluted in 0.1% TBS-Tween for 1 hour at room temperature. The membrane was then washed 3 times with 0.1% TBS-Tween and imaged on an Odyssey Infrared Imaging System (Li-Cor). For reprobing, the membrane was incubated for 20 minutes with pre-heated (to 50˚C) harsh stripping buffer (2% SDS, 62.5 mM Tris-HCl pH=6.8, 0.01% ß-mercaptoethanol), carried out at room temperature with vigorous agitation. The membrane was then thoroughly washed with NanoPure water (>1 hour, >30 washes) followed by blocking, primary antibody incubation, secondary antibody incubation, and visualization. The primary antibodies used in this study are: mouse anti-P-Erk1/2 (Cell Signaling, 1:1000), rabbit anti-Erk1/2 (Cell Signaling, 1:1000), and mouse

anti-Tuj1 (Covance, 1:1000). The secondary antibodies used in this study are: IRDye 800CW Goat anti-Rabbit IgG (Li-Cor Sciences, 1:10000), and IRDye 800CW Goat anti-Mouse IgG (Li-Cor Sciences, 1:10000).

Microfluidic devices

Microfluidic devices were generated as described previously (Park et al. 2006). These chambers were affixed to cover glass coated with poly-D-lysine (50 μg/mL) and laminin (1μg/mL).

In vitro calcium imaging

Mass cultures of E14.5 or P14 DRG neurons were generated and supplemented with 45 ng/mL NGF and AraC. Calcium imaging was performed by washing cells 2-3x with Calcium Imaging Buffer (CIB) (125mM NaCl, 2mM $MgCl_2$, 4.5mM KCl, 10mM glucose, 20mM HEPES pH=7.4, 2mM $CaCl_2$), then loaded with 3μM Fluo-4 AM (Invitrogen) diluted in CIB for 20-30 minutes. Cells were then washed 2-3x with CIB and permitted to sit for 20-40 minutes for deesterification. After deesterification, cover slips were loaded into customized imaging chambers and imaged on the Leica SP5x microscope. 1μM capsaicin (MP Biomedicals), 100μM L-menthol (MP Biomedicals), or 100μM mustard oil (Acros Organics) was acutely added to the cultures. Imaging sessions lasted at most 2 minutes. Cultures and solutions were maintained at 37°C during incubations and imaging. One chemical treatment was used per experiment.

P14 cultures were processed identically except they were used for calcium imaging after 12-24 hours after plating into NGF. Also, they were incubated with Fluo-4 and IB4 for 1 hour before deesterification as described previously (Gerevich et al. 2004). ATP (Thermo Scientific) was acutely added at a concentration of 1000μM.

Explants

≤50 μL of Matrigel Basement Membrane (BD Biosciences) was added to coverslips coated with PDK/laminin and permitted to solidify for 20-30 minutes at 37°C according to the manufacturer's instructions. E14.5 DRGs were freshly dissected and attached to the surface of the gel to assess 2D growth. Either 45 ng/mL of NGF or 100 ng/mL of neurturin (Pepro Tech, 450-11) was added to the cultures for 24 hours. For TNF reverse signaling explant experiments, either 2 ng/mL of TNF (R&D Systems, 210-TA-010) or 5 μg/mL of sTNFR1 (R&D Systems, 636-R1-025) in addition to 100 ng/mL NRTN was added to explants. Cultures were then fixed with 4% PFA for 1 hour, washed 3x with 1X PBS, and incubated in blocking solution (5% normal serum in 0.3% PBS-T) at 4°C o/n. Primary antibodies diluted in blocking solution were added to the cultures the next day and incubated at 4°C o/n. Explants were washed 3x with 1X PBS before secondary antibodies diluted in blocking solution were added at 4°C o/n. Cultures were washed then imaged. Post-acquisition stitching was performed with a FIJI macro (Preibisch et al. 2009).

Alternatively, some explant cultures were fixed, washed 3x with 1X PBS, and loaded with 1 mg/mL (at 1:1000 in 1X PBS) Calcein-AM fluorescent dye (Life Technologies) for 1 hour, followed by 30 minutes of deesterification, as described previously (Kisiswa et al. 2013).

RT-PCR

For TNFRSF expression analysis, E18.5 DRGs, muscle, and brain were extracted from mice and homogenized in Trizol (Invitrogen). RNA was then processed as described previously (Deppmann et al. 2008), according to the manufacturer's instructions. Primers used for the analyses are:

TNFRSF1A F	ACCAAGTGCCACAAAGGAAC
TNFRSF1A R	CTGGAAATGCGTCTCACTCA
TNFRSF1B F	AAATGCAAGCACAGATGCAG
TNFRSF1B R	CAGCAGACCCAGAGTTGTCA
TNFRSF3 F	GAGCCCTAAACATGGCAGAG
TNFRSF3 R	CTGCCCTTCTCACTGTCCTC
TNFRSF4 F	CTTGTACCTGCTCCGAAAGG
TNFRSF4 R	AGGATATGGGCTGTCTGTGC
TNFRSF5 R	TCTGAGCCCTGGAACTGTTT
TNFRSF5 F	TATTACTGCGGACCCCTGAC
TNFRSF6 F	ACCTGGTGACCCTGAATCTG
TNFRSF6 R	TGATACCAGCACTGGAGCAG
TNFRSF7 F	TGTGCAGCTCCGACTGTATC
TNFRSF7 R	GGCAGCTGTAAGGACAAAGC
TNFRSF8 F	TGCAGAGAAGTGGGTCAGTG

TNFRSF8 R	GTGGCTCTGGAGGTTCTCTG
TNFRSF9 F	CTGGTTCTCTGTGCCCAAAT
TNFRSF9 R	AGTGCTTCTCGGTTTCCTGA
TNFRSF10B F	AAACCAGGCAGCTTTGAAGA
TNFRSF10B R	AGCTGGGTTGTTTCCATTTG
TNFRSF11A F	GCCAGCAAGAAGTGTGTGAA
TNFRSF11A R	CCGGTCCGTGTACTCATCTT
TNFRSF11B F	TGGGAATGAAGATCCTCCAG
TNFRSF11B R	GAGGAAGGAAAGGGCCTATG
TNFRSF12A F	CACTGATCCAGTGAGGAGCA
TNFRSF12A R	CTCTCTGTCTGCCCCAGAAC
TNFRSF13B F	GGCCGGATAACTTAGGAAGG
TNFRSF13B R	TGGGAAGTGGCTCTCCTCTA
TNFRSF13C F	GTGGGTCTGGTGAGTCTGGT
TNFRSF13C R	TTGAATGGAGGCCAGTTAGG
TNFRSF14 F	CAGCTAGATCGGCCTACCAC
TNFRSF14 R	GCTGTTCCACAGCATGAGAA
TNFRSF16 F	TTGCTTGCTGTTGGAATGAG
TNFRSF16 R	AGCTCCTGGGGAGGAAAATA
TNFRSF17 F	ACTAAGAGCAGGGCTGGTGA
TNFRSF17 R	CTTGCCATAGTCACCCGTTT
TNFRSF18 F	CTGTGCCATGGGTACCTTCT

TNFRSF18 R	AAGCAGCCACACTAGGAGGA
TNFRSF19 R	TCAATCCCGAAAATGAAAGC
TNFRSF19 F	GTCCTTTGAGCATCCTGAGC
TNFRSF21 F	CTCGCGGTACCTTCTCTGAC
TNFRSF21 R	CGTGTGCTCAGGATGAGAAA
TNFRSF25 F	GTGCTGAGGACCTTCGTAGC
TNFRSF25 R	GCCCCTTCTGGTATTTCTCC
TNFRSF27 F	GGCCAACTGCACAAATACCT
TNFRSF27 R	TCCTACCAGTGCGACAAGTG
GAPDH-F	CCCATCACCATCTTCCAGGA
GAPDH-R	TTGTCATACCAGGAAATGAGC

Behavioral Assays

Mice were tested between P26 and P56 (Figure 6), between P26-P42 (Figure 7P), or between P42-P49 (Figure S5). Before testing, mice were habituated to handling. All behavioral experiments were performed during the light cycle. One trial per mouse is reported per data point. Behavioral experiments were performed with cohorts >30 mice for each genotype in Figure 6 (P26-P56 mice). *Ngf*$^{+/-}$ rescue hot plate behavioral experiments (Figure 7P) were performed with cohorts of 6-8 littermate mice per genotype. *Ngf*$^{+/-}$ mice in Figure 7P were not littermates but were background (B6;129 hybrid) and age-matched.

Tail flick: Mice were manually restrained while the posterior 1/3 of the mouse's tail was submerged in a water bath (Fisher, Isotemp) maintained at the designated temperature

±0.3°C until mouse flicked or reacted to the temperature. One trial per mouse was recorded per temperature with a 20-second window in which to respond. Mice were subjected to the test at most three times per day with trials spaced at least 20 minutes apart.

Hot plate: Mice were placed on plates maintained at the given temperature (Columbus Instruments, Hotplate analgesia meter) and restricted to move within the area of an inverted 1000 mL beaker. The latency to vigorously lick/groom was recorded. No more than 3 trials per mouse were conducted per day with trials spaced at least 20 minutes apart. The test was stopped at 60 seconds in Figure 6 and Figure S5, and 90 seconds in Figure 7P for *Ngf*$^{+/-}$ rescue experiments.

Hargreaves: Mouse was manually restrained and its hind-paw was placed over an infrared light source (Ugo Basile) until reflexive removal of paw. Intensity of the IR beam was calibrated such that WT withdrawal in Figure 6 occurred at roughly 10 seconds.

von Frey: Mice were placed on a thin mesh screen and restrained within slightly opaque red containers during the test duration. Mechanical filaments of varying diameter (Bioseb, Touch Test) were administered to hind-paws beneath the apparatus and the percent response of paw lifting per 5 trials per filament was recorded.

Acetone drop: 50µL of acetone was applied to the hind-paw and permitted to evaporate for 10 seconds. The duration of grooming per 120 seconds after the evaporation was recorded. Grooming was judged as forepaw/hindpaw/stomach licking, facial grooming, and hindpaw dragging.

Quantitation of Images

All analyses were performed with FIJI/ImageJ and Leica LAS AF software.

Skin: P0 skin for PGP9.5 innervation analysis was acquired at 40x resolution and z-stacks were acquired from randomly chosen fields judged by DAPI staining at 1.25-2 μm increments. One image was acquired per section for PGP9.5 analysis. Fibers projecting into the epidermis were scored as described previously (Zylka et al. 2005, Lindfors et al. 2006). Quantification was performed by counting axons penetrating the epidermis per cutaneous field (defined as z-stack depth times length of epidermis; z-stack depth was analogous between genotypes; optical sections without fibers were not included); at least 369 fibers were scored for this analysis.

For P0 peripherin analysis, images were acquired at 63x resolution chosen randomly by DAPI staining. Innervation density was quantified by counting the number of neurite branches in the skin as described previously (Newbern et al. 2011). At least 500 fibers were scored per genotype for this analysis.

P30 PGP9.5 epidermal innervation analysis was performed similarly at 63X magnification with randomly chosen fields selected by DAPI staining per section per 2 animals. At least 421 fibers were analyzed per genotype for this analysis.

For CGRP skin immunostaining at P14, image fields from each section were randomly chosen and acquired at 63X magnification.

Spinal cord: For all analyses, spinal cord sections were acquired at 20X resolution in z-stacks of 1.25-2 μm and quantified by tracing the area of individual laminae positive for a given marker. If sections showed lateral or medial bundle projections, they were traced and included in the area measurement. Individual axon projections were considered normal and

not traced (e.g. single ectopic fibers projecting ventrally). The area of only one dorsal horn was analyzed per spinal cord section.

Lateral projections: Axonal bundles were determined to be "mistargeted" if they projected medially and contacted fibers from the opposite hemisphere of the spinal cord. Axonal bundles projecting laterally were scored as "mistargeted" if they exhibited deep nociceptor central projections, as previously described (Guo et al. 2011). If a section exhibited either quality, it was scored as mistargeted.

DRG quantification: L4 or L5 DRGs were sectioned into thirds and each section was collected and distributed amongst three slides and stained with a given marker. Images were acquired at 20X resolution in z-stacks at 1-1.25 μm intervals for quantification. Cells with visible nucleoli and positive for a given marker were scored in ImageJ. The total number of cells was summed and multiplied by 3 to yield the total number of cells in a given DRG.

For Ret/TrkA immunostaining of differentiation at P0, the Ret channel was normalized to a constant intensity in FIJI and the number of arbitrarily selected TrkA+ neurons also positive for Ret were scored and divided by the number of TrkA+ cells selected to yield "percent differentiating."

For the TNFR1 colocalization analysis with different nociceptor markers in the DRG, cells were randomly selected in one channel and then scored for the presence of TNFR1 in another channel. The number of positive neurons for a given marker was divided by the total number of neurons positive for TNFR1 and the given marker. These values were computed to be the percentage of positive neurons for the different marker combinations.

Calcium imaging: For calcium imaging acquisition, regions of high cell density were arbitrarily selected and acquired based on bright field illumination or fluorescence in the IB4-568 channel. Quantification was performed in Leica LAS AF. A max intensity projection was generated in the 488 channel (Fluo-4) and neuronal somata were selected for analysis. If non-peptidergic IB4+ neurons were analyzed, their somata were arbitrarily selected in the IB4 channel. The average fluorescence of Fluo-4 before chemical addition was averaged and calculated, and the maximum intensity was recorded within 90 seconds after chemical addition (usually, the maximum value changed only slightly from the peak within the vicinity of chemical addition). Background normalization was performed by determining the fold change of background and scaling the relative fluorescence fold changes of an experiment accordingly. For instance, if background increased after agonist addition, fold change was scaled down and vice versa. Values were discarded if the total fold change was <5%.

Explants: After staining, average explant outgrowth was analyzed by tracing axons from their most distal point back to the perimeter of the ganglion. If the neurites of an explant clumped near the edge of the Matrigel area, that particular region of the explant was discounted and the remainder of the outgrowth was scored normally. If an explant grew three dimensionally (i.e. into the gel), it was not analyzed. If an explant appeared to not extend neurites whatsoever, it was discarded. The average length of all fibers is reported as average outgrowth.

Dissociated neuron axon growth: Axons were measured using ImageJ. The axon with the longest length was selected for measurement if multiple axons branched from the same origin. The length of individual axons was measured starting from its growth at the microfluidic channel to the distal tip. After 24 hours the same axon was identified and measured the same way. The growth of each axon was calculated by subtracting the initial length from that after 24 hours. Pixels were converted into microns, and all values within the same condition between experiments were averaged for final representation of axon growth.

Western blot densitometry: Individual bands were selected in each lane and their intensities measured with ImageJ. The signal was quantified by measuring the area under the curve for each lane's signal. Activated P-Erk/1/2 was calculated as the fraction of P-Erk1/2 signal relative to Erk1/2 signal.

Statistical Methods

All statistical tests were performed with Prism 6 software. Data were assumed to be normal although no formal normalization test was conducted. Data are all presented as mean±SEM in each figure. Statistical significance threshold was set at $\alpha<0.05$ for all analyses.

Supplemental References

72. Deckwerth TL, & Johnson EM (1993). Temporal analysis of events associated with programmed cell death (apoptosis) of sympathetic neurons deprived of nerve growth factor. *J Cell Biol* 123, 1207–22.

73. Preibisch S, Saalfeld S, & Tomancak P (2009). Globally optimal stitching of tiled 3D microscopic image acquisitions. *Bioinformatics* 25, 1463–5.

74. Park JW, Vahidi B, et al. (2006). Microfluidic culture platform for neuroscience research. *Nat Protoc* 1, 2128–36.

Chapter 3 – Development of magnetogenetic actuators to remotely control cellular activity

The human brain is remarkably complex. It possesses over 100 billion neurons that make 100 trillion synapses[41]. In other words, a single neuron makes 1,000 connections with other cells. As of 2011, comparisons between the brain and the zenith of computing technology of the time provide estimates that a single brain (~3 pounds, ~1200 cm^3) possesses roughly one-tenth of the power of the fastest manmade supercomputer in the world, "K computer" in Kobe, Japan (22,000 m^2 housed in several skyscrapers), which is remarkable (http://www.scientificamerican.com/article/computers-vs-brains/). Despite the fact that a mere 10 brains retain the complexity of a powerful supercomputer, the brain can achieve these feats despite using 1/1,000,000 of the power required by the supercomputer. In addition to these neuron-specific characteristics, the nervous system at large interacts with scores of diverse cell types in the periphery and several more in the brain such as astrocytes, oligodendrocytes, and microglia. Given the remarkable complexity of the human brain, such as its circuits and the cells comprising them, how can we begin to deconstruct the circuits that underlie the most elusive human behaviors such as love, imagination, and consciousness?

One route of investigation pursued for about two decades is the development of biotechnology that can be utilized to activate genetically defined populations of neurons by expressing synthetic genes containing "sensor" and "actuator" domains that can convert normally inert physical stimuli into intelligible biological signals. One brilliant point of inflection that paved the way for the modern causal investigation of neural circuit function came from Gero Miesenbock's group in 2002 at Oxford[42]. Using elegant logic, they

suspected they could engineer neurons to become light-sensitive by reconstituting selective components of the phototransduction cascade used by photoreceptors. They determined the necessary number of components required to elicit light-induced currents, which consisted of a G-protein alpha subunit (effector), an arrestin (inverse effector), and an opsin (sensor). They demonstrated that they can express this artificial system in hippocampal neurons to evoke light-dependent action potentials.

To put this study in context, it is a significant expansion of the previous mode of neuronal stimulation that had been used since the 1950s, namely coarse electrical stimulation of relatively broad brain nuclei[43]. While these studies elucidated basic properties of the brain and were performed by luminaries of the past such as Wilder Penfield and Theodore Rasmussen, and those a bit more contemporary such as Bill Newsome[44], a dynamic change in science was brewing. Given the meteoric rise of genetic power such as cell labeling with fluorescent proteins[45], the sequencing of the human genome[46], and the completed worm connectome[47], genetically non-specific stimulation of neural domains became antiquated—a relic of the past analogous to the Golgi stain. What we needed was more approaches similar to "chARGe," where genetically defined neuronal populations could be labeled with a modulatory system that had the capacity to directly influence neuronal activity.

To this end, a rapid flurry of groundbreaking work was unleashed, beginning with "chARGe," where light-sensitive genetic components can be targeted to neurons to control activity. One such approach, termed "SPARK," utilized a chemical engineering approach to confer photosensitivity to ion channels using an inducible photoisomerizable compound

that can reversibly control neural activity. Clever though it was, SPARK was ultimately supplanted by perhaps the most revolutionary class of technology since GFP: optogenetics.

In September of 2005, a revolution occurred in neuroscience. A small group from Stanford, housed in the lab of Assistant Professor Karl Deisseroth, pioneered a technological innovation that would change the face of brain science for more than a decade. Without exaggeration, this technology has become a staple of neuroscience in the way that PCR has revolutionized molecular biology, GFP has revolutionized the study of cell biology, and antibody generation has revolutionized the field of immunology. The authors were able to repurpose a light-sensitive cation channel from bacteria to express in neurons. They found that this protein, channelrhodopsin-2 (ChR2), could rapidly and reversibly activate neurons in response to pulses of blue light, enabling remote control of genetically defined neurons with simplicity. The lead author of the study, Ed Boyden, perhaps put it best: "Serendipity had struck—the molecule was good enough in its wild-type form to be used in neurons right away."[48,49]

In the decade that has passed since the inception of what is now called "optogenetics," the technology has only gotten stronger. While the original ingenuity of the authors in Deisseroth's lab at Stanford as well as their own labs (Ed Boyden at MIT, Feng Zhang at MIT) has been replaced by clever modes of activating circuits in less invasive and more rigorous ways, the ability to control neural circuits is now simple, the ultimate compliment for a working technology. In the decade since, the modes of optogenetic control over activity have only diversified. In addition to the initial excitatory variant, ChR2, there are now several modes of inhibition[50,51], biochemical activation[52], step-function activation opsins[53], and photosensitive NMDA receptors[54].

In addition to optogenetic actuators, another class of actuators has been invented recently (i.e. in the past two decades), which has been termed "chemogenetics"[55]. Whereas optogenetic actuators are largely descended from bacterially-derived opsins and engineered proteins, chemogenetic actuators share little resemblance to one another, mainly because of the diverse needs that they satisfy. For instance, perhaps the most widely utilized are the DREADDs (designer receptors exclusively activated by designer drugs), a class of synthetic G-protein coupled receptors (GPCRs) engineered in the laboratory of Bryan Roth at UNC – Chapel Hill[56]. However, several other synthetic chemogenetic tools have been invented such as the PSAM/PSEM system generated by Scott Sternson's lab in Janelia Farm/HHMI[57]. While these groups employed chemical engineering to generate synthetic chemogenetic receptors, others have approached this same task using a genetic strategy. Groups led by Mike Ehlers at Duke and Richard Palmiter at the University of Washington, both also of HHMI, devised a clever strategy to selectively activate defined neurons using the capsaicin receptor, TRPV1[58,59]. By generating a Cre-dependent TRPV1 expression construct, the groups could target the capsaicin receptor to specific neurons, which could then be activated using the specific TRPV1 agonist, capsaicin. When used on a TRPV1 null background strain of mice, this strategy has enabled description of functionally uncharacterized subpopulations of neurons that contribute to several behaviors such as itch[60].

These actuator systems, while revolutionary, and no doubt destined to receive the Nobel Prize, are severely handicapped by several intrinsic limitations. First, optogenetic tools have been known to require intensive surgery and long-term implants in order to deliver light into dense brain tissues[53]. Specifically, a laser and a stabilization mechanism

must be implanted in the brain in order to deliver light to the otherwise dense and opaque brain. Several recent technological advances have alleviated the burden of direct fiberoptic implantation into target tissues through the clever use of wirelessly activated LEDs[61] and optical stimulation of thin tissues such as the glabrous skin of the footpad[62], most of the work affiliated with Scott Delp's group at Stanford. These advances are useful but nevertheless avoid the intrinsic problem associated with optogenetics, which is that light does not scatter well in brain tissue. Chemogenetics maintains the opposite problem, which is overly broad activation of designated receptors with little to no control over receptor activation.

Approaches using infrared light that weakly penetrates the skull have been developed, but tissue heating and the intrinsic problem of poor light scatter remain. Recently, a technique has been developed that allows for both remote and more temporally precise control of neurons using high-frequency radiowaves, which has been successfully used by several groups[63–66]. This approach takes advantage of the fact that ion channels such as TRPV1 are temperature sensitive and by decorating TRPV1 channels with either organic or inorganic nanoparticles and applying high-energy radiowaves, magnetically induced hysteresis will enable heat dissipation from the iron storage nanoparticles and thermally activate TRPV1. However, while radiowaves penetrate the skull in a manner analogous to infrared radiation, they are high-energy waves that can cause tissue damage, prevent freely behaving animals to be manipulated, and ultimately exert their influence on multicomponent effectors. Moreover, the kinetics of these systems function more analogously to chemogenetic actuators whereby activity cannot be precisely controlled with absolute temporal specificity.

Thus, to activate neural networks and causally probe the function of circuits underlying behavior, next-generation actuator systems must be developed to artificially activate cells in a remote, reversible, and temporally precise manner. To alleviate the limitations when using optogenetic, chemogenetic, and radiogenetic actuators as outlined above, I am designing an altogether distinct class of actuator proteins sensitive to magnetic fields. This class of actuators functions through truly remote static magnetic field activation of synthetic magnetoreceptors that can be encoded in a single gene[67]. The promise of this approach is almost boundless: broad populations of cells can be targeted and activated in different spatial domains within the brain or other tissues with no equipment except for permanent magnets or electromagnets, which can be bought cheaply.

Chapter 4 – Activation of the nervous system using an engineered magnetoreceptor

I. Introduction

Opto- and chemogenetic actuators have revealed critical properties of neural networks in normal and pathological states[42,48,55,59,68,69]. While both opto- and chemogenetics remotely control neuronal stimulation, optical strategies are limited spatially by poor light penetration into dense tissues and chemogenetic strategies suffer from slow pharmacokinetics that prevent cellular activation on a physiologically relevant timescale. Therefore, there remains a need for next generation actuators that are non-invasive and can respond rapidly and reversibly[70]. Several recent studies have reported transient receptor potential vanilloid 1 (TRPV1) ion channels can be engineered to become sensitive to a combination of radiowaves and magnetothermal heating through coupling to the iron storage protein, ferritin, or to inorganic paramagnetic nanoparticles[63,64,71–73]. While these reagents represent an important advance, they are multicomponent systems (e.g. requiring delivery of nanoparticles and a genetically encoded channel) with possible off-target heating effects. One study has employed non-thermal magnetogenetic control of somatic tissues to regulate blood glucose[65], but a fully encoded, single component magnetogenetic system has yet to be applied to the nervous system. Here, we have expanded upon these strategies by engineering a magnetogenetic actuator through fusion of the non-selective cation channel, TRPV4[74–76], to the paramagnetic protein, ferritin[77]. We have successfully applied this actuator to the nervous system and validated it using *in vitro* calcium imaging, brain slice electrophysiology, *in vivo* electrophysiology, and acute modulation of behavior in freely moving zebrafish and mice.

II. Results

(a) Design and screen of a novel magnetically sensitive cation channel

To engineer a novel single-component magnetogenetic actuator, we based our design on TRPV4 since it has been reported to respond to pressure[74,75]. We suspected that, when fused to TRPV4, a paramagnetic protein would enable magnetic torque to tug open the channel to depolarize cells (Supplementary Fig. 1). While we hypothesized that magnetic field dependent activation of TRPV4 would be more facile than using a non-mechanically sensitive ion channel, it may also be formally possible that application of torque to ion channels in general would achieve the same result. Therefore, we developed a small library of 21 proteins consisting of TRPV4 fused to a gene encoding two subunits of the paramagnetic ferritin protein (Supplementary Table 1)[78]. Human embryonic kidney (HEK) 293 cells did not express 18 of the 21 generated chimeric proteins following transient transfection, presumably due to cytotoxicity of the chimeric channels. For the three channels that did express in HEK293 cells, we performed *in vitro* calcium imaging to determine whether the fusion proteins responded to magnetic fields. Using the fluorescent calcium-binding dye Fluo-4, we measured calcium transients in response to a ~50 mT magnetic field delivered by an electromagnet (Supplementary Fig. 2). Of the three candidate proteins, we observed detectable calcium transients in response to magnetic stimulation with one fusion protein, consisting of ferritin tethered to a truncated TRPV4 carboxyl-terminus (Δ760-871) (Supplementary Fig. 3). Because the 17±3.5% (mean±SEM) increase in magnetically evoked calcium transients was smaller than expected TRPV4 responses[76] (Supplementary Fig. 3h), we hypothesized that trafficking to the plasma membrane was disrupted[79], resulting in blunted calcium signaling. We next optimized the

chimeric channel's subcellular localization by adding a series of subcellular trafficking signals to Magneto akin to the optimization of optogenetic actuators[80,81]. Ultimately, we determined that the addition of a plasma membrane trafficking signal enhanced the prototype channel's membrane expression (Supplementary Fig. 4), and we dubbed this improved channel "Magneto2.0." We confirmed that HEK293 cells were viable after Magneto2.0 expression (Supplementary Fig. 5) and then measured magnetic field dependent calcium transients produced by Magneto2.0 using the paradigm described in Supplementary Fig. 3. We observed that cells expressing Magneto2.0 (58% transfected cells, n=6 coverslips, n=539 cells) exhibited robust calcium transients approximately 2.5-fold higher than baseline after 50 mT magnetic stimulation with no change in any of the control conditions (Fig. 1a-f). Controls included: (1) cells expressing non-fused TRPV4 and ferritin moieties, (2) unstimulated Magneto2.0 expressing cells, (3) Magneto2.0 expressing cells exposed to the TRP pore blocker ruthenium red (RR), and (4) Magneto2.0 expressing cells in Ca^{2+} free extracellular media. We observed calcium influx immediately following magnetic stimulation but invariably, maximal calcium fluorescence was observed minutes after magnetic field stimulation of Magneto2.0 expressing cells, which was not observed in any of the above control conditions (Fig. 1g). We found that the delayed calcium response in Magneto2.0+ cells was caused by calcium release from intracellular stores following magnetically induced depolarization since this secondary response was eliminated following depletion of intracellular calcium stores by thapsigargin, a sarco-endoplasmic reticulum calcium transport ATPase pump inhibitor[82] (Supplementary Fig. 6). However, we sought to determine if the increase in calcium signaling concomitant with magnetic field stimulation was GSK205 sensitive, which would suggest that the signal is TRPV4

dependent[83]. We thus stimulated and quantified the change in calcium fluorescence of mCherry+ *Magneto2.0-p2A-mCherry* transfected cells during magnetic field application both in the presence and absence of the specific TRPV4 inhibitor GSK205. We observed a magnetic field dependent calcium increase in the GSK205-untreated Magneto2.0 expressing cells compared to stimulated GSK205-treated cells (two-way ANOVA, $p<0.0001$) (Fig. 1h). Moreover, 70±5.1% (mean±SEM) of Magneto2.0+ cells responded to magnetic fields (n=3 coverslips, n=58 cells) with an average maximal change in calcium fluorescence of 29±9.8% (mean±SEM) during stimulation compared to only 6.5±0.9% (mean±SEM) for the GSK205-treated population (n=3 coverslips per condition, n=88 GSK205-treated cells, n=57 untreated cells, unpaired two-tailed t-test, $t_{143}=2.819$, $p=0.0055$). Importantly, all observed changes in calcium fluorescence were noticeably improved over the poorly trafficked prototype channel (Supplementary Figs. 3, 4a). These data demonstrate that Magneto2.0 is a magnetically sensitive, genetically encoded actuator that can manipulate cellular activity *in vitro*.

(b) Electrophysiological characterization of Magneto2.0 in the mammalian brain

These preliminary experiments prompted us to precisely determine the temporal kinetics of Magneto2.0 activation since the future utility of Magneto2.0 is contingent on its rapid activation in response to magnetic fields in live tissues. To this end, we generated an adeno-associated virus (AAV) to express Magneto2.0 in mammalian cells under control of the cytomegalovirus (CMV) promoter using the double-floxed inverse open reading frame (DIO) approach (*CMV::DIO-Magneto2.0*). This strategy enables permanent Cre-dependent expression of a reversed lox site-flanked gene through Cre-lox mediated recombination

(Fig. 2a)[84]. We bilaterally co-injected the medial entorhinal cortices (mECs) of WT mice with an AAV1 containing *CMV::DIO-Magneto2.0* and an AAV9 carrying Cre recombinase fused to enhanced green fluorescent protein (EGFP) under control of the calcium/calmodulin-dependent protein kinase II alpha (CamKIIα) promoter (*CamKIIα::Cre-EGFP*), which will express Magneto2.0 in excitatory neurons (Fig. 2b). To test whether Magneto2.0 could elicit action potentials (APs) in neurons from brain slice preparations in response to magnetic fields, we recorded from EGFP+ neurons in the mEC of WT mice doubly transduced with AAVs carrying *CMV::DIO-Magneto2.0* and *CamKIIα::Cre-EGFP* under whole-cell current clamp conditions. Upon application of a ~50 mT static magnetic field delivered by a NdFeB rare earth magnet, neurons in the mEC reliably fired a series of APs akin to spiking behavior evoked by injection of 300 pA of depolarizing current (Fig. 2c, Supplementary Fig. 7a). APs were elicited by both current injection and magnetic fields in 12/12 strongly EGFP+ neurons tested (n=5 mice; n=2 mice excluded due to low EGFP expression). Measurement of time to threshold and time to peak for APs evoked either by current injection or magnetic fields revealed no differences (Supplementary Fig. 7b). Membrane properties, such as resting membrane potential, AP amplitude, upstroke velocity, AP width, and firing threshold were similar between the two stimulation conditions (Supplementary Fig. 7c-g). As controls, we measured that magnetic stimulation initiated APs at a comparable rate to current injection (Supplementary Fig. 8a) and did not cause electrical interference in electrophysiology measurements (Supplementary Fig. 8b). To test if the magnetically evoked firing was due specifically to activation of TRPV4, we bathed brain slices in the selective TRPV4 antagonist GSK205 (n=3 neurons from 3 mice). After a 10-minute incubation with GSK205, magnetic stimulation failed to evoke APs (Fig.

2c, right panel), suggesting that the observed APs were due to Magneto2.0 activation. To determine whether magnetic stimulation affects mEC neurons not expressing Magneto2.0, we magnetically stimulated cells transduced with AAVs delivering *CMV::DIO-Magneto2.0* and *CamKIIα::EGFP*, thus preventing Cre-dependent expression of Magneto2.0. We found that stimulation with magnetic fields did not evoke APs in non-Magneto2.0 expressing EGFP+ neurons of the mEC, although these neurons fired spike trains in response to injection with 300 pA of depolarizing current (n=6 neurons from 3 mice) (Fig. 2d, Supplementary Fig. 7h). In sum, we found that only Magneto2.0-expressing neurons of the mEC fired APs in response to magnetic field stimulation, and bath application of GSK205 blocked these responses (Fig. 2e). These data support the notion that activation of Magneto2.0 can rapidly and reversibly depolarize neurons leading to remote control over neural circuit dynamics.

(c) Genetically targeted remote magnetic control over zebrafish tactile behaviors

We next began validation of Magneto2.0 function *in vivo*. We first sought to remotely modulate a simple behavior of the zebrafish, *Danio rerio.* We transiently expressed Magneto2.0 in Rohon-Beard sensory neurons (5 Magneto2.0+ Rohon-Beard neurons per fish, n=9 fish), using regulatory sequences of the *ngn1* promoter[85,86]. We identified mosaic zebrafish expressing Magneto2.0 in Rohon-Beard neurons by selecting for animals that also expressed a co-injectable fluorescent marker in the heart (Supplementary Fig. 9a). We sought to determine whether magnetic stimulation of zebrafish expressing Magneto2.0 led to an increase in calcium signaling within Rohon-Beard neurons. To this end, we performed GCaMP imaging of live, 48 hours post-fertilization (hpf) zebrafish larvae expressing

Tg(s1020t::Gal4);*Tg(UAS::GCaMP3)*;*ngn1::Magneto2.0-p2A-mCherry*, which enables detection of activated neurons through the genetically encoded calcium sensor, GCaMP3[87], which is expressed in ventral spinal cord neurons[88]. This transgenic combination enables direct visualization of calcium transients in response to magnetic stimulation through dual labeling of GCaMP3+ and mCherry+ Rohon-Beard neurons. We delivered a 50 mT static magnetic field via NdFeB rare earth magnets and observed an immediate increase in GCaMP3 fluorescence in stimulated Magneto2.0+, mCherry-labeled Rohon-Beard neurons but not in adjacent mCherry- neurons populating the spinal cord (Fig. 3a, Supplementary Fig. 10a). We determined that 17/20 mCherry+ neurons responded above the 6.9±0.15% (mean±SEM) average maximal fluorescence change of control, mCherry- cells (Supplementary Fig. 10a), suggesting that magnetic stimulation *in vivo* will reliably activate Magneto2.0+ neurons, consistent with both our calcium imaging and slice electrophysiology data. We next tested whether remote activation of Rohon-Beard neurons is sufficient to modulate the behavior of *ngn1::Magneto2.0* zebrafish in the presence or absence of magnetic fields. We developed a magnetized behavioral testing arena formed by spacing two NdFeB rare earth magnets 6 mm apart (Supplementary Fig. 10b), which delivered a ten-fold greater magnetic field of ~500 mT to zebrafish larvae than the GCaMP assay. We hypothesized that even if only a few Rohon-Beard neurons were activated by Magneto2.0, the stereotypical escape response would nevertheless induce a coiling behavior, as demonstrated previously[86,89]. Indeed, in response to a 500 mT magnetic field, groups of 24 to 34 hours post fertilization (hpf) *ngn1::Magneto2.0* expressing zebrafish larvae coiled more frequently compared to those not exposed to a field (Fig. 3b, Supplementary Movies 1-2). In contrast to *ngn1::Magneto2.0* fish, which displayed an

approximate ten-fold increase in coiling behavior upon magnetic field exposure, there was no observable change in this behavior for either control group—uninjected WT fish or *ngn1::TRPV4-p2A-ferritin* fish, which bicistronically express independent, unfused TRPV4 and ferritin moieties (Fig. 3c). Consistent with *in vitro* findings, fish expressing the Magneto prototype channel under control of the *ß-actin* promoter exhibited a response that was five-fold smaller than that of fish expressing Magneto 2.0 (Supplementary Fig. 9b-d). Finally, we confirmed that Magneto2.0 expression did not disrupt normal peripheral projections of Rohon-Beard neurons by examining red fluorescent protein (RFP) expression in sensory neurons of *Tg(isl1::rfp)* fish and *Tg(isl1::rfp);ngn1::Magneto2.0-IRES-nlsegfp* chimeric fish (Supplementary Fig. 10c-f). Together, these results confirm that Magneto2.0 is a viable candidate for remotely controlling neuronal activity and animal behavior *in vivo*.

(d) Remote control of mammalian neural activity in freely behaving mice

To determine if Magneto2.0 is capable of controlling mammalian neural activity *in vivo*, we performed electrophysiology measurements in freely behaving mice transduced with an AAV1 carrying *CMV::DIO-Magneto2.0*, which expresses Magneto2.0 in a Cre-dependent manner. We aimed to test if Magneto2.0 is capable of rapidly activating a large nucleus deep within the brain, which is more challenging when using optical actuators. To this end, we used mice expressing Cre recombinase under control of the dopamine receptor 1 promoter (*Drd1a::Cre*), which is expressed in approximately half of the medium spiny neurons (MSNs) of the striatum[90]. We then transduced striatal neurons of *Drd1a::Cre* mice with an AAV1 carrying Magneto2.0 and two weeks post-viral injection, we performed

extracellular single-unit recordings with tetrode microdrives on Magneto2.0 expressing striatal cells in freely behaving mice and examined the effects of magnetic stimulation on neural firing (Fig. 4a). For this assay, we designed a magnetized chamber (23 cm x 4 cm x 18 cm) consisting of NdFeB magnets embedded in the chamber walls (Fig. 4b) and quantified the firing rates of striatal neurons under three conditions: (1) at baseline without magnetic stimulation, (2) during exposure to 50-250 mT magnetic fields within the chamber, and (3) post-magnetic field exposure. We classified recorded cells into two main groups based on firing rate: slow-spiking (<5 Hz) and fast-spiking (>5 Hz) neurons with mean firing rates of 2.1±0.3 Hz (mean±SEM) and 8.6±0.6 Hz (mean±SEM), previously described as putative MSNs (either D1R+/D2R- or D1R-/D2R+) and GABAergic interneurons (D1R-), respectively[91]. Exposure of these mice to magnetic fields produced a 43.8±20.3% increase in the overall firing rate of slow-spiking putative MSNs (Fig. 4c-e). Importantly, the firing rate of putative GABAergic interneurons remained constant (Fig. 4c-d). Subsequent to magnetic stimulation, 66.7% of putative MSNs returned to baseline firing rates, while the putative interneuron firing rate again remained at baseline (Fig. 4f). Finally, we observed an increase in the firing rate of slow-spiking, but not fast-spiking, neurons of the striatum following systemic administration of the D1R agonist, SKF81297 (Supplementary Fig. 11a), suggesting that the D1R+ population responsive to magnetic fields are indeed slow-spiking neurons. Together, these data demonstrate that Magneto2.0 is capable of controlling neural firing in deep brain regions in response to magnetic fields.

(e) Remote magnetogenetic control of D1R-mediated striatal reward valence

Ultimately, we sought to determine whether Magneto2.0 dependent control of neural activity *in vivo* could translate to control over complex mammalian reward behaviors regulated by dopamine signaling[92]. While optogenetic studies have implicated the dopaminergic signaling axis in causally mediating reward behavior[93], it is unclear whether activation of postsynaptic D1R+ neurons is sufficient for controlling this effect. For instance, optogenetic stimulation of one subset of striatal D1R+ neurons is not causally responsible for induction of conditioned place preference (CPP)[94]. Conversely, studies using systemic pharmacological manipulations with D1R agonists confirm that activation of D1R+ neurons is sufficient to evoke CPP[95,96], suggesting that broadly activating D1R+ neurons may cause reinforcing behaviors. Optogenetic techniques are intrinsically limited in the number of neurons that can be activated simultaneously via fiberoptic implants and pharmacological approaches lack genetic specificity. However, a magnetogenetic paradigm circumvents both obstacles simultaneously allowing resolution of this discrepancy with cell-type specificity and a real time behavioral output. We tested the sufficiency of D1R+ neurons in eliciting reward conditioning by unilaterally injecting the striata of WT and *Drd1a::Cre* mice with an AAV1 carrying *CMV::DIO-Magneto2.0* and subjecting the mice to a real time place preference (RTPP) assay where they could choose between a magnetized arm, lined with eight permanent NdFeB magnets delivering a magnetic field gradient of 250-50 mT, and a non-magnetized arm (Fig. 5a). We observed that Magneto2.0 expressing *Drd1a::Cre* mice showed a significant preference for the magnetized arm of the RTPP chamber in contrast to WT mice (one-way ANOVA, $p=0.0152$), which exhibited no preference (Fig. 5b-e). Moreover, removal of the magnets from the chamber eliminated the preference of Magneto2.0 expressing *Drd1a::Cre* mice for either arm, a response identical

to WT mice (Fig. 5c), demonstrating that RTPP is dependent on D1R stimulation. As a control, we measured no differences in overall locomotion between unilaterally injected WT and *Drd1a::Cre* mice using a modified open field assay (Supplementary Fig. 11b-c). These data show: (1) that broad activation of D1R+ neurons of the striatum is sufficient to control reward salience and (2) that Magneto2.0 can be used for remote control of complex mammalian behaviors mediated by deep brain nuclei in freely moving mice.

III. Discussion

In total, we have engineered and optimized a genetically encoded magnetogenetic actuator, Magneto2.0, and applied it to the nervous system in freely behaving animals. This is the first demonstration of *bona fide* magnetic control of the nervous system using engineered actuators, which we confirmed electrophysiologically and behaviorally using both zebrafish and mice. We have shown that Magneto2.0 remotely controls both neural firing rates and behavior on a rapid and physiologically relevant timescale, which is a prediction offered by the authors of an earlier study employing magnetogenetics to study insulin signaling[65]. Our single-component magnetogenetic system represents a significant advance in the ability to study neural circuits with relative ease as broad populations of genetically defined cells can be remotely activated in freely behaving animals. We applied Magneto2.0 to the study of reward behaviors to directly measure the behavioral consequences involved in remotely modulating large populations of cells participating in specific neural circuits[97]. Our findings also shed light on the sufficiency of D1R+ neurons to control reinforcing behaviors, which is consistent with the results of a recent study investigating D1R+ neuron necessity in these processes[61]. Magneto2.0 represents a new

prototype for a novel class of magnetogenetic remote controlled actuators. While we initiated our actuator design using TRPV4 because of its small size and known pressure sensitivity[74,98–100], Magneto suffers from the unique disadvantage of remaining sensitive to several endogenous stimuli known to activate TRPV4[75,76], a problem not encountered with many opto- or chemogenetic methods. Future studies will optimize Magneto2.0 such that it no longer responds to these stimuli and responds to magnetic fields only. In addition, it will be useful to understand if Magneto functions because of the mechanosensitive nature of TRPV4 or whether this property is immaterial to its magnetic activation. Continued optimization and utilization of this magnetogenetic actuator will position the field to better understand neural development, function, and pathology.

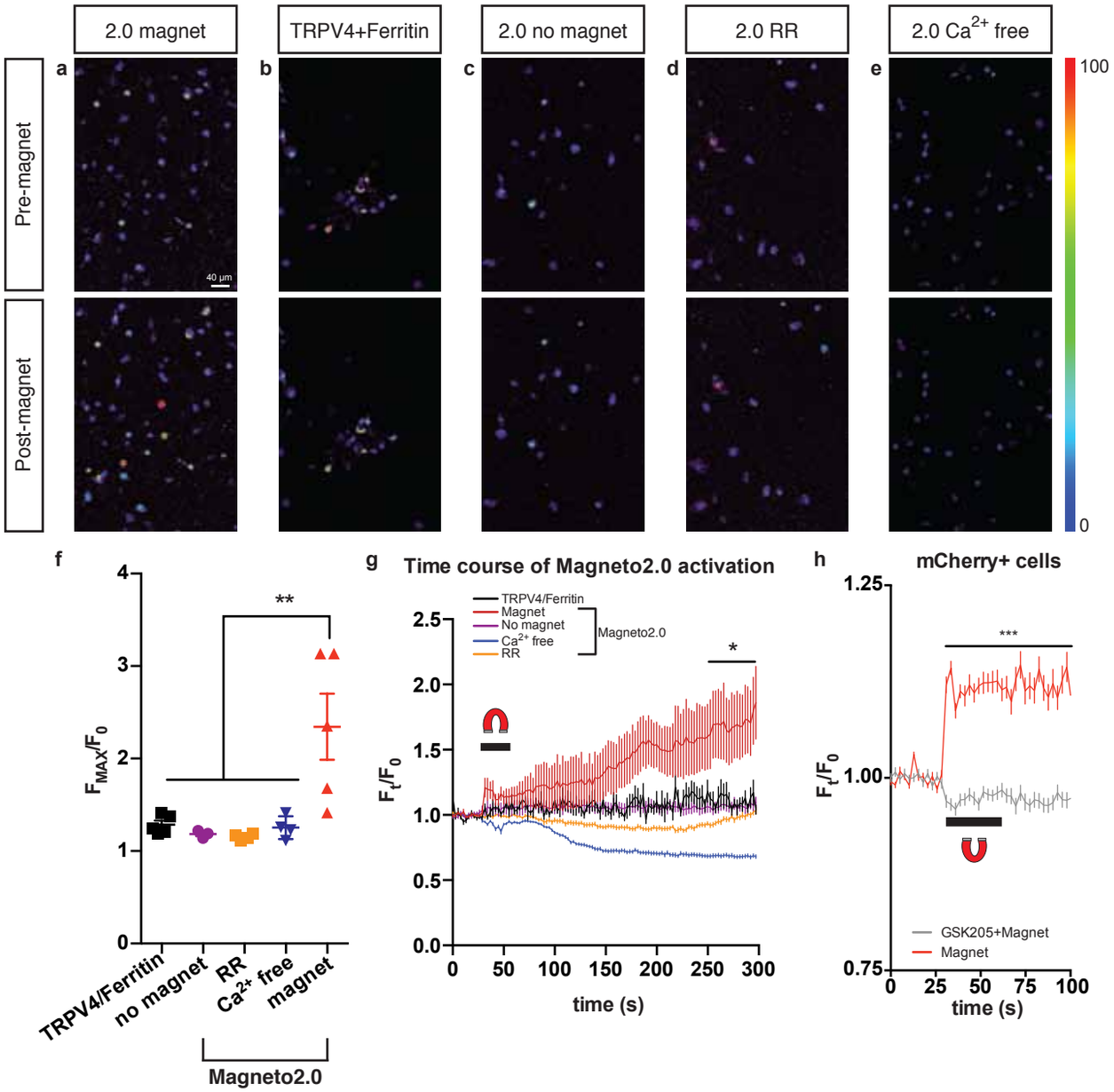

Figure 1: Remote control of calcium signaling using Magneto2.0

(a-e) *In vitro* calcium imaging micrographs of Fluo-4-loaded HEK293 cells before and after 3 pulses of 40-50 mT, 0.1 Hz, 90% duty cycle magnetic stimulation. (f) Quantification of calcium fluorescence fold change in response to the given condition. All experiments treated with magnetic fields except "no magnet" condition. Shown are n=3-5 coverslips per condition, n=114-396 total cells analyzed per condition, n>30 cells analyzed per coverslip. One-way ANOVA, Bonferroni post-test, ($F_{4,16}$=7.268, p=0.0016). (g) Average temporal kinetics of all cells analzyed within a single coverslip per condition (n=102 Magnet; n=48 TRPV4/ferritin; n=50 No magnet; n=45 Ca^{2+} free; n=45 RR). Horizontal bar/horseshoe indicates magnetic field application. Two-way ANOVA, Bonferroni post-test, p<0.05 for all time points from 250 s onward compared to "Magnet." $F_{5,38304}$=192.9. (h) Kinetics of calcium fluorescence fold change within mCherry+ cells in response to magnet in the presence or absence of the TRPV4 inhibitor, GSK205 (10 µM). n=3 coverslips per condition. Data represent all mCherry+ cells analyzed (n=88 GSK205-treated, n=57 untreated). Two-way ANOVA, Bonferroni post-test. p<0.001 for all time points from 30 s onward. $F_{39,5680}$=23.7. Data shown as mean±SEM. ***p<0.001, **p<0.01, *p<0.05.

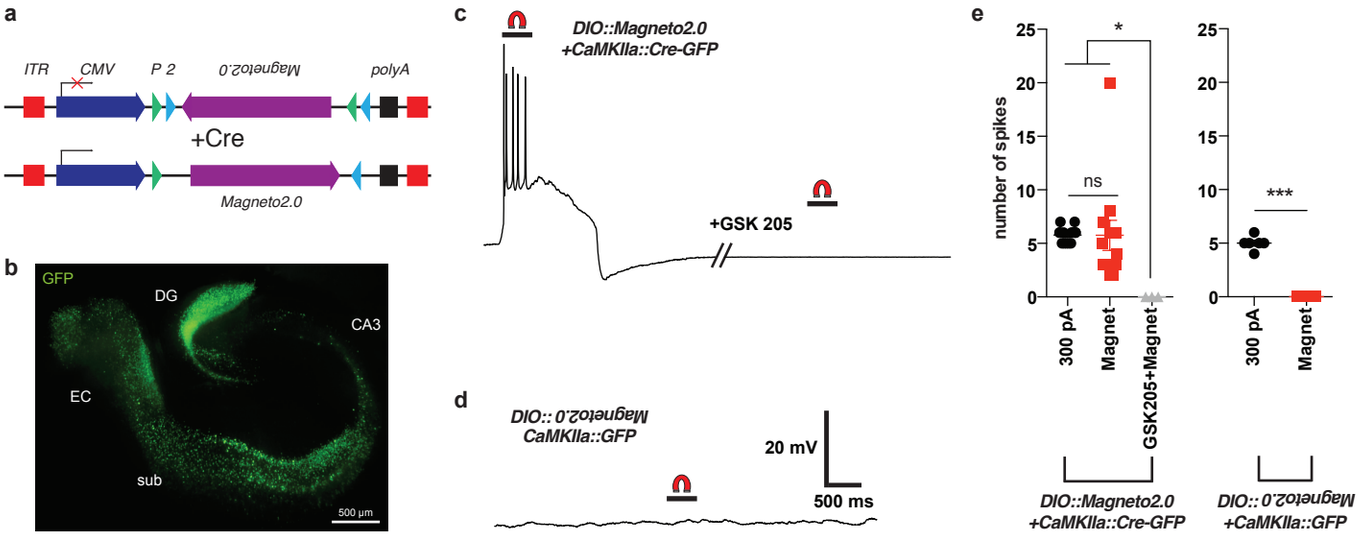

Figure 2: Electrophysiological characterization of Magneto2.0 in mouse brain slices
(a) Schematic of viral vector. ITR: inverted terminal repeats; CMV: cytomegalovirus promoter; P: loxP site; 2: lox2272 site. (b) GFP immunostaining of a WT mouse brain slice showing areas of viral transduction. Hippocampus/entorhinal cortex was doubly transduced with two AAV vectors: AAV1 carrying *CMV::DIO-Magneto2.0* and AAV9 carrying *CaMKIIa::Cre-EGFP*. DG: dentate gyrus, sub: subiculum, EC: entorhinal cortex. (c) Magnetically evoked spike trains of two independent current-clamped mEC neurons transduced with *CaMKIIa::Cre-EGFP* and *CMV::DIO-Magneto2.0*. Neurons were stimulated with a 50 mT static magnetic field delivered by a permanent magnet. Magnetically evoked APs were abolished by bath application of 10 µM GSK205. (d) Sample trace from a GFP+ current-clamped mEC neuron transduced with *CaMKII::EGFP* and *CMV::DIO-Magneto2.0* but not expressing Magneto2.0. No action potentials are elicited in response to magnetic stimulation. (e) Quantification of the number of spikes compared between current injection (n=14 cells) and magnetic stimulation (n=12 cells) for GFP+ cells. No magnetically induced APs are observed during bath application of GSK205 (n=3 cells) or when Magneto2.0 is not expressed (300 pA: n=5 cells; Magnet: n=3 cells). Cells are from a total of n=8 mice, with at least n=3 mice per condition. *left panel:* One-way ANOVA, Bonferroni post-test. $F_{2,26}$=4.301. p>0.9999 (300 pA vs. Magnet), *p=0.0273 (300 pA vs. GSK205+Magnet), *p=0.0313 (Magnet vs. GSK205+Magnet). *right panel:* unpaired two-tailed t-test. t_7=13.23, ***p<0.0001. ns: not significant. Data shown as mean±SEM.

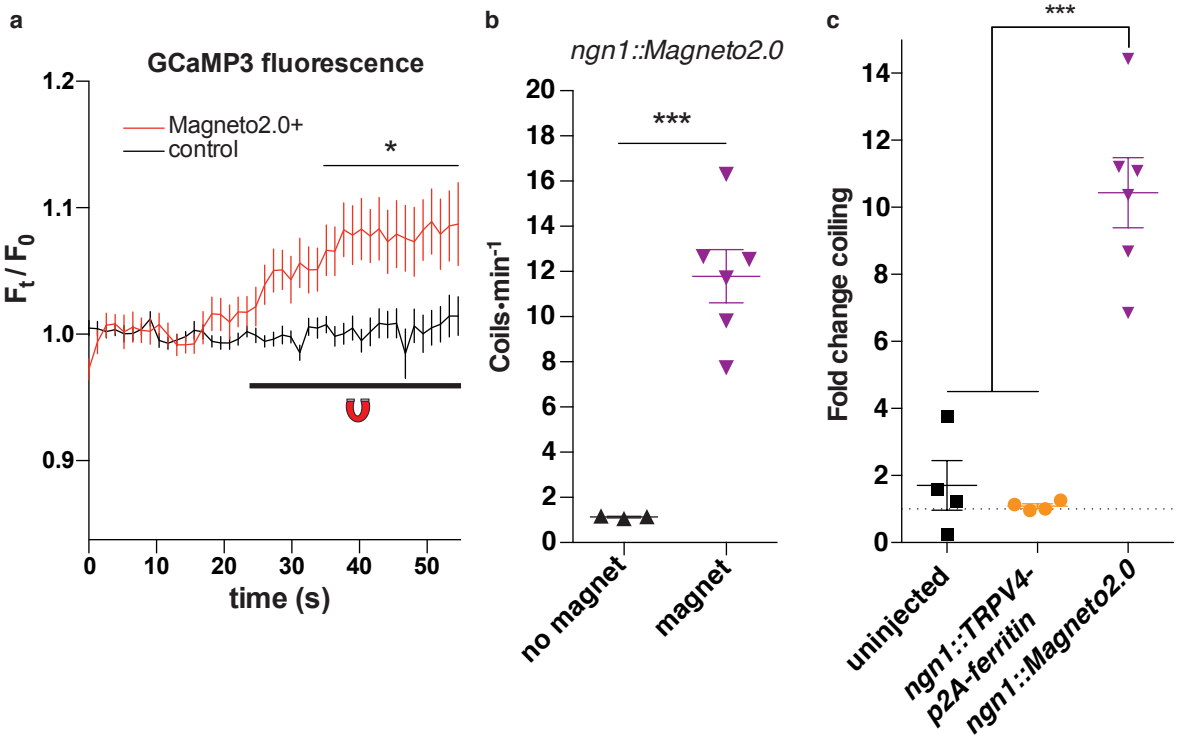

Figure 3: Magnetic control over zebrafish tactile behavior *in vivo*

(a) Quantification of GCaMP3 fluorescence in mCherry+ Rohon-Beard sensory neurons and mCherry- spinal cord neurons in 48 hpf zebrafish larvae expressing *ngn1::Magneto2.0-p2A-mCherry* n=20 mCherry+, n=33 mCherry- neurons. Cells from 8 experiments using n=5 zebrafish from 2 independent injection cohorts. Two-way ANOVA, Bonferroni post-test, $F_{42,2339}$=3.248, *p<0.05 for all points from 35-55 seconds. (b) Coiling rate of 24-36 hpf *ngn1::Magneto2.0* fish; unpaired two-tailed t-test, (t_7=6.152, ***p=0.0005). (c) Fold change in coiling of fish cohorts aged 24-36 hpf; one-way ANOVA, Bonferroni post-test ($F_{2,11}$=39.01, ***p<0.0001). Data pooled from 2 injections per genotype, shown as mean±SEM. n=17-27 fish per condition.

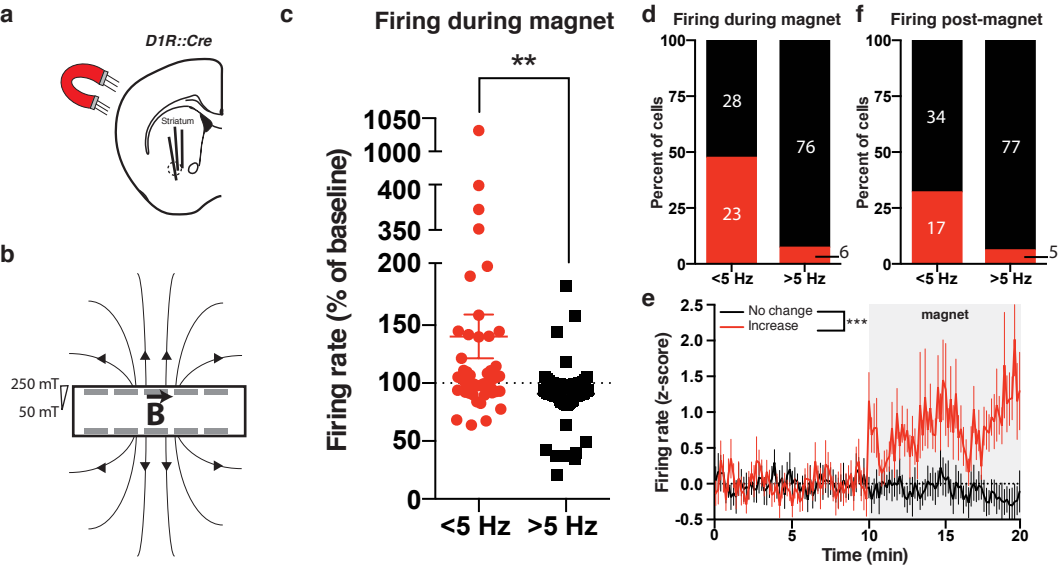

Figure 4: Magnetogenetic control of the mammalian nervous system *in vivo*

(a) Representation of magnetic stimulation and recording of D1R-expressing cells in the striatum of *D1R*::*Cre* mice. Solid lines indicate electrode placement from 3 mice; dashed circle indicates approximate injection area. (b) Cartoon of magnetized testing chamber, rare earth magnets (gray bars) are embedded in the walls, "B" represents magnetic field; strength shown as gradient. (c) Quantification of single unit average firing rate during magnetic field exposure in freely behaving mice; n=51 <5 Hz neurons, n=81 >5 Hz neurons from 5 mice (n=66, n=30, n=25, n=7, n=4 cells from each mouse). Unpaired two-tailed t-test, (t_{130}=3.210, p=0.0017). (d) Proportion of cells firing >5% over baseline during magnet exposure. (e) Standard score (z-score) over time for MSNs in (d) that fired >5% (red, n=23) vs. <5% (black, n=28). Two-way ANOVA ($F_{1,6120}$=213.6, p<0.0001). Gray box represents magnetized chamber. Dashed line shows baseline of no change. (f) Proportion of cells firing >5% over baseline post-magnet exposure. Data are shown as mean±SEM, ***p<0.001, **p<0.01.

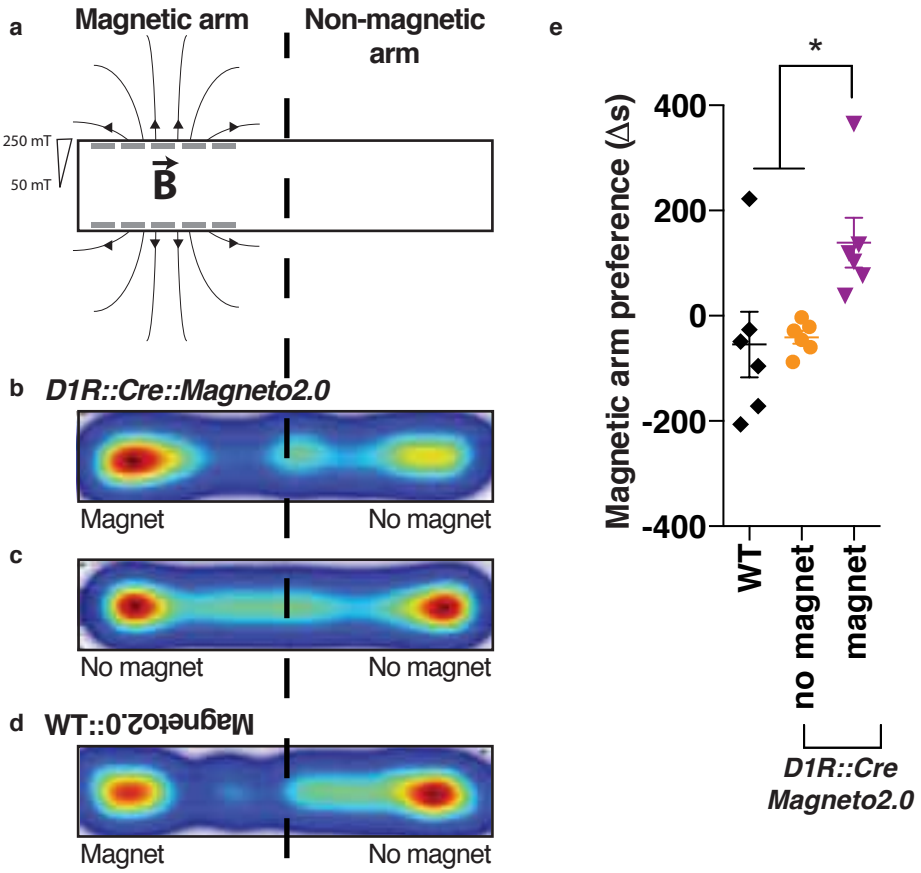

Figure 5: Activation of striatal D1R+ neurons controls reward behavior
(a) Cartoon of magnetized RTPP assay. (b-d) Representative heat maps of arm preference for each condition shown as time spent in a particular arm; mid-point of one mouse shown per map. (e) Difference in time spent in magnetic arm versus non-magnetic arm for WT and *D1R*::*Cre* mice (n=6 per genotype) transduced with *AAV*::*Magneto2.0*. "No magnet" refers to non-magnetized RTPP chamber, "magnet" refers to magnetized chamber, WT mice were only tested in the magnetized chamber. One-way ANOVA, Bonferroni post-test, ($F_{2,15}$=5.611, p=0.0152). Data are shown as mean±SEM. *p<0.05.

Figure 5 - Guler

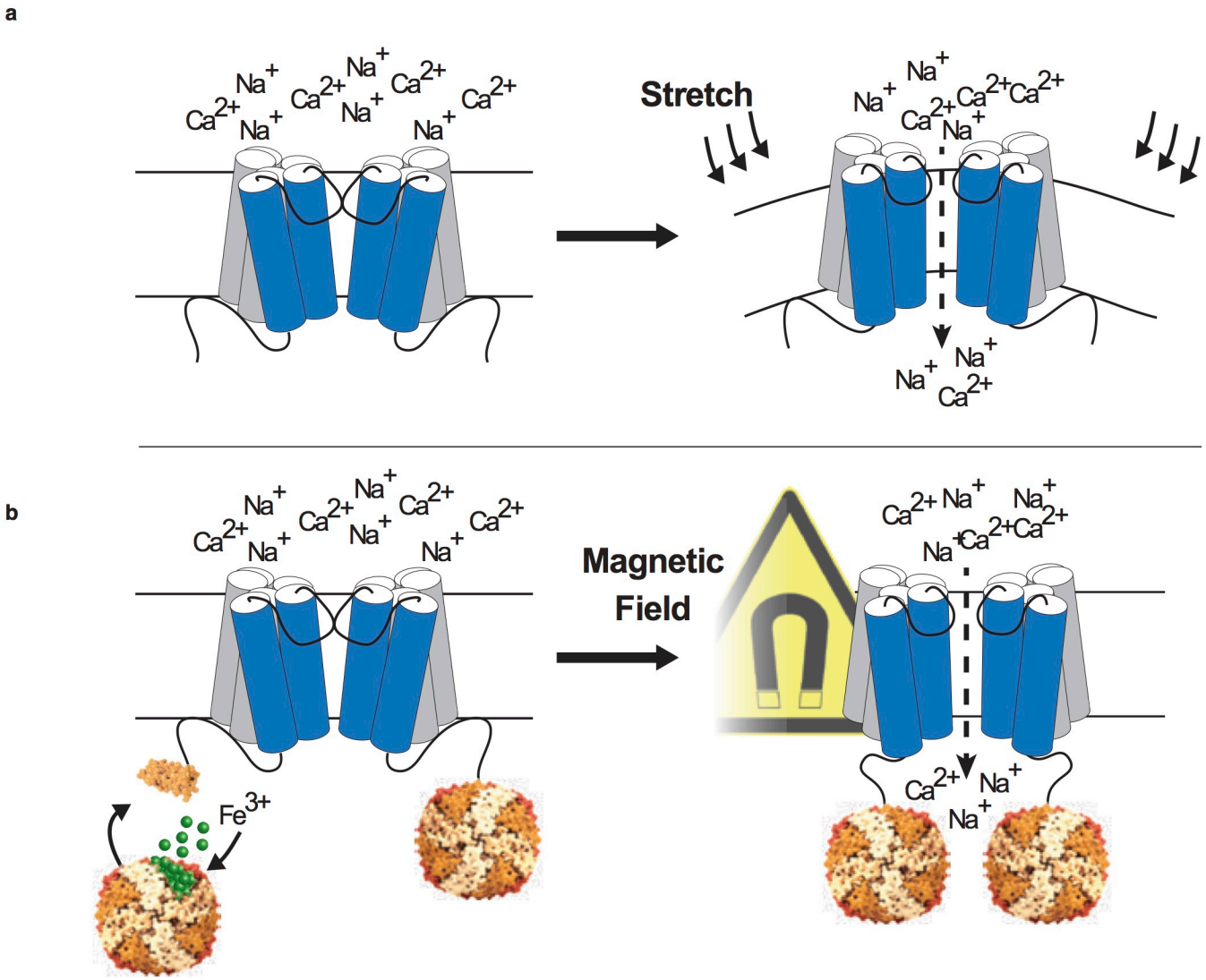

Supplementary Figure 1

Model of magnetic activation via Magneto

(**a**) The cation channel, TRPV4, is gated by stretch (among other diverse classes of stimuli), to depolarize cells. For simplicity, only two of the four homomeric subunits are shown. (**b**) Coupling ferritin to the TRPV4 C-terminus converts TRPV4 to a magnetic field detector. Gating properties were extrapolated from published descriptions of TRPV1 and TRPA1 gating mechanisms[49-51].

49. Cao *et al.* (2013) *Nature* 504, 113-118.

50. Liao *et al.* (2013) *Nature* 504, 107-112.

51. Paulsen *et al.* (2015) *Nature* 520, 511-517.

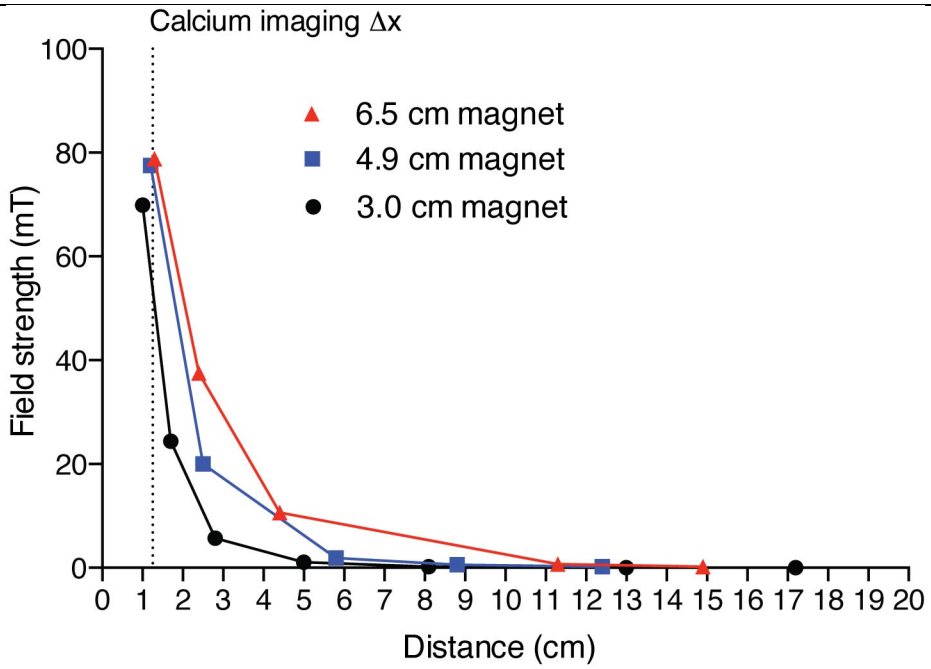

Supplementary Figure 2

Measurement of electromagnet strength over distance

Empirical determination of the strength of several electromagnets over distance powered by an identical current. Dashed line represents distance between HEK cells and electromagnet during calcium imaging assays. A 3 cm diameter magnet was used for all calcium imaging assays. Δx represents distance between magnet and cells used in calcium imaging.

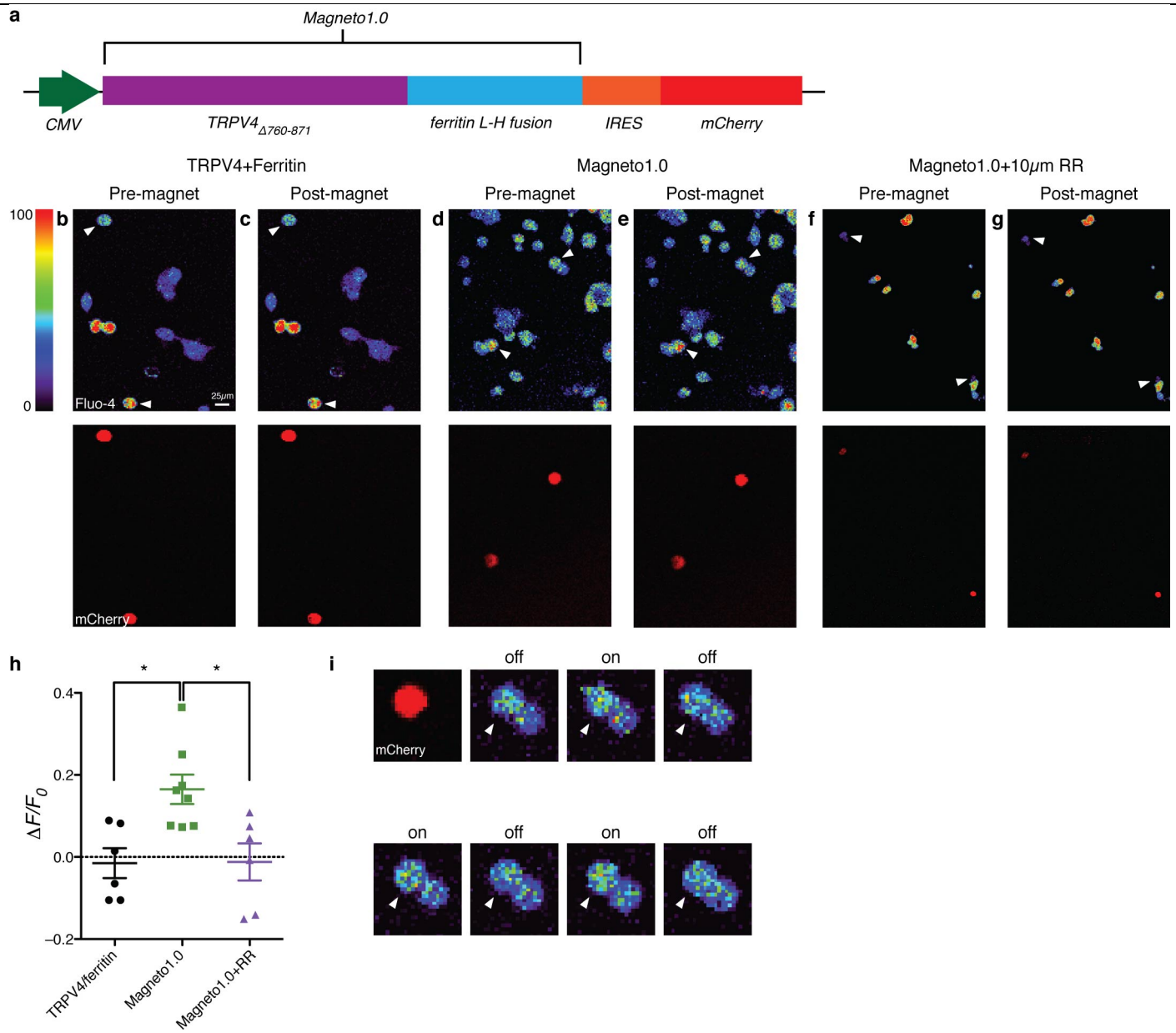

Supplementary Figure 3

***In vitro* calcium imaging using Magneto1.0**

(**a**) Mammalian expression vector schematic of Magneto1.0. (**b-g**) Representative images of HEK293 cells used for *in vitro* magnetic stimulation Fluo-4 calcium imaging. (**h**) Quantification of relative calcium fluorescence in response to magnetic stimulation of mCherry+ cells. Replicates are shown as individual coverslips equaling n=6 (TRPV4/ferritin), n=8 (Magneto1.0), and n=6 (Magneto1.0+RR). Total cells analyzed for each condition are n=545 (TRPV4/ferritin), n=565 (Magneto1.0), and n=437 (Magneto1.0+RR). One-way ANOVA, Bonferroni post-test, ($F_{2,17}$=7.509, p=0.0046). (**i**) Representative images of temporal association between calcium fluorescence and magnetic field pulses in an individual Magneto1.0-expressing cell (arrow). Field was pulsed for alternating 10 second periods of on/off. *p<0.05. Data are shown as mean±SEM.

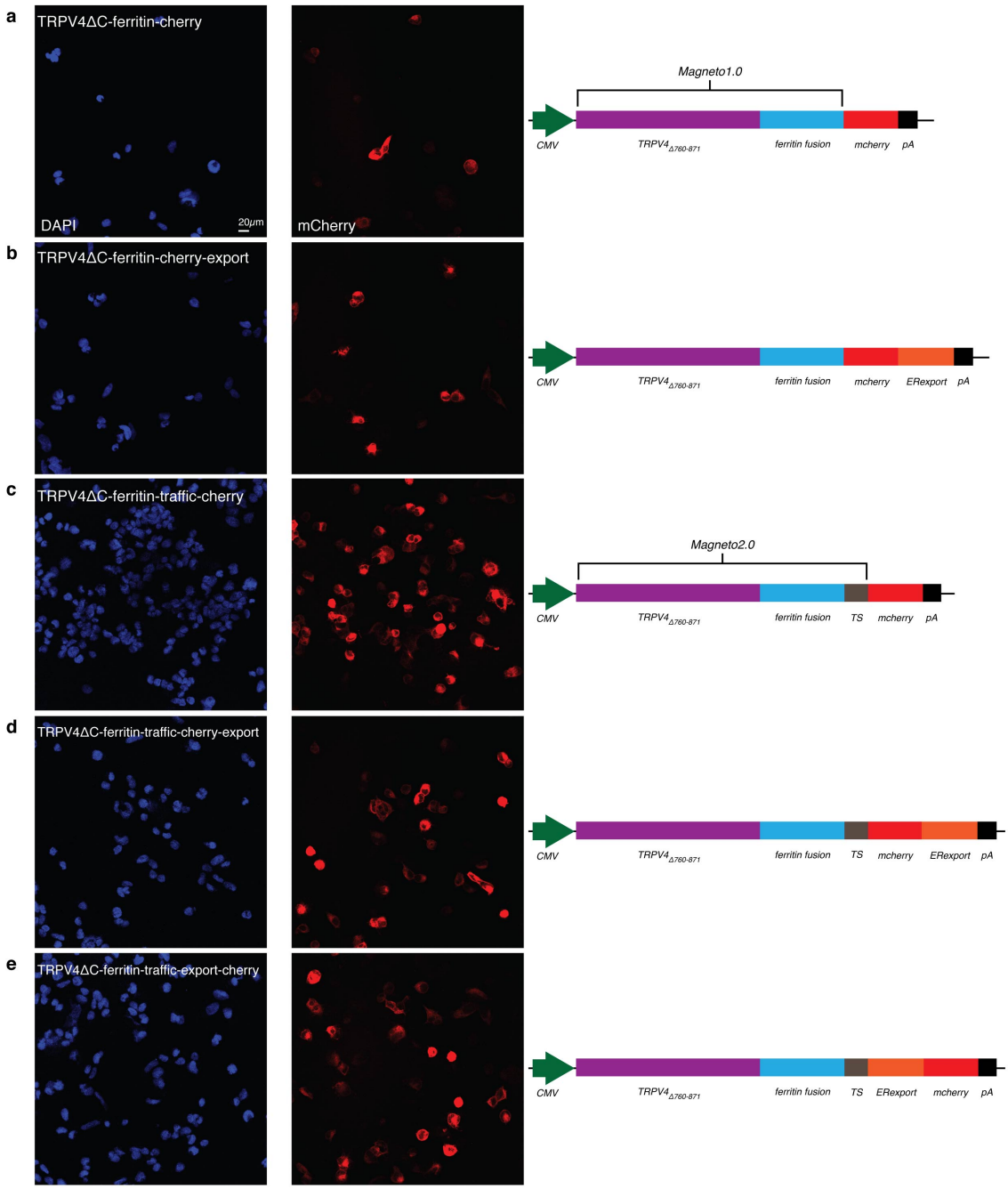

Supplementary Figure 4

Optimization of Magneto1.0 by improving cellular trafficking

(**a-e**) HEK293 cells transfected with mCherry-fused variants of Magneto1.0 with combinations of various inwardly rectifying K+ channel 2.1 (Kir2.1) trafficking signals. (**a**) Magneto1.0-mCherry shows diffuse cellular localization, poor membrane expression, and poor transfection efficiency. (**b**) Addition of ER export signal from Kir2.1 to C-terminus of Magneto1.0-mCherry peptide partially improves Magneto expression. (**c**) Addition of Kir2.1 membrane trafficking signal (TS) significantly improves membrane expression of Magneto. (**d**) Dual addition of membrane trafficking and ER export signals improves expression relative to Magneto1.0 but not relative to a single membrane trafficking signal. (**e**) Tandem Kir2.1 membrane trafficking/ER export signals on Magneto1.0 C-terminus improves expression but not relative to **c**. n=2 coverslips and >100 cells analyzed per trafficking modification examined.

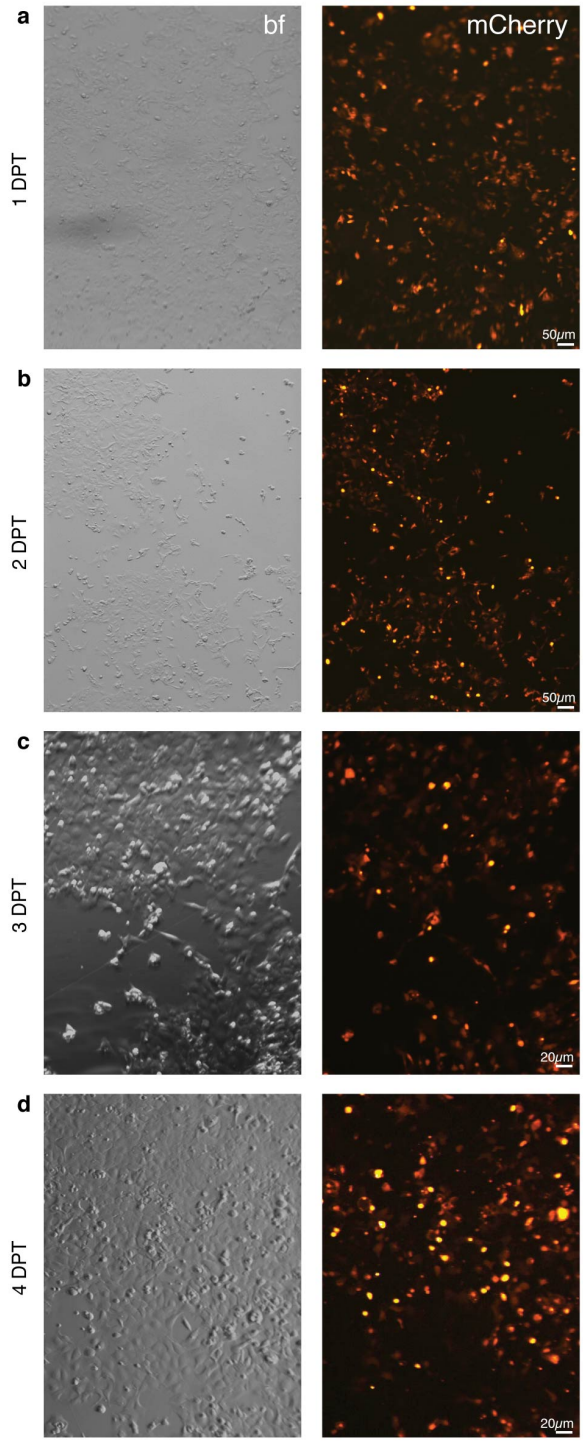

Supplementary Figure 5

Viability of Magneto2.0 transfected mammalian cells

(**a-d**) Viability of Magneto2.0 transfected HEK293 cells several days post transfection (DPT). Images show bright field and mCherry fluorescence. Zoom increased in (**c-d**) to increase single cell resolution following significant cell division. Images are representative of n>100 cells examined.

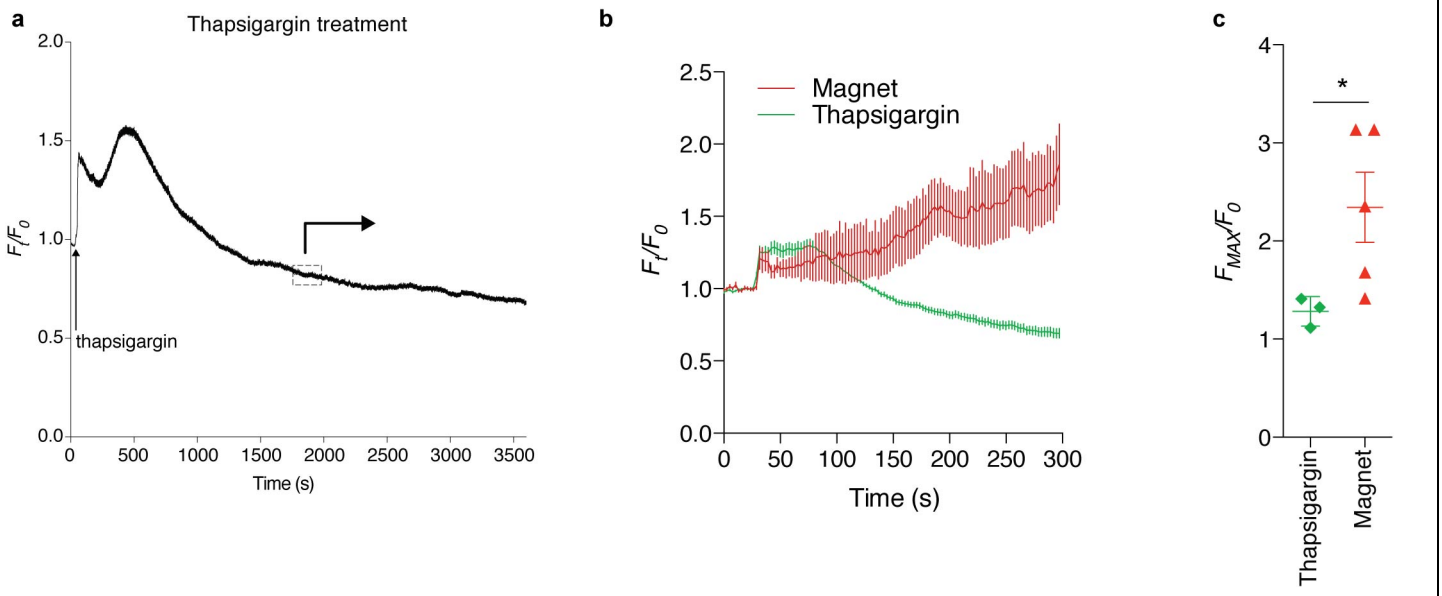

Supplementary Figure 6

Calcium imaging controls using thapsigargin

(**a**) Graph of Fluo-4 fluorescence using HEK293 cells transfected with *Magneto2.0-p2A-mCherry* and treated with thapsigargin over a period of 60 minutes. Arrow indicates addition of 1 μM thapsigargin to the imaging chamber after a 30 second baseline recording of calcium fluorescence. Dashed box indicates analysis window for "thapsigargin" experiments in panel **b**. n=114 cells analyzed from 3 independent replicates. (**b**) Time course showing the magnetic activation of Magneto2.0 expressing cells in the presence and absence of thapsigargin. All cells from one replicate shown per condition, n=102 cells (Magnet) and n=52 cells (Thapsigargin). In the "thapsigargin" condition, cells were pre-treated with 1μM thapsigargin and calcium imaging was initiated 30 minutes post-thapsigargin treatment during the window (dashed box) shown in panel **a**. (**c**) Quantification of maximal calcium fluorescence of HEK293 cells expressing Magneto2.0 and subjected to the above conditions using Fluo-4 calcium imaging 24 hours post-transfection. Values shown are the average maximal Fluo-4 fluorescence values per cell relative to baseline for each condition. Data points are shown as total cell averages among individual coverslips. n=114 (Thapsigargin) and n=396 (Magnet) cells analyzed from n=3 (Thapsigargin) and n=5 (Magnet) independent replicates. Welch's two-tailed unpaired t-test, ($t_{2.882}$=4.457, p=0.0395). "Magnet" data are duplicated from Figure 1. *p<0.05. Data shown as mean±SEM.

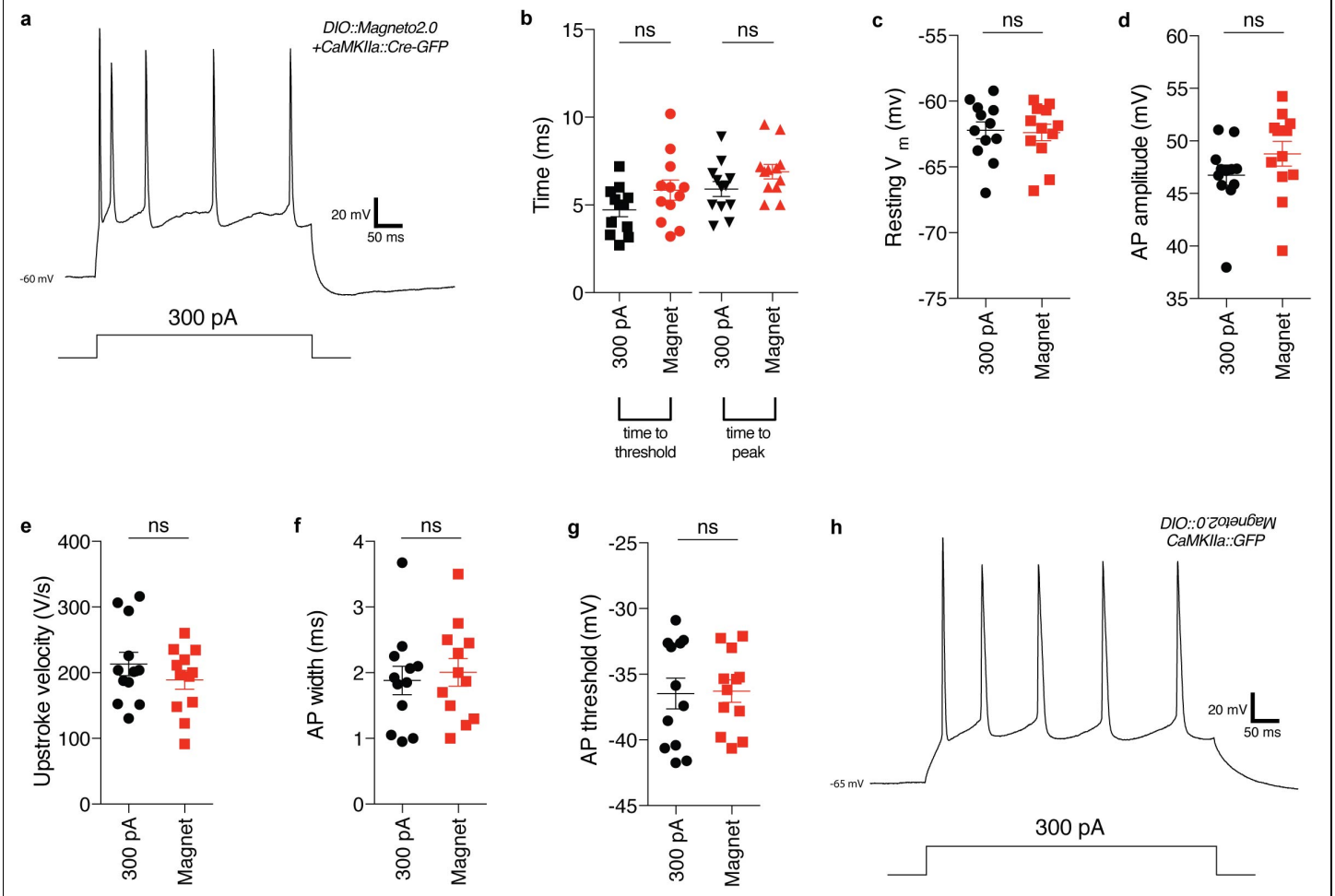

Supplementary Figure 7

Control analyses for electrophysiological characterization of Magneto2.0

(**a**) Representative trace showing that injection of depolarizing current evokes spikes in doubly transduced EGFP+ Magneto2.0 expressing neurons. (**b**) No change in AP latency between conditions of current injection or magnetic field application in transduced neurons (measured from time immediately preceding depolarization). Unpaired two-tailed t-test, (t_{22}=1.628, p=0.1178) (threshold), (t_{22}=1.676, p=0.1079) (peak). (**c-g**) Membrane properties are unchanged under conditions of either current injection or magnetic stimulation in hippocampal neurons doubly transduced with *CMV::DIO-Magneto2.0* and *CaMKIIα::Cre-EGFP*. Unpaired two-tailed t-test, (t_{22}=0.1926, p=0.8498) in **c**, (t_{22}=1.335, p=0.1954) in **d**, (t_{22}=0.1290, p=0.8985) in **e**, (t_{22}=1.052, p=0.3042) in **f**, (t_{22}=0.4086, p=0.6868) in **g**. (**h**) Injection of depolarizing current evokes APs in Cre-negative *DIO-Magneto2.0* transduced EGFP+ neurons. n=12 neurons analyzed for each condition shown in (**b-g**). ns: not significant. Data shown as mean±SEM.

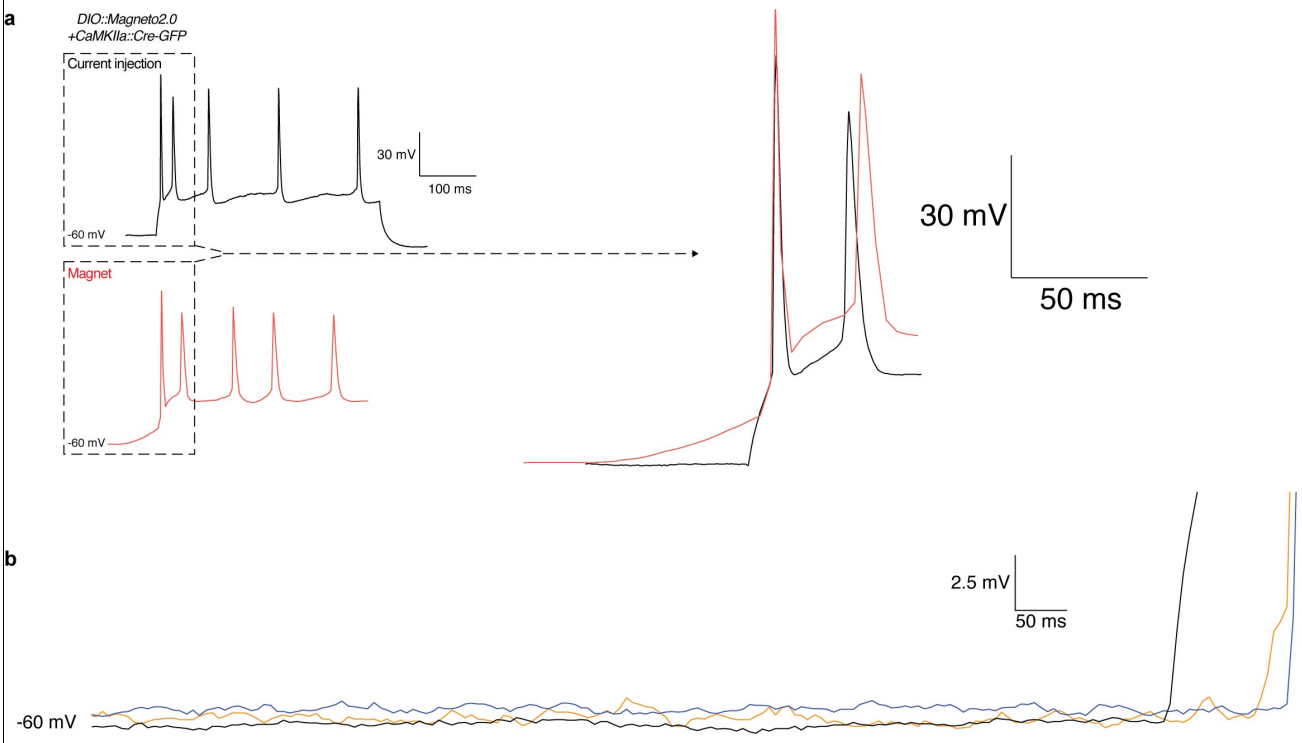

Supplementary Figure 8

Controls for magnetic stimulation in brain slice electrophysiology

(**a**) Paired traces depicting the onset of action potentials following current injection (black) and magnetic stimulation (red) for the same neuron co-transduced with AAVs carrying *CaMKIIα::Cre-EGFP* and *CMV::DIO-Magneto2.0*. Overlay shows a modest delay of action potential onset (50-100 ms) when neurons are stimulated with static magnetic fields. (**b**) Magnified traces of the resting state from three additional neurons co-transduced with the above viruses. Neurons are shown immediately prior to action potential initiation as static magnetic fields are brought more closely to the cells using a micromanipulator, a process requiring roughly 1 second. Traces do not show interference coming from ~50 mT static magnetic fields in close proximity to the recording apparatus.

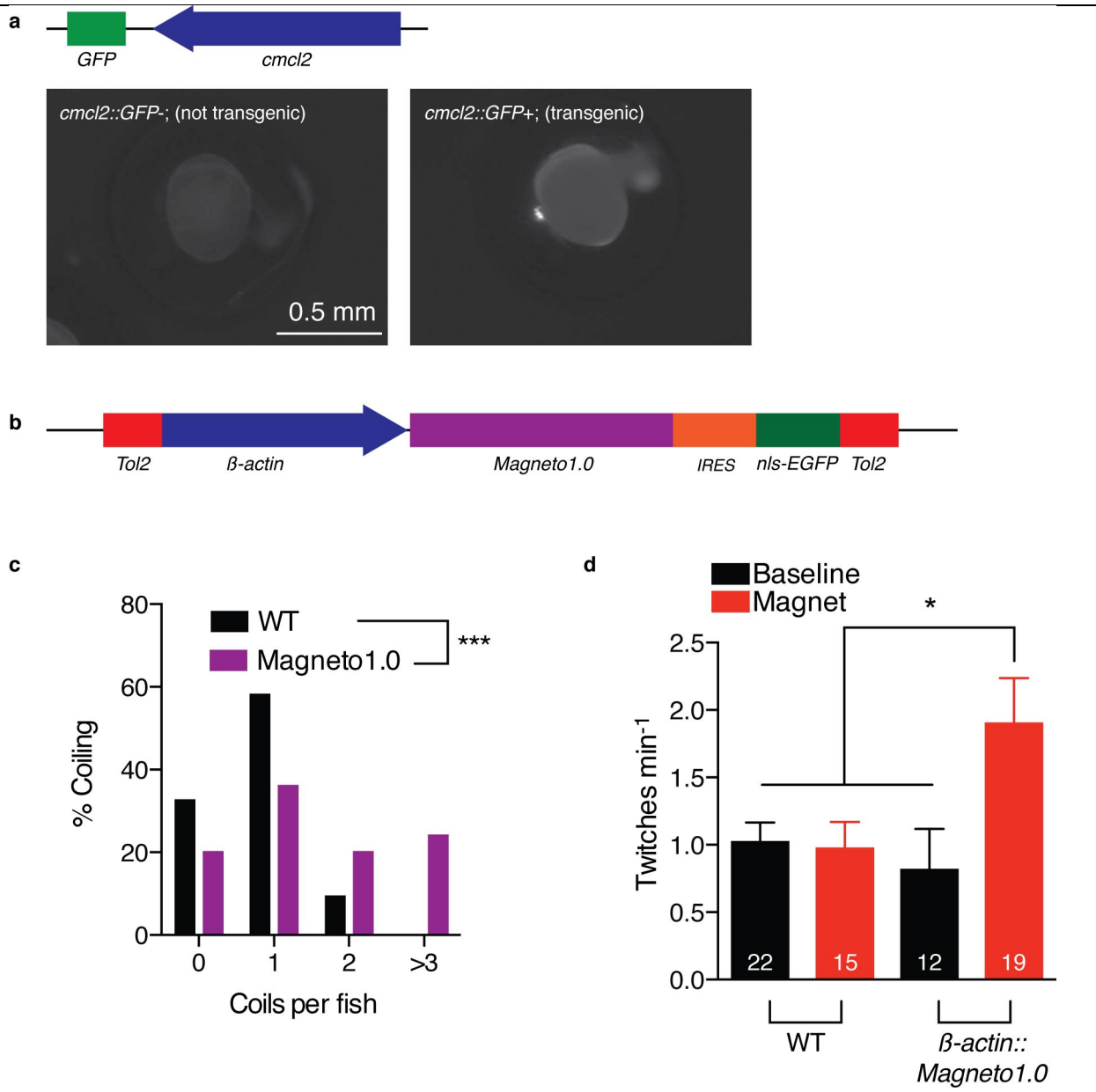

Supplementary Figure 9

Application of Magneto1.0 to zebrafish behavior *in vivo*

(**a**) Schematic of *trans cardiac myosin light chain 2* (*cmcl2*)*::GFP* element and its expression in 24 hpf zebrafish embryos for positive transgenic selection. n>100 fish examined. (**b**) Schematic of Magneto1.0 construct used: Tol2: Tol2 transposon sites; ß-Actin: promoter; IRES: internal ribosomal entry site; nls-EGFP: nuclear localized enhanced GFP. (**c**) Quantification of the number of coils in WT (uninjected) and *ß-actin::Magneto1.0* expressing 24 hpf zebrafish embryos in response to magnetic stimulation. n=43 WT, n=25 *ß-actin::Magneto1.0* fish. Statistics determined by Chi-squared analysis, (Chi^2_3=36.51, p<0.0001). (**d**) Quantification of coiling rate in WT (uninjected) and *ß-actin::Magneto1.0* expressing zebrafish. Replicates (number of individual fish) shown in columns. Statistics determined by one-way ANOVA, Bonferroni post-test, ($F_{3,64}$=3.89, p=0.0129). ***p<0.001, *p<0.05. Data are shown as mean±SEM.

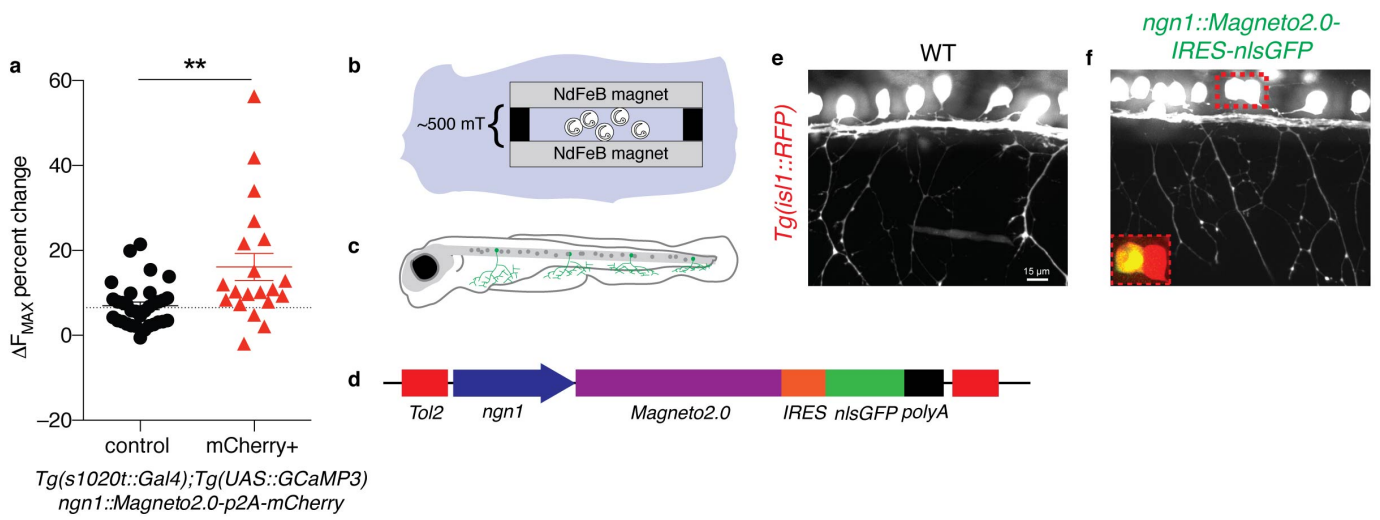

Supplementary Figure 10

Analysis of Magneto2.0 in live zebrafish

(**a**) Maximal GCaMP3 calcium fluorescence change of mCherry+ (n=20 from 5 fish) and mCherry- (n=33 from 5 fish) neurons in response to magnetic field stimulation. Dashed line indicates average GCaMP3 fluorescence value for mCherry- neurons. (17/20 mCherry+ neurons exceed this fluorescence value). Unpaired two-tailed t-test, (t_{51}=3.373, p=0.0014). (**b**) Schematic of behavioral paradigm for induction of zebrafish coiling behaviors using magnetic stimulation. (**c**) Schematic of Rohon-Beard neuron projections. (**d**) Magneto2.0 expression construct. Tol2: transposon site; ngn1: neurogenin-1 promoter; IRES: internal ribosomal entry site; nls: nuclear localization signal; EGFP: enhanced green fluorescent protein; polyA: polyadenylation signal. (**e-f**) *In vivo* imaging of Rohon-Beard neuron projections into the skin, n=10 fish examined per genotype. Inset: Magneto2.0+ (EGFP+/RFP+) and Magneto2.0- (EGFP–/RFP+) neurons. Data pooled from 2 injections per genotype. **p<0.01. Data shown as mean±SEM.

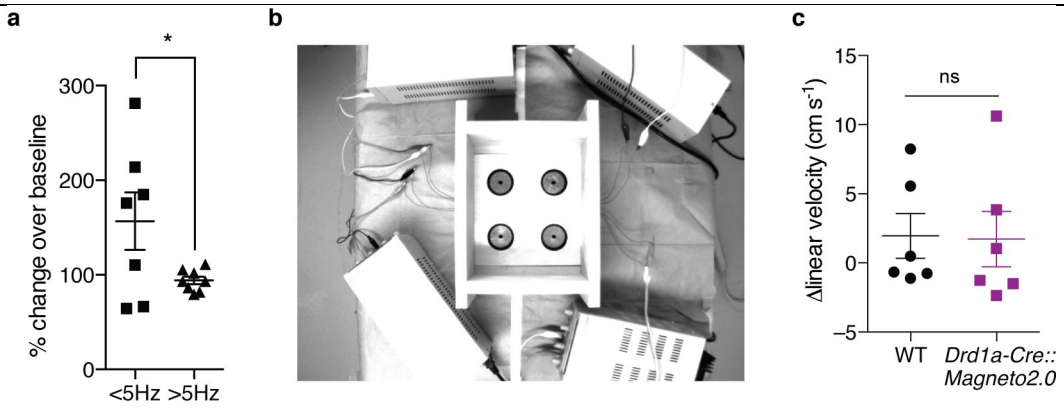

Supplementary Figure 11

Mouse behavioral controls

(**a**) Quantification of the change in firing rate relative to baseline for low-frequency and high-frequency firing single units in the striatum in response to the D1R agonist SKF81297, n=7 (<5 Hz), n=8 (>5 Hz) units examined from one *Drd1a::Cre* mouse transduced with *CMV::DIO-Magneto2.0*, unpaired two-tailed t-test, (t_{13}=2.192, p=0.0472). (**b**) Picture of magnetic open field behavioral chamber. (**c**) Quantification of change in linear velocity in open field for both groups (n=6 per genotype), unpaired two-tailed t-test, (t_{10}=0.08856, p=0.9312). *p<0.05, ns: not significant. Data shown as mean±SEM.

V. Methods

Mice information

All animal experiments were conducted in accordance with the University of Virginia Institutional Animal Care and Use Committee (IACUC). All mice were maintained on a C57Bl/6 background. Mice were housed in a vivarium on a 12-hour light/dark cycle. Mice were housed at between 1-3 mice per cage. Viral injection experiments were conducted starting at 8 weeks of age. All mice used in this study were injected between 8-10 weeks of age. Only male mice were used in this study.

Zebrafish husbandry

All animal studies were approved by the University of Virginia Institutional Animal Care and Use Committee (IACUC). Zebrafish strains used in this study were: AB*, *Tg(isl:rfp),* and *Tg(s1020t::Gal4)*;*Tg(UAS::GCaMP3)*. Embryos were raised at 28.5°C in egg water or embryo medium and staged according to hour post fertilization (hpf) or days post fertilization (dpf). Embryos of both sexes were used for experiments[101].

Molecular biology

Molecular biology was performed using standard protocols. Plasmid DNA was purified using kits from Qiagen. Restriction enzymes were purchased from New England Biolabs. Amplification of template DNA was performed with Phusion Flash (Life Technologies, F-548) and sequenced by GeneWiz. For TRPV4 S4-S5 fusion proteins, site-directed mutagenesis using Quickchange II XL Site-Directed Mutagenesis (Agilent) was performed

on TRPV4 to introduce a unique *BamHI* site, into which a successive series of DNA linkers was inserted to gradually expand the linker region flanking TRPV4 and ferritin.

Rat TRPV4 was obtained from Addgene vector: #45751, a gift from Robert Lefkowitz. To generate AAV expression vectors, we modified the Addgene vector: #35507, a gift from Karl Deisseroth. A CMV promoter was substituted in the #35507 vector, and a small pA sequence was used[102] to minimize size of the vector. A human ferritin H-L fusion gene was designed according to a previous study[78] and synthesized by IDT. Other than AAV vectors, mammalian expression vectors were maintained in the pcDNA3.0 backbone. Fish expression vectors were maintained in pDestTol2CG2 and all entry vector maps are freely available from (http://tol2kit.genetics.utah.edu). Relevant plasmids used in this study will be deposited in Addgene.

Magnets and magnetic field strength measurement

Electromagnets of varying sizes and strengths were purchased from Ebay (seller ID: pawnnew). Permanent N42 or N52 grade NdFeB magnets were purchased from CMS Magnetics via www.cmsmagnetics.com or www.amazon.com. Gaussmeters (AlphaLabs, Inc.) were used to determine the field strength of electromagnets over distance for each experiment. For the *in vivo* zebrafish and mice behavioral experiments using permanent NdFeB magnets, an online magnetic field calculator (K&J Magnetics) or a Gaussmeter (AlphaLabs, Inc.) was also used.

Cell transfection and cell culture

HEK293 cells were a gift from the University of Virginia tissue culture core. Cells used in this study were authenticated and checked for mycoplasma contamination. Cells were transfected using Lipofectamine 2000 (Invitrogen) according to standard protocols. Low passage (<40) HEK293 cells were transfected for 1-2 hours in well plates, trypsinized for 5 minutes using 10% trypsin, and replated onto poly-D lysine (50 μg/mL) and laminin-coated (1 μg/mL) glass coverslips in fresh DMEM:F12 media (Life Technologies) containing 1 mM non-essential amino acids (Gibco), 1 mM sodium pyruvate (Gibco), 10% FBS, and 1X penicillin/streptomycin (Gibco).

Microscopy

Imaging for calcium imaging and immunocytochemistry was performed on a Leica SP5 confocal with white light laser. Calcium imaging was performed using 10X magnification.

In vitro magnetic calcium imaging

Calcium imaging was performed largely as described previously[10,76]. Briefly, transfected cells were plated onto glass coverslips, incubated overnight in a humidified incubator kept at 37°C and 10% CO2. Cells were washed 3X with calcium imaging buffer (CIB) solution (105mM NaCl, 3mM KCl, 2.5mM $CaCl_2$, 0.6mM $MgCl_2$, 10mM HEPES, 1.2mM $NaHCO_3$, 100mM mannitol, and 10mM glucose, adjusted to pH 7.45 with NaOH) and loaded with 3 μM Fluo-4 diluted in CIB for 30 minutes at 37°C. Cells were then washed 3X with CIB and de-esterified for 30-60 minutes at 37°C. Coverslips were then loaded into customized imaging chambers and imaged at 10X magnification for analysis. Ruthenium red (RR), a TRP channel pore blocker, (Sigma) was used at a concentration of 10 μM and cells were

incubated with RR for ~2-3 minutes in the imaging chambers before imaging. For calcium-free media experiments, calcium in CIB was replaced with 10 mM EGTA, and cells were washed and incubated with calcium-free media. The TRPV4 specific antagonist, GSK205, was purchased from Calbiochem (616522) and used at a concentration of 10 μM. Cells were incubated in GSK205 for 15 minutes at 37°C before calcium imaging.

A magnetic stimulus was delivered using 3 cm electromagnets (purchased from eBay, sellerID: pawnnew) ruled for continuous duty, 12 VDC, 5 W, and 10 kg of pull-force. We situated the magnet directly above the imaging chamber during imaging. Using a Gaussmeter (AlphaLab Inc.), we calculated the magnetic field experienced by the cells (~1.25 cm away from the magnet) to be roughly 40-50 mT (Supplementary Fig. 1).

Imaging was performed by recording 30 seconds of baseline fluorescence and then turning on the magnet for 3-6 pulses of 10 seconds each (0.1 Hz, total time of 30-60 seconds, 90% duty cycle), using a standard DC powered delivery system. Coverslips were not analyzed if they significantly shifted during imaging.

Cells were randomly selected from an image field. Quantification was performed by averaging 30 seconds of baseline fluorescence measurements with no applied magnetic field followed by quantification of the largest three fluorescence values following magnetic stimulation. The three peak values were normalized to the average baseline fluorescence before magnetic stimulation to compute a relative fold change for each cell. Fold change

was normalized to background by respectively scaling all values by the average fold change in the background (if applicable) during magnetic stimulation.

For time course analyses (Fig. 1g-h), fluorescence data for each cell was analyzed as a relative increase over time compared to the baseline fluorescence (30 seconds) prior to magnetic stimulation.

Thapsigargin calcium imaging

HEK cells were prepared for calcium imaging as above. Thapsigargin was purchased from Sigma (T9033) and used at a working concentration of 1 μM, diluted 1:1000 in CIB. A 30-second baseline of calcium fluorescence was recorded before direct application of 800 μL of thapsigargin into the calcium imaging chamber. Calcium fluorescence was recorded for 1 hour after thapsigargin addition (Supplementary Figure 6a).

Magneto2.0-expressing cells were treated with thapsigargin and incubated at 37°C for 30 minutes before calcium imaging as thapsigargin-induced calcium release remained steady at 30 minutes after application. Cells were stimulated with magnetic fields as above: 10-second pulses of 50 mT field for 30 seconds of total field exposure.

Immunocytochemistry

Cells plated on coverslips were washed 3X with 1X PBS, fixed in 4% PFA for 1 hour at RT, washed 3X with 1X PBS, and mounted on slides with Fluoromount-G with DAPI (Southern

BioTech). Immunocytochemistry for each iteration of trafficking signals was performed on two independent populations of transfected HEK293 cells.

Fish injection

AB* or *Tg(isl:rfp)* embryos were injected at the one-cell stage with 1-2 nL of a working stock of 12.5 ng/μL DNA for each construct. At 24 hpf, embryos were screened for *cmcl2::egfp*$^{+}$ transgenics. Imaging of *cmcl2::egfp* expression was performed on every zebrafish embryo examined (n>50 positive fish).

Zebrafish GCaMP3 live imaging

Tg(s1020t::Gal4);Tg(UAS::GCaMP3);ngn1::Magneto2.0-p2A-mCherry expressing zebrafish were mounted in 0.8-2% low melting point agarose and imaged on a Leica SP5 laser-scanning confocal microscope with a white light laser. Fish were imaged using a 40X objective with water immersion. After 30-60 seconds of baseline fluorescence readings, mounted zebrafish were stimulated by a ~50 mT magnetic field delivered by a permanent NdFeB rare earth magnet. The confocal pinhole was increased to 2 μm and the scan speed was approximately 1.3 seconds per frame. n=5 fish and n=8 stimulation experiments were analyzed from two independent pools of injections.

***In vivo* zebrafish imaging**

Imaging was performed as described previously[103]. Briefly, a Quorum WaveFX-XI spinning disc confocal system (Quorum Technologies Inc.) was used, equipped with a 40X water

objective (NA=1.1) on a motorized Zeiss AxioObserver ZI microscope. Images were processed with Metamorph. n=10 fish imaged per genotype.

Zebrafish behavioral tests

Injected fish were maintained on an AB* background strain. Zebrafish embryos were behaviorally tested between 24-34 hours post fertilization (hpf). Two 2”x0.5”x0.25” N52 grade NdFeB permanent magnets were oriented such that one south and one north pole were oriented towards the fish over a fixed distance of ~1 cm. Fish were maintained in egg water during the course of behavioral testing and a 30 fps video was taken using an Axio Zoom.V16 fluorescent stereo zoom microscope. Fish were randomly selected from their groups for behavioral analysis. The videos were manually scored by counting the number of coils made by each fish over the length of the video and normalized as a rate of coiling by dividing the number of coils by the length of the video. Length of original behavioral analysis is between 2-3 minutes per video and Supplementary Movies 1-2 are shown at 8x speed. Fish tested had no prior history of behavioral testing. Animals were tested once each. Exclusion criteria for analysis consisted of stereotypy such as continuous coiling during the recording of the movie. Two uninjected WT animals were excluded from the analysis given these criteria. Behavioral testing was performed during the day at consistent times (8am-4pm).

Zebrafish whole mount immunostaining

Zebrafish were fixed and immunostained according to the protocol described previously[103]. The antibody used was rabbit anti-GFP (Invitrogen, A-6455) at a dilution of 1:1000. The secondary antibody was donkey anti-rabbit Alexa 488 used at 1:600.

Stereotaxic injection

Striatum transduction: The AAV1, *CMV::DIO-Magneto2.0-pA* containing virus used in this study was produced in the University of Pennsylvania vector core. Four injections of 1 µL of ~$5x10^{12}$ titer AAV1 virus were injected unilaterally into the striata of WT and *D1R::Cre* mice using a 30G Hamilton syringe, stereotaxic alignment system (Cartesian Research, Inc.), and automated delivery system (World Precision Instruments) while mice were under 2% isoflurane anesthesia on a heating pad. Unilateral injection was performed at (M/L: +1.6, A/P: +0.98) relative to Bregma and four 1 µL injections were performed at depths of -4.75, -3.75, -2.75, and -1.75 mm over 40 minutes at a rate of 100 nL/min. After the final injection, the syringe remained in the brain for 10 minutes, raised 0.5 mm where it remained for 5 minutes, then removed. Mice were administered 3 mg/kg ketoprofen post-injection and for 3 subsequent days and permitted to recover on a heating pad before being returned to their home cages.

mEC transduction: For expression of Magneto 2.0 into hippocampal and mEC neurons, C57Bl/6 mice (5-6 weeks old) were anesthetized with ketamine/dexmedetomidine solution and mounted on a stereotaxic apparatus. Anesthesia was maintained by inhaled isoflurane for the duration of the procedure. A small hole was opened in the skull, and a pulled glass micropipette was lowered to the target site (M/L: +/- 3.0, A/P: -3.0) at a depth

of 2.0 mm. Mice were injected with an equivolume mixture of an AAV1 carrying *CMV::DIO-Magneto2.0* and an AAV9 carrying *CaMKIIa::EGFP-Cre* (obtained from UPenn Vector Core) with titers of ~$5x10^{12}$ and ~$1x10^{13}$ infectious units per mL, respectively. 200 nL of virus was injected with pressure at a rate of ~50 nL/min. After injection the micropipette was maintained in place for 4 min before retraction. This procedure was repeated bilaterally. Mice were allowed to recover for at least 4 weeks following surgery before commencement of electrophysiology testing.

Brain slice electrophysiology

Horizontal brain slices were prepared as previously described[104]. For recordings, slices were held in a small chamber superfused with heated (32°C) oxygenated ACSF at 3 mL/min. For electrophysiology experiments, transduced mouse medial entorhinal cortex neurons were visually identified by EGFP fluorescence using a Zeiss Axioscope microscope (Zeiss, Oberkochen, Germany). Action potentials were evoked using a current injection step to 300 pA. To evoke action potentials via magnetic stimulus, a permanent NdFeB magnet (CMS Magnetics) was used delivering ~50 mT. The magnet was driven toward the EGFP+ neuron via a micromanipulator until it was approximately 1 cm from the cell. Action potential parameters were measured as previously described[104].

Single unit recordings *in vivo* in freely moving mice

In vivo electrophysiology was performed largely as described previously[59]. HS-16 four-tetrode microdrives (Neuralynx) were implanted in anaesthetized mice by using stereotaxic coordinates for the striatum described above except two injections of 1 µL each

were made at depths of -4.75 mm and -4.25 mm within the brain; the head stage was installed at an initial depth of -4 mm. After 2 weeks of recovery, mice were connected to a digital Lynx (10S) acquisition system through an HS-16 headstage preamplifier (Neuralynx), and signals were amplified and filtered (600–6000Hz). Data were acquired by using Cheetah acquisition software (Neuralynx). Baseline putative D1R neuron firing properties were recorded for 10 min in the non-magnetized arm of the custom-made place preference chamber, followed by 10 min in the magnetic arm of the chamber, and then 10 min of a second baseline recording period. Tetrodes were lowered 50μm daily during scanning for distinct units. Offline Sorter software (Plexon) cluster analysis was used to isolate units. Clustered waveforms were subsequently analyzed with MATLAB (MathWorks). Baseline activity recordings (10 min) were used to identify putative D1R neurons that exhibited firing rates below 5 Hz. Behavioral testing was performed at consistent times daily (9am-1pm) for 2-4 weeks. One mouse was excluded from this analysis because it failed to yield >n=3 units.

After the completion of these three recording sessions, the mice were injected with the D1R agonist SKF81297 (Cayman Chemical, diluted to 3 mg/kg in saline, injected i.p.). 15 minutes after the agonist had been administered, a final 10-minute recording period in the non-magnetized arm of the place preference chamber was completed. Drug injection experiments were performed only during a 5-day period following the triplicate recording procedure performed above (baseline, magnet, post-magnet). Data were not included in the triplicate analysis (Fig. 4) once a mouse had been injected with SKF81297. Data in Supplementary Fig. 11a using drug are from a single mouse.

Immunohistochemistry

Mice were perfused with 4% PFA in PBS. Brains were removed and post-fixed overnight at 4°C followed by dehydration in 30% sucrose for 2 days at 4°C. Brains were frozen in OCT and sectioned on a cryostat as 30 μm sections. As free-floating sections, tissue was washed 3x for 5 minutes with 0.3% PBS-T (Triton X-100), followed by blocking for 30 minutes in 5% donkey serum diluted in 0.3% PBS-T. Sections were then incubated with primary antibody diluted in blocking solution overnight at 4°C with agitation. The next day, sections were washed 3x for 5 minutes with 0.3% PBS-T followed by incubation with secondary antibody diluted in blocking solution for 2 hours at room temperature. Sections were washed 3x for 5 minutes in 0.3% PBS-T and mounted on slides.

Primary antibodies used in this study were: rabbit anti-TRPV4 (Santa Cruz, sc-98592) and rabbit anti-TRPV4 (Novus, NB110-74960). Secondary antibody used was: donkey anti-rabbit Alexa-488 (Invitrogen) at 1:500.

NOTE: The TRPV4 antibodies used showed significantly high background staining in WT and non-transduced tissue, making it difficult to distinguish between endogenous and virally-mediated TRPV4 expression.

Mouse behavioral testing

All testing was conducted was during the mouse light cycle at consistent times (9am-5pm).

Open field

A custom-built open-field chamber was constructed by A. Spano and M. Wheeler (23 cm x 23 cm), where four 10 cm diameter electromagnets fit into the floor, and were covered with a 0.5 cm wooden platform on which the mouse could walk. Each magnet was connected to an independent power supply delivering roughly 2.5A and 30V of power, and generating a magnetic field of roughly 150 mT. Mice were placed in the chamber for 5 minutes and baseline recordings of locomotion were measured. Magnets were turned on for 5 minutes to measure responses to the magnetic field. Each mouse was tested in the assay 1 time for a total of 10 minutes per mouse.

Real time place preference (RTPP)

The two arms of the assay were custom-built by A. Spano and M. Wheeler (4 cm wide (internal diameter) x 23 cm long). Five permanent NdFeB magnets (Four 2" x 0.5" x 0.25" magnets, one 1" x 0.5" x 0.25" magnet) were embedded into each wall of the magnetized arm, recessed at a depth of 1 cm. Each 2" x 0.5" x 0.25" magnet delivered roughly 250 mT and the magnetic field strength was roughly 50 mT in the center of the magnetized arm. The magnets were embedded at a height range of between 1.1 cm to 1.6 cm above the floor of the chamber to primarily expose the mice's heads to the field. Mice were placed into the chamber in the center of the two arms and permitted to explore for 2 minutes before recording began. The testing session lasted a total of 10 minutes. The two arms appeared identical except for the presence/absence of magnets.

For experiments using Magneto-transduced *Drd1a::Cre* mice where the magnets were removed from the RTPP chamber, two cohorts of 3 mice each were used. In the first cohort, the mice were first exposed to the magnet on Day 1, then the magnets were removed and preference was assessed on Day 2. In the second cohort, *Drd1a::Cre* mice injected with AAV1 *CMV::DIO-Magneto2.0* were trained in the chamber lacking magnets on Day 1, then tested with the magnetized chamber on Day 2. The magnetized/non-magnetized arms were transposed for each cohort to ensure that there was no preference for either side in the testing chamber.

Mouse behavioral data analysis

Mouse behaviors were measured using Ethovision XT 11 (Noldus), which is an automated tracking, recording, and measurement software package. Following each testing session of open field, linear velocity was measured (nose-point relative to center-point) with and without magnetic field for the open field assay. For RTPP, side preference was calculated as the percent of time a mouse spent in the magnetized vs. non-magnetized arm. For RTPP experiments where mice were exposed to the chamber without any magnets installed, the "magnetic arm" was chosen as the side where the magnet was placed in the testing session and numerical values were then calculated.

Statistical Methods

All statistical comparisons were performed using Prism 6 (GraphPad). No Omnibus normality test was performed for any of the data sets because sample sizes were small. Data were assumed to be normally distributed except in Fig. 4d, f and Supplementary Fig.

9c. Specific statistical tests are explicitly stated in the Figure Legends. No statistical methods were used to pre-determine sample sizes but our sample sizes are similar to those generally employed in the field[10,59,65,93,105,106]. No blinding was performed for data analysis or behavioral testing but automated and randomized quantification was performed where applicable.

A supplementary methods checklist is available.

Chapter 5 – Concluding remarks

I. Estimate of the Situation

In sum, my work has covered the study of diverse dimensions of neural circuit structure and function. In particular, I have found that primary (afferent) neural circuits exhibit dynamic tuning properties that are ultimately required for the proper development of sensory information processing. By modulating growth factor signaling or cytokine signaling during development, the fundamental structure of nociceptive circuits in particular, and probably sensory circuits more generally, is altered, which results in changes in the gain of the inputs to the nervous system. These data are in line with studies unearthing the fundamental principles of coding in the visual system[107,108], where the tuning of the primary output neurons in the retina can modulate the visual scene contrast information. More thorough characterization of the breadth of this principle is required since it appears to be a fundamental mechanism by which the nervous system regulates incoming information from the environment.

Moreover, I have invented a means by which neural circuits can be remotely controlled by magnetic fields. I designed a genetically encoded synthetic magnetoreceptor, which enables activation of neural circuits rapidly and totally remotely. Through using this tool, and others like it, the neuroscience community can begin to uncover the roles of diffuse and distinct cell types scattered across the body previously impervious to rapid, remote, and reversible activation with actuator technologies. Magnetic actuators such as Magneto can open up new avenues in understanding the mechanisms by which neural circuits function. Perhaps more distantly, Magneto and other actuator technology can be applied to the clinical intervention of dysfunctional neural circuitry.

In addition, it will be important to utilize remote actuator technologies to leverage control over a variety of other signaling pathways important for modulating organismal function. For instance, if magnetogenetic control over biochemistry or inhibitory currents could be developed, multiple modes of stimulation could be applied to the entire brain using a single stimulus. Perhaps even the interaction between several groups of cells with one another can be controlled by differentially modulating the activity of each population using a variety of magnetogenetic tools. Moreover, the ability to begin controlling not only animal and human tissues for biomedical research but plant cells as well. I envision the possibility that plants could be engineered to be grown in harsher environments by expressing magnetically sensitive actuators in different tissues and then growing the plants in the presence of magnetic fields. These approaches, and others like them, will enable possible modification of organisms that can be useful for human agriculture.

Perhaps most generally relevant to both projects is the inability of the nervous system to interpret stimuli that cannot be encoded in the nervous system at all. In other words, cells are receptive to only those stimuli that can be biophysically sensed and transformed into electrical or chemical signals. Moving forward, the field of neuroscience as a whole must grapple with the idea of what it means to form maps of the world in the purest sense. How does a lattice of organic tissue orchestrate the symphony that is the multisensory mind? Can we reorganize the nervous system artificially, therapeutically, or computationally such that we can understand the substance of the world as told through the existence of the mind? Might we better understand what “is” or “is not” through the assemblage of biological computing left to us to analyze the world? Or might such questions be useless altogether?

"Whereof one cannot speak, thereof one must be silent."[109]

II. References

1. Lu, B., Pang, P. T. & Woo, N. H. The yin and yang of neurotrophin action. *Nat. Rev. Neurosci.* **6,** 603–14 (2005).
2. Delmas, P., Hao, J. & Rodat-Despoix, L. Molecular mechanisms of mechanotransduction in mammalian sensory neurons. *Nat. Rev. Neurosci.* **12,** 139–53 (2011).
3. Fitzgerald, M. The development of nociceptive circuits. *Nat. Rev. Neurosci.* **6,** 507–20 (2005).
4. Li, L., Rutlin, M., Abraira, V., Cassidy, C. & Kus, L. The functional organization of cutaneous low-threshold mechanosensory neurons. *Cell* 1615–1627 (2011). doi:10.1016/j.cell.2011.11.027
5. Abraira, V. E. & Ginty, D. D. The sensory neurons of touch. *Neuron* **79,** 618–39 (2013).
6. Bai, L. *et al.* Genetic Identification of an Expansive Mechanoreceptor Sensitive to Skin Stroking. *Cell* **163,** 1783–1795 (2015).
7. Zimmerman, A., Bai, L. & Ginty, D. D. of Mammalian Skin. *Science (80-.).* **346,** 950–954 (2014).
8. Woolf, C. J. Neuronal Plasticity: Increasing the Gain in Pain. *Science (80-.).* **288,** 1765–1768 (2000).
9. Costigan, M., Scholz, J. & Woolf, C. J. Neuropathic Pain : A Maladaptive Response of the Nervous System to Damage. *Annu. Rev. Neurosci.* (2009). doi:10.1146/annurev.neuro.051508.135531
10. Wheeler, M. a. *et al.* TNF-α/TNFR1 Signaling Is Required for the Development and Function of Primary Nociceptors. *Neuron* **82,** 587–602 (2014).
11. Park, K. J., Grosso, C. A., Aubert, I., Kaplan, D. R. & Miller, F. D. p75NTR-dependent, myelin-mediated axonal degeneration regulates neural connectivity in the adult brain. *Nat. Neurosci.* **13,** 559–66 (2010).
12. Singh, K. K. *et al.* Developmental axon pruning mediated by BDNF-p75NTR-dependent axon degeneration. *Nat. Neurosci.* **11,** 649–58 (2008).
13. Deppmann, C. D. *et al.* A model for neuronal competition during development. *Science* **320,** 369–73 (2008).
14. Sharma, N. *et al.* Long-distance control of synapse assembly by target-derived NGF. *Neuron* **67,** 422–34 (2010).
15. Chao, M. V. Neurotrophins and their receptors: a convergence point for many signalling pathways. *Nat. Rev. Neurosci.* **4,** 299–309 (2003).
16. Marmigère, F. & Ernfors, P. Specification and connectivity of neuronal subtypes in the sensory lineage. *Nat. Rev. Neurosci.* **8,** 114–27 (2007).
17. Lallemend, F. & Ernfors, P. Molecular interactions underlying the specification of sensory neurons. *Trends Neurosci.* **35,** 373–81 (2012).
18. Locksley, R. M., Killeen, N. & Lenardo, M. J. The TNF and TNF receptor superfamilies: integrating mammalian biology. *Cell* **104,** 487–501 (2001).
19. Liu, Z., Hsu, H., Goeddel, D. V & Karin, M. Dissection of TNF Receptor 1 Effector Functions: JNK Activation Is Not Linked to Apoptosis While NF-kB Activation Prevents Cell Death. *Cell* **87,** 565–576 (1996).
20. Chang, L. *et al.* The E3 ubiquitin ligase itch couples JNK activation to TNFalpha-induced cell death by inducing c-FLIP(L) turnover. *Cell* **124,** 601–13 (2006).

21. Cowan, W. M. Viktor Hamburger and Rita Levi-Montalcini: the path to the discovery of nerve growth factor. *Annu. Rev. Neurosci.* **24,** 551–600 (2001).
22. Bamji, S. X. *et al.* The p75 neurotrophin receptor mediates neuronal apoptosis and is essential for naturally occurring sympathetic neuron death. *J. Cell Biol.* **140,** 911–23 (1998).
23. Ernfors, P., Lee, K. F., Kucera, J. & Jaenisch, R. Lack of neurotrophin-3 leads to deficiencies in the peripheral nervous system and loss of limb proprioceptive afferents. *Cell* **77,** 503–12 (1994).
24. Nykjaer, A., Lee, R., Teng, K. & Jansen, P. Sortilin is essential for proNGF-induced neuronal cell death. *Nature* **427,** 15–20 (2004).
25. Chowdary, P. D., Che, D. L. & Cui, B. Neurotrophin signaling via long-distance axonal transport. *Annu. Rev. Phys. Chem.* **63,** 571–94 (2012).
26. Stoeckel, K., Schwab, M. & Thoenen, H. Specificity of Retrograde Transport of Nerve Growth Factor (NGF) in Sensory Neurons: A Biochemical and Morphological Study. *Brain Res.* **89,** 1–14 (1975).
27. Landreth, G. E. & Shooter, E. M. Nerve growth factor receptors on PC12 cells: ligand-induced conversion from low- to high-affinity states. *Proc. Natl. Acad. Sci. U. S. A.* **77,** 4751–5 (1980).
28. Schecterson, L. C. & Bothwell, M. Novel roles for neurotrophins are suggested by BDNF and NT-3 mRNA expression in developing neurons. *Neuron* **9,** 449–63 (1992).
29. Wang, N., Orr-Urtreger, A. & Korczyn, A. D. The role of neuronal nicotinic acetylcholine receptor subunits in autonomic ganglia: lessons from knockout mice. *Prog. Neurobiol.* **68,** 341–60 (2002).
30. Shao, Z. *et al.* TAJ/TROY, an orphan TNF receptor family member, binds Nogo-66 receptor 1 and regulates axonal regeneration. *Neuron* **45,** 353–9 (2005).
31. Lee, R., Kermani, P., Teng, K. K. & Hempstead, B. L. Regulation of cell survival by secreted proneurotrophins. *Science* **294,** 1945–8 (2001).
32. Yang, J. *et al.* Neuronal release of proBDNF. *Nat. Neurosci.* **12,** 113–5 (2009).
33. Yano, H., Torkin, R., Martin, L. A., Chao, M. V & Teng, K. K. Proneurotrophin-3 is a neuronal apoptotic ligand: evidence for retrograde-directed cell killing. *J. Neurosci.* **29,** 14790–802 (2009).
34. Roux, P. P. & Barker, P. a. Neurotrophin signaling through the p75 neurotrophin receptor. *Prog. Neurobiol.* **67,** 203–33 (2002).
35. Hempstead, B., Martin-Zanca, D. & Kaplan, D. High-affinity NGF binding requires coexpression of the trk proto-oncogene and the low-affinity NGF receptor. *Nature* (1991). at <http://www.nature.com/nature/journal/v350/n6320/abs/350678a0.html>
36. Lee, K. F. *et al.* Targeted mutation of the gene encoding the low affinity NGF receptor p75 leads to deficits in the peripheral sensory nervous system. *Cell* **69,** 737–49 (1992).
37. Bergmann, I. *et al.* Analysis of cutaneous sensory neurons in transgenic mice lacking the low affinity neurotrophin receptor p75. *Eur. J. Neurosci.* **9,** 18–28 (1997).
38. Wehrman, T. *et al.* Structural and mechanistic insights into nerve growth factor interactions with the TrkA and p75 receptors. *Neuron* **53,** 25–38 (2007).
39. Nikoletopoulou, V. *et al.* Neurotrophin receptors TrkA and TrkC cause neuronal death whereas TrkB does not. *Nature* **467,** 59–63 (2010).

40. Mehlen, P. & Bredesen, D. E. The dependence receptor hypothesis. *Apoptosis* **9,** 37–49 (2004).
41. Micheva, K. D., Busse, B., Weiler, N. C., O'Rourke, N. & Smith, S. J. Single-synapse analysis of a diverse synapse population: Proteomic imaging methods and markers. *Neuron* **68,** 639–653 (2010).
42. Zemelman, B. V., Lee, G. a., Ng, M. & Miesenböck, G. Selective photostimulation of genetically chARGed neurons. *Neuron* **33,** 15–22 (2002).
43. Penfield, W. Some Mechanisms of Consciousness Discovered During Electrical Stimulation of the Brain. *Proc Natl Acad Sci U S A* **44,** 51–66 (1958).
44. Seidemann, E., Zohary, E. & Newsome, W. T. Temporal gating of neural signals during performance of a visual discrimination task. *Nature* **394,** 72–75 (1998).
45. Tsien, R. Y. the Green Fluorescent Protein. *Annu. Rev. Biochem.* **67,** 509–44 (1998).
46. Frazier, M. *et al.* Initial sequencing and analysis of the human genome. *Nature* **409,** 860–921 (2001).
47. White, J. G., Southgate, E., Thomson, J. N. & Brenner, S. The Structure of the Nervous System of the Nematode *Caenorhabditis elegans*. *Philos. Trans. R. Soc. B Biol. Sci.* **314,** 1–340 (1986).
48. Boyden, E. S., Zhang, F., Bamberg, E., Nagel, G. & Deisseroth, K. Millisecond-timescale, genetically targeted optical control of neural activity. *Nat. Neurosci.* **8,** 1263–1268 (2005).
49. Boyden, E. S. A history of optogenetics: the development of tools for controlling brain circuits with light. *F1000 Biol. Rep.* **3,** 11 (2011).
50. Chow, B. Y. *et al.* High-performance genetically targetable optical neural silencing by light-driven proton pumps. *Nature* **463,** 98–102 (2010).
51. Zhang, F. *et al.* Multimodal fast optical interrogation of neural circuitry. *Nature* **446,** 633–639 (2007).
52. Airan, R. D., Thompson, K. R., Fenno, L. E., Bernstein, H. & Deisseroth, K. Temporally precise in vivo control of intracellular signalling. *Nature* **458,** 1025–1029 (2009).
53. Yizhar, O., Fenno, L. E., Davidson, T. J., Mogri, M. & Deisseroth, K. Optogenetics in Neural Systems. *Neuron* **71,** 9–34 (2011).
54. Berlin, S. *et al.* A family of photoswitchable NMDA receptors. 1–29 (2016). doi:10.7554/eLife.12040
55. Sternson, S. M. & Roth, B. L. Chemogenetic Tools to Interrogate Brain Functions. *Annu. Rev. Neurosci.* 387–407 (2014). doi:10.1146/annurev-neuro-071013-014048
56. Armbruster, B. N., Li, X., Pausch, M. H., Herlitze, S. & Roth, B. L. Evolving the lock to fit the key to create a family of G protein-coupled receptors potently activated by an inert ligand. *Proc. Natl. Acad. Sci. U. S. A.* **104,** 5163–5168 (2007).
57. Magnus, C. J. *et al.* Chemical and genetic engineering of selective ion channel-ligand interactions. *Science* **333,** 1292–1296 (2011).
58. Arenkiel, B. R., Klein, M. E., Davison, I. G., Katz, L. C. & Ehlers, M. D. Genetic control of neuronal activity in mice conditionally expressing TRPV1. *Nat Methods* **5,** 299–302 (2008).
59. Güler, A. D. *et al.* Transient activation of specific neurons in mice by selective expression of the capsaicin receptor. *Nat. Commun.* **3,** 746 (2012).
60. Han, L. *et al.* A subpopulation of nociceptors specifically linked to itch. *Nat. Neurosci.* (2012). doi:10.1038/nn.3289

61. Jeong, J. W. *et al.* Wireless Optofluidic Systems for Programmable In Vivo Pharmacology and Optogenetics. *Cell* **162,** 662–674 (2015).
62. Iyer, S. M. *et al.* Virally mediated optogenetic excitation and inhibition of pain in freely moving nontransgenic mice. *Nat. Biotechnol.* **32,** 274–8 (2014).
63. Huang, H., Delikanli, S., Zeng, H., Ferkey, D. M. & Pralle, A. Remote control of ion channels and neurons through magnetic-field heating of nanoparticles. *Nat. Nanotechnol.* **5,** 602–606 (2010).
64. Stanley, S. a *et al.* Radio-wave heating of iron oxide nanoparticles can regulate plasma glucose in mice. *Science* **336,** 604–8 (2012).
65. Stanley, S. a., Sauer, J., Kane, R. S., Dordick, J. S. & Friedman, J. M. Remote regulation of glucose homeostasis in mice using genetically encoded nanoparticles. *Nat. Med.* **21,** 92–98 (2015).
66. Chen, R., Romero, G. & Christiansen, M. G. Wireless magnetothermal deep brain stimulation. 6–12 (2015).
67. Wheeler, M. A. *et al.* Genetically targeted magnetic control of the nervous system. *Nat Neurosci* **advance on,** (2016).
68. Gradinaru, V., Mogri, M., Thompson, K. R., Henderson, J. M. & Deisseroth, K. Optical deconstruction of parkinsonian neural circuitry. *Science* **324,** 354–359 (2009).
69. Alexander, G. M. *et al.* Remote control of neuronal activity in transgenic mice expressing evolved G protein-coupled receptors. *Neuron* **63,** 27–39 (2009).
70. Bernstein, J. G., Garrity, P. a. & Boyden, E. S. Optogenetics and thermogenetics: Technologies for controlling the activity of targeted cells within intact neural circuits. *Curr. Opin. Neurobiol.* **22,** 61–71 (2012).
71. Hughes, S., McBain, S., Dobson, J. & El Haj, A. J. Selective activation of mechanosensitive ion channels using magnetic particles. *J. R. Soc. Interface* **5,** 855–863 (2008).
72. Stanley, S. a., Sauer, J., Kane, R. S., Dordick, J. S. & Friedman, J. M. Remote regulation of glucose homeostasis in mice using genetically encoded nanoparticles. *Nat. Med.* **21,** 92–98 (2015).
73. Chen, R., Romero, G., Christiansen, M. G., Mohr, A. & Anikeeva, P. Wireless magnetothermal deep brain stimulation. *Science* **347,** 1477–80 (2015).
74. Loukin, S., Zhou, X., Su, Z., Saimi, Y. & Kung, C. Wild-type and brachyolmia-causing mutant TRPV4 channels respond directly to stretch force. *J. Biol. Chem.* **285,** 27176–27181 (2010).
75. Liedtke, W. *et al.* Vanilloid receptor-related osmotically activated channel (VR-OAC), a candidate vertebrate osmoreceptor. *Cell* **103,** 525–535 (2000).
76. Güler, A. D. *et al.* Heat-evoked activation of the ion channel, TRPV4. *J. Neurosci.* **22,** 6408–14 (2002).
77. Stanley, S. Biological nanoparticles and their influence on organisms. *Curr. Opin. Biotechnol.* **28,** 69–74 (2014).
78. Iordanova, B., Robison, C. S. & Ahrens, E. T. Design and characterization of a chimeric ferritin with enhanced iron loading and transverse NMR relaxation rate. *J. Biol. Inorg. Chem.* **15,** 957–965 (2010).
79. Lei, L. *et al.* A TRPV4 channel C-terminal folding recognition domain critical for trafficking and function. *J. Biol. Chem.* **288,** 10427–10439 (2013).
80. Hofherr, A., Fakler, B. & Klöcker, N. Selective Golgi export of Kir2.1 controls the

stoichiometry of functional Kir2.x channel heteromers. *J. Cell Sci.* **118,** 1935–1943 (2005).
81. Gradinaru, V. *et al.* Molecular and Cellular Approaches for Diversifying and Extending Optogenetics. *Cell* **141,** 154–165 (2010).
82. Lytton, J., Westlin, M. & Hanley, M. R. Thapsigargin inhibits the sarcoplasmic or endoplasmic reticulum Ca-ATPase family of calcium pumps. *J. Biol. Chem.* **266,** 17067–17071 (1991).
83. Phan, M. N. *et al.* Functional characterization of TRPV4 as an osmotically sensitive ion channel in porcine articular chondrocytes. *Arthritis Rheum.* **60,** 3028–37 (2009).
84. Sohal, V. S., Zhang, F., Yizhar, O. & Deisseroth, K. Parvalbumin neurons and gamma rhythms enhance cortical circuit performance. *Nature* **459,** 698–702 (2009).
85. Andermann, P., Ungos, J. & Raible, D. W. Neurogenin1 defines zebrafish cranial sensory ganglia precursors. *Dev. Biol.* **251,** 45–58 (2002).
86. Douglass, A. D., Kraves, S., Deisseroth, K., Schier, A. F. & Engert, F. Escape Behavior Elicited by Single, Channelrhodopsin-2-Evoked Spikes in Zebrafish Somatosensory Neurons. *Curr. Biol.* **18,** 1133–1137 (2008).
87. Tian, L. *et al.* Imaging neural activity in worms, flies and mice with improved GCaMP calcium indicators. *Nat. Methods* **6,** 875–881 (2009).
88. Wyart, C. *et al.* Optogenetic dissection of a behavioural module in the vertebrate spinal cord. *Nature* **461,** 407–410 (2009).
89. Sagasti, A., Guido, M. R., Raible, D. W. & Schier, A. F. Repulsive Interactions Shape the Morphologies and Functional Arrangement of Zebrafish Peripheral Sensory Arbors. *Curr. Biol.* **15,** 804–814 (2005).
90. Hersch, S. M. *et al.* Electron microscopic analysis of D1 and D2 dopamine receptor proteins in the dorsal striatum and their synaptic relationships with motor corticostriatal afferents. *J. Neurosci.* **15,** 5222–5237 (1995).
91. Berke, J. D., Okatan, M., Skurski, J. & Eichenbaum, H. B. Oscillatory Entrainment of Striatal Neurons in Freely-Moving Rats. *Neuron* **43,** 883–896 (2004).
92. Wise, R. a. Dopamine, learning and motivation. *Nat. Rev. Neurosci.* **5,** 483–494 (2004).
93. Tsai, H.-C. *et al.* Phasic firing in dopaminergic neurons is sufficient for behavioral conditioning. *Science* **324,** 1080–1084 (2009).
94. Lobo, M. K. *et al.* Cell type-specific loss of BDNF signaling mimics optogenetic control of cocaine reward. *Science* **330,** 385–390 (2010).
95. Zengin-Toktas, Y. *et al.* Motivational properties of D2 and D3 dopamine receptors agonists and cocaine, but not with D1 dopamine receptors agonist and l-dopa, in bilateral 6-OHDA-lesioned rat. *Neuropharmacology* **70,** 74–82 (2013).
96. Gore, B. B. & Zweifel, L. S. Genetic Reconstruction of Dopamine D1 Receptor Signaling in the Nucleus Accumbens Facilitates Natural and Drug Reward Responses. *J. Neurosci.* **33,** 8640–8649 (2013).
97. Stuber, G. D., Britt, J. P. & Bonci, A. Optogenetic modulation of neural circuits that underlie reward seeking. *Biol. Psychiatry* **71,** 1061–1067 (2012).
98. O'Neil, R. G. & Heller, S. The mechanosensitive nature of TRPV channels. *Pflugers Arch.* **451,** 193–203 (2005).
99. Liedtke, W. & Kim, C. Functionality of the TRPV subfamily of TRP ion channels: add mechano-TRP and osmo-TRP to the lexicon! *Cell. Mol. Life Sci.* **62,** 2985–3001 (2005).
100. Matthews, B. D. *et al.* Ultra-rapid activation of TRPV4 ion channels by mechanical

forces applied to cell surface beta1 integrins. *Integr. Biol. (Camb).* **2,** 435–442 (2010).
101. Kimmel, C. B., Ballard, W. W., Kimmel, S. R., Ullmann, B. & Schilling, T. F. Stages of embryonic development of the zebrafish. *Dev. Dyn.* **203,** 253–310 (1995).
102. McFarland, T. J. *et al.* Evaluation of a novel short polyadenylation signal as an alternative to the SV40 polyadenylation signal. *Plasmid* **56,** 62–67 (2006).
103. Smith, C. J., Morris, A. D., Welsh, T. G. & Kucenas, S. Contact-Mediated Inhibition Between Oligodendrocyte Progenitor Cells and Motor Exit Point Glia Establishes the Spinal Cord Transition Zone. *PLoS Biol.* **12,** e1001961 (2014).
104. Hargus, N. J., Nigam, A., Bertram, E. H. & Patel, M. K. Evidence for a role of Nav1.6 in facilitating increases in neuronal hyperexcitability during epileptogenesis. *J. Neurophysiol.* **110,** 1144–57 (2013).
105. Quintana, A. *et al.* Lack of GPR88 enhances medium spiny neuron activity and alters motor- and cue-dependent behaviors. *Nat. Neurosci.* **15,** 1547–55 (2012).
106. Chen, S., Chiu, C. N., McArthur, K. L., Fetcho, J. R. & Prober, D. a. TRP channel mediated neuronal activation and ablation in freely behaving zebrafish. *Nat. Methods* **8,** 1–7 (2015).
107. Masland, R. H. Sensory Systems : Fine-Tuning the. **15,** 808–810
108. Hosoya, T., Baccus, S. a & Meister, M. Dynamic predictive coding by the retina. *Nature* **436,** 71–77 (2005).
109. Wittgenstein, L. *Tractatus Logico-Philosophicus (TLP)*, 1922, C. K. Ogden (trans.), London: Routledge & Kegan Paul. Originally published as "Logisch-Philosophische Abhandlung", in *Annalen der Naturphilosophische*, XIV (3/4), 1921.

Appendix I

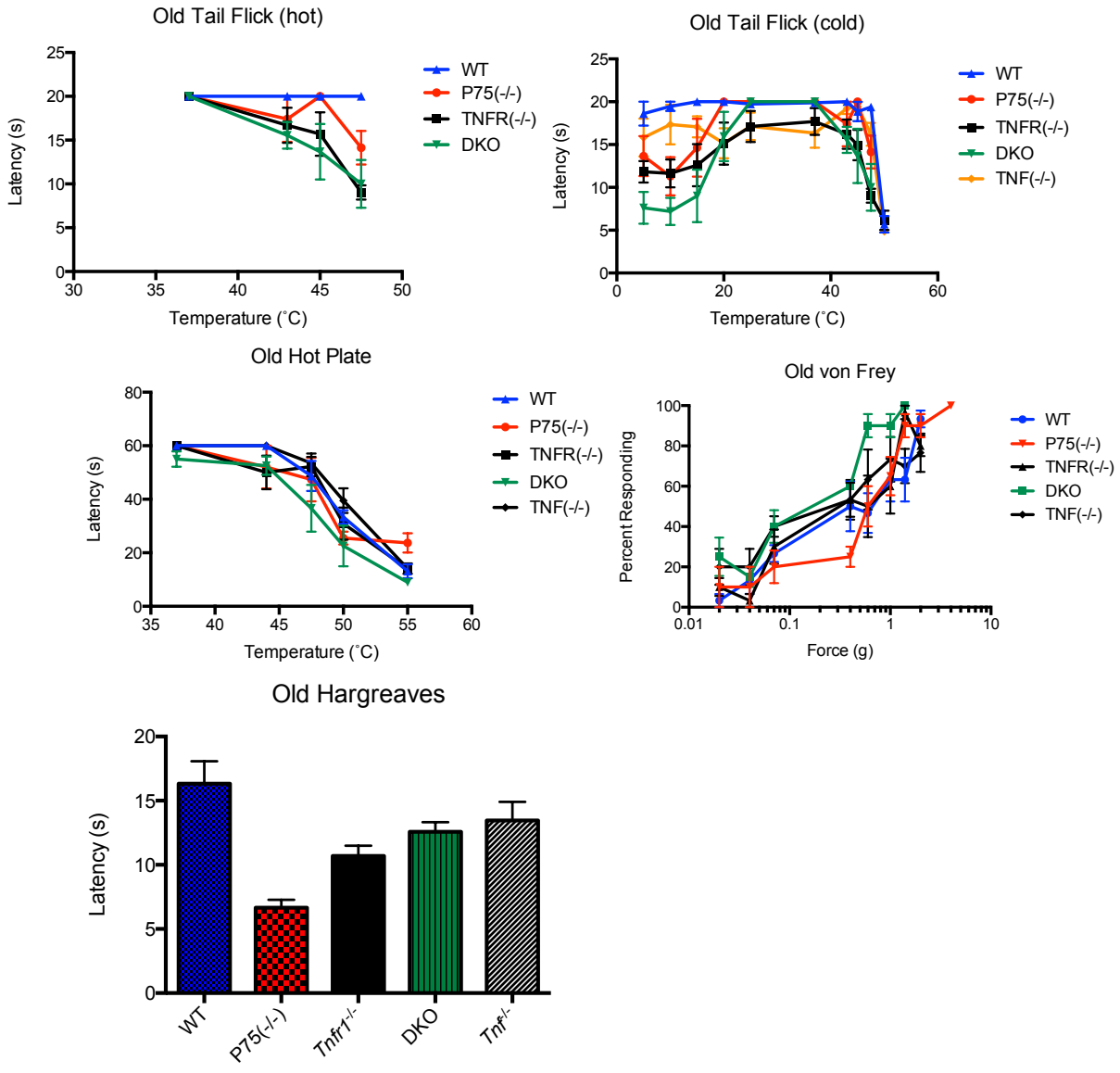

Figure legend: Continuation of pain behavioral data for TNFRSF KO mice. Overall, the data suggest that functional adaptation can occur over time in the KOs.

Appendix II

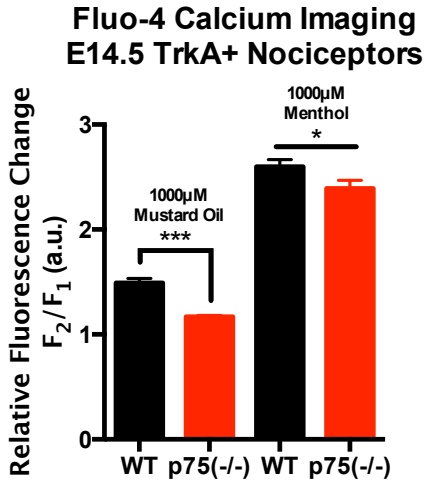

a. p75-/- nociceptors are hyposensitive to cold stimuli shown through in vitro calcium imaging.

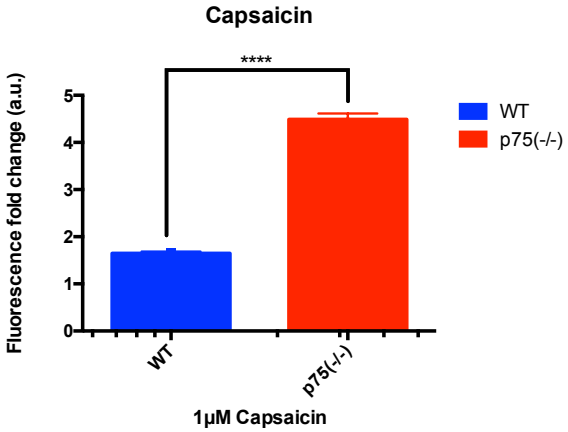

b. p75-/- nociceptors are hypersensitive to capsaicin application